DETECTION AND ASSESSMENT OF CARDIAC PATENT FORAMEN OVALE

by

İSMAİL BURAK PARLAK

B.S., Computer Engineering, Galatasaray University, 2001

M.S., Biomedical Engineering, Boğaziçi University, 2005

Submitted to the Institute of Biomedical Engineering

in partial fulfillment of the requirements

for the degree of

Doctor

of

Philosophy

Boğaziçi University

2013

ACKNOWLEDGMENTS

A PhD study with innovative methods in biomedical area not only requires a theoretical and experimental effort but also a great inspiration and motivation. I think the guidance is much more hard-working when a novelty is being taken into account which would improve recent studies. I owe this study to my supervisors who conducted these complex steps. Prof. Dr. Ahmet ADEMOĞLU taught me step by step with patience how to develop a simulation and experimental survey using mathematical and computational bases and to route a research with many bottlenecks. Assoc. Prof. Dr. Salih Murat EGİ led my findings by enduring deadlocks in both medical and engineering aspects, by showing the shortcuts to access the unknowns and especially by motivating our progressive steps with comparative examples. Both qualitative and quantitative methods were accomplished by their precious motivation. For me, it is wordless to express my gratitude to them for their patience, grace and altruism during my PhD journey.

Academical supports in terms of the setup of experimental acquisition, the interpretation of medical data, financial costs are other challenges for PhD studies. I am feeling lucky to have strong contacts with Divers Alert Network (DAN) Europe. I should confess that Prof. Costantino BALESTRA, Dr. Peter GERMONPRE and Dr. Alessandro MARRONI shared their precious knowledge with me like my supervisors. I know that to have the opportunity to work with Prof. Costantino BALESTRA is a big chance for a graduate student. His inspirations do not only give the chance to learn the milestones in the physiology of cardio-pulmonary system but also encourage the enthusiasm to discover an untouched field in microemboli studies. Without his inspirations and his benevolence, it was impossible to achieve our goal. Dr. Peter GERMONPRE who provided initial training sets and arranged our acquisition setup led us to follow correct methodology. Dr. Alessandro MARRONI who shared the background knowledge of DAN-Europe in diving physiology provided us an important grant.

During the evolution of an academical work, the critical interpretation of methods and results is crucial to provide a comprehensible pathway and to benefit the correct utility of the work. I am indebted to Assoc. Prof. Ata AKIN and Assist. Prof. Dr. Burak ARSLAN for showing me how to evolve our findings and to represent them better in our manuscripts. Helpful comments of Prof. Dr. Salih AYDIN and his indispensable aids in both medical and engineering areas shaped this work. It is obvious that clinical viewpoint would orient and enrich a biomedical study in order to provide a useful tool for medical purposes. Dr. Özlem Batukan ESEN, Dr. Serap TEKİN and medical staff of Memorial Hospital showed me how to interpret an echocardiographic acquisition with notable landmarks and also helped to explain the differences between constrast enhanced multimodal echocardiography.

My very special thanks are destined to Dr. Thyl SNOECK, Dr. Mikel EZQUER and Dr. Steven PROVYN. Their great inspirations and friendship led this study with the dynamic environment of both Environmental and Occupational Physiology Laboratory of Haute Ecole Paul Henri Spaak and Experimental Anatomy Laboratory of Vrije Universiteit in Brussels. I am also very grateful to several colleagues from Boğaziçi University for encouraging discussions and insights: Adil Deniz DURU who shared his knowledge and experiences in programming and data acquisition with all PhD candidates in *NeurAL* without doubt, Hamdi ERYILMAZ who directed a new perspective in neuroscience.

Finally, I should thank my brother Assist. Prof. Dr. Murat Levent DEMİRCAN who guided and shared new ideas and approaches from different fields, Prof. Dr. Bernard LEVRAT who taught me the verbal power and the computational secrets behind the words and the library staff; Filiz Flores MAMONDI and Huriye ÇELEBİ. Without their precious help, it would be impossible to reach to such important articles in the area of congenital cardiac studies and the microemboli fields.

Lastly, my deepest gratitude is destined to my parents. Without their patience and inspirations during my education, this work could not be accomplished.

ABSTRACT

DETECTION AND ASSESSMENT OF CARDIAC PATENT FORAMEN OVALE

Arterial microemboli are gas filled structures which are formed in intravascular and extravascular environment. They are characterized in spherical or ellipsoid forms which would cause diseases in a broad range from stroke to migraine. Cardiac Patent Foramen Ovale (CPFO) is considered as a congenital defect through both atria as a permeable shunt with a prevalence frequency of 25-30% in asymptomatic population. Decompression Sickness (DCS) is a fatal disease during hyperbaric and hypobaric activities due to unestimated effects of microemboli. CPFO aperture combined with DCS is a clinical problem where bubble analysis is managed manually by special and trained cardiologists. Even this problem was considered recently by different groups within sound, image and video forms, an automated tool is considered as a challenge due to algorithmic and mechanical constraints related to noise, monitoring and probe localization. We aimed to develop a spatio-temporal methodology for clinicians which would not carry out long lasting videos where the number and the size of microemboli alter dynamically. In this thesis, developed methods are classified into two groups; qualitative and quantitative assessments. These approaches were tested initially in a simulation environment with artificial microemboli. Furthermore, microemboli and CPFO were monitored in subjects through videos using two modalities: contrast Trans Esophageal Echocardiography and contrast Trans Thoracic Echocardiography. Even our procedures would get accurate findings within videos, it is important to note that low resolution, high speckle noise, shadowing would introduce false alarms. Consequently, we conclude that this routine would standardize CPFO analysis and offer better adjustment for bubble detection.

Keywords: Congenital Defect, Intravascular Microemboli, Right-to-Left Shunts, Gabor Wavelet, Active Contours, Decompression Sickness.

ÖZET

KARDİYAK PATENT FORAMEN OVALE TESPİTİ VE DEĞERLENDİRİLMESİ

Damariçi ve damardışı ortamda oluşan arteryel microemboli içinde gaz bulunan yapılardır. Küre veya elips biçiminde nitelendirilen bu kabarcıklar inmeden migrene kadar geniş ölçekte hastalıklara sebep olmaktadır. Kalbin her iki kulakçığı arasında geçirgen bir yol vazifesi gören konjenital bir bozukluk olan Kardiyak Patent Foramen Ovale (KPFO)'nin belirti vermeyen bir topluluk içerisinde görülme sıklığı %25-30 arasındadır. Dekompresyon Hastalığı (DH)'nın, mikroembolilerin önceden kestirilemez etkileri sebebiyle hiperbarik ve hipobarik uygulamalarda ölümcül sonuçları olmaktadır. DH ile birleşmiş KPFO açıklığı klinik bir problem olmakla birlikte, kabarcıklar uzman kardiyologlar tarafından elle işaretlenmektedir. Bu problemin farklı araştırma grupları tarafından ses, imge ve video tabanlı olarak ele alınmasına rağmen, otomatik bir yöntem vasıtasıyla analizinin; gürültü, görüntüleme ve prob sabitleme gibi algoritmik ve mekanik problemlerden ötürü zor olduğu düşünülmektedir. Çalışmamızda uzun süren ve mikroemboli boyut ve sayısının değiştiği için sürekli analiz yapamayacak uzmanlar için zaman-uzamsal bir yaklaşım geliştirmeyi hedefledik. Bu tezdeki yaklaşımlar, niteliksel ve niceliksel olmak üzere iki farklı grupta ele alınmaktadır. Bu yöntemler, ilk olarak suni kabarcıklar ile simülasyon ortamında test edilmiştir. Sonraki aşamada, mikroemboli ve KPFO gönüllü kişiler üzerinde, Trans Özofajyal Ekokardiyografi ve Trans Torasik Ekokardiyografi olmak üzere iki görüntüleme yöntemi vasıtasıyla incelenmiştir. Önerdiğimiz yöntemler video imgeleri üzerinde başarılı sonuçlar vermesine rağmen; düşük çözünürlük, yüksek speckle gürültüsü ve gölgeleme etmenleri yanlış alarmlara sebep olabilmektedir. Sonuç olarak, bu çalışmanın KPFO analizini standartlaştırabileceği ve kabarcık tespiti konusunda faydalı olabileceği düşünülmektedir.

Anahtar Sözcükler: Konjenital Bozukluk, Intravasküler Emboli, Sağ-Sol Şantları, Gabor Dalgacığı, Aktif Konturlar, Dekompresyon Hastalığı.

TABLE OF CONTENTS

LIST OF FIGURES

LIST OF TABLES

LIST OF SYMBOLS

$E(I)$	Entropy of an image I.
h	Histogram of an image.
H	Shannon measure for the entropy of an image.
p_i	Probabilistic distributon through the histogram h.
μ_0	Average gray level of the background image.
μ_1	Average gray level of the foreground image.
ω_0	Probability of background occurence.
ω_1	Probability of foreground occurence.
σ_0	Variance of background class.
σ_1	Variance of foreground class.

LIST OF ABBREVIATIONS

CCD	Congenital Cardiac Disease
CPFO	Cardiac Patent Foramen Ovale
DCI	Decompression Illness
DCS	Decompression Sickness
FPS	Frames per Second
IAS	Interatrial Septum
MRI	Magnetic Resonance Imaging
PDA	Patent Ductus Arteriosus
RLS	Right to Left Shunt
ROI	Region Of Interest
SNR	Signal-to-Noise Ratio
TEE	Trans Esophageal Echocardiogram
TTE	Trans Thoracic Echocardiogram
VSD	Ventricular Septal Defect

1. INTRODUCTION

Over the last decades, the classification and definition of Cardiac Patent Foramen Ovale (CPFO) were debated from the aspects of both anatomical and physiological issues. Anatomically, CPFO is considered as a remnant of mal occlusion between Left and Right Atria (LA, RA) after the birth and is briefly characterized as a congenital defect represented in Figure 1.1. On the other hand, several studies after 70s revealed the association of CPFO with several diseases. Therefore, CPFO would be introduced within three different categories.

Firstly, CPFO would be considered as a septal shunt which is inactive in normal conditions. Normal conditions mean the ordinary air pressure that does not trigger microemboli production in circulatory system and also regular pressure gradient between atria through standard physical activities performed by the subject. This anatomical interpretation addresses only its size and does not take into account how this defect is actively working. Generally, *post mortem* studies are focused on CPFO with this angle of view for the biostatistical and epidemiologic aims.

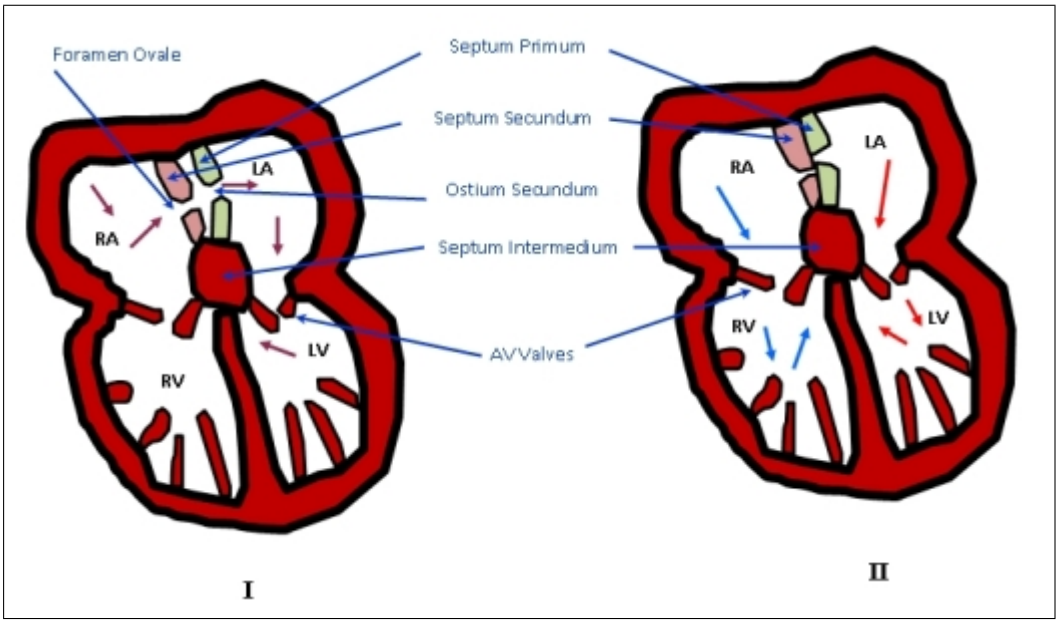

Figure 1.1 CPFO Schematization: (I) CPFO Aperture, (II) Fused CPFO Aperture.

Secondly, recent research revealed its combined effects within several diseases in a broad range from stroke to migraine. Its combined effects introduce the physiology of shunt activity which is measured by the functionality of shunt through maneuvers and tasks. Its functionality is measured via the interpretation of clinical examinations monitored through video recordings. This clinical task is done for the assessment of CPFO and the determination of its severity. Therefore, it is described as an indirect disease which triggers other ones. Its sealing procedure should be decided regarding its grading score.

Thirdly, hypobaric and hyperbaric environments which would be considered as extreme conditions introduce microemboli generation in blood. These gas filled structures which travel towards cardiac chambers would trigger CPFO aperture due to the low or high pressure gradient between LA and RA. In this case, microemboli would cause severe diseases especially Decompression Sickness (DCS). This microemboli-CPFO association is characterized as a disease combined with the anatomy of CPFO. Micremboli activity combined with CPFO functionality is the main threat for divers, pilots and astronauts. In this case, CPFO should be examined with detailed monitoring procedures. Its assessment should be evaluated using grading scores within a longitudinal survey in order to find a reliable closure method.

In this thesis, the dynamics of CPFO detection were examined in both simulation and experimental environment. Detection results revealed the behavioral similarities of microemboli within images and videos during the temporal analysis. Experimental analysis of CPFO and its relationship with intravascular bubbles were studied regarding the fundamental cardiac imaging modality; echocardiography.

Echocardiographic imaging is a clinical tool which became a golden standard in the diagnosis of Congenital Cardiac Diseases (CCD). Medical assessment is performed with the contrast media which is generally a saline solution enhanced with air bubbles. CPFO severity is measured through the response of the shunt to the passage of contrast bubbles. Even if CPFO closure is generally evaluated with the aperture size, the activity of CPFO shunt is measured regarding total number of crossing microemboli.

Bubble grading which is actually measured with bubble numbers is a direct measure of CPFO. Despite correct visualization, reliable diagnosis of CPFO activity requires special trainings on different type of visual examples within multimodal echocardiographic frames. It is remarkable that noise and artifacts might cause drastic variations between measurements performed by clinicians.

Even though, imaging bottlenecks like noise and artifacts would be filtered, bubble or microemboli detection during cardiac imaging is a challenging problem due to the chaotic nature of bubbles, the circulation turbulence, the non-newtonian behaviour of blood, the interference between blood and bubble and also the side effects of endocardial boundaries and valves. On the other hand, the major weakness of echocardiographic modalities is their non-adapted nature for bubble recognition. Morphologically, a standard bubble shape is modeled as a sphere; however, sonographic behaviour introduces a longitudinal elongation in the visualization of bubbles. Therefore, bubbles are monitored as ellipsoids when they move separately. If a massive opacification is present, bubble shapes would not be regularly described mainly due to bubble overlapping, coalescence and turbulence.

Automatic detection and estimation of the functionality of CPFO or mainly the CCD exists since 50s using dye dilution techniques. During the 70s, improvements in medical imaging through ultrasound technology accelerated the process to reveal the secrets of microemboli and DCS. The first attempts were achieved using Doppler Ultrasonography. However, it was vulnerable to several factors such as application area, noise, subjectivity and low sensitivity. Moreover, different groups focused on echocardiographic images in bubble recognition for several aims; segmentation, noise reduction, candidate object recognition, microemboli grading and scoring tables. Both qualitative and quantitative approaches were proposed to cluster the degree of CPFO and DCS which is directly related with the number of bubbles. Even this problem was considered within other forms such as image and video records, an automated tool was not yet developed due to the algorithmic and mechanical challenges related to noise, monitoring and the variation between the observations. Therefore, a major problem in CPFO analysis and microemboli detection is the longitudinal analysis and

the examination of long lasting videos where the number and the size of intravascular microemboli change dynamically.

Our main hypothesis during this research is that automatic microemboli detection with proposed algorithms can be preferred to comprehend bubble behavior during post decompression phase within heart and diagnose interatrial aperture on contrast Trans Esophageal Echocardiogram (TEE) and Trans Thoracic Echocardiogram (TTE) modalities where noisy environment and subjectivity among clinicians would alter the final decision of CPFO treatment. Furthermore, we aim to introduce a computational procedure within conventional imaging modalities and to observe the sensitivity and specificity of each modality by comparing a double blinded clinical criterion.

In this thesis, Chapter II introduces the evolution of CPFO aperture after the birth, its main characteristics, its differences with similar CCD, main treatments and related diseases. Chapter III examines the nature of microemboli amd intravascular bubbles. It describes the formation of bubbles and main pathways which cause fatal diseases such as DCS. Chapter IV describes the methodology during this work regarding the qualitative, quantitative approaches and also through the comparison between recent algorithms and proposed techniques. Chapter V illustrates the results of all analysis. Finally, Chapter VI concludes the whole study by commenting prospective studies.

2. CARDIAC PATENT FORAMEN OVALE

In a Babylonian cuneiform tablet dating 2000 years, it is written that "When a woman gives birth to an infant that has the heart open and has no skin, the country will suffer from calamities". A medical interpretation of this saying reminds us a congenital heart defect; ectopia cordis which is commonly associated with interatrial defects; Atrial Septal Defect (ASD) and CPFO [12].

The postnatal development of heart was studied since Galen of Pergamon by different scientists [13, 14]. It is noted that post-natal cardiac development, foramen ovale and ductus arteriosus were firstly introduced in *De Usu Partium* of Galen in the second century. After Galen, Arabic scholars were interested in cardio-pulmonary system and discussed the existence of a visible passage between LA and RA [15]. Avicenna followed a similar approach of Galen at the end of 10th century. Ibn al Nafis commented the previous works and compared his findings in the book *Commentary on Anatomy in Avicenna's Canon* in 13th century [16]. During the Renaissance, Leonardo da Vinci intended also to represent the communication between right and left chambers in his illustrations of *Quaderni d'Anatomia* in Figure 2.1 by stating a perforating channel in 1513 [1]. Botallo who was an Italian surgeon working at the French royal court retook this passage between heart compartments and published *De caturrho* in 1564. In the 17th century, we remark that cardiac surveys increased via the experimental anatomy related to blood circulation and heart development. Formally, William Harvey; the famous english physician was the first researcher who introduced a modern approach of the separate right and left-heart circulations after the fusion of interatrial septum in 1628 [17, 18]. He followed a similar interpretation to the works of Botallo and was criticized by Domenico Marchetti (1639), Ceclio Folli (1639) and Pierre Gassendi (1640). In the 18th century, Albrecht von Haller who was a Swiss anatomist and physiologist studied Lutembacher syndrome which a special form of interatrial communication in 1750. In 1875, Karl von Rokitansky observed the pathology of ASDs and characterized different defects with their post-natal evolution [19].

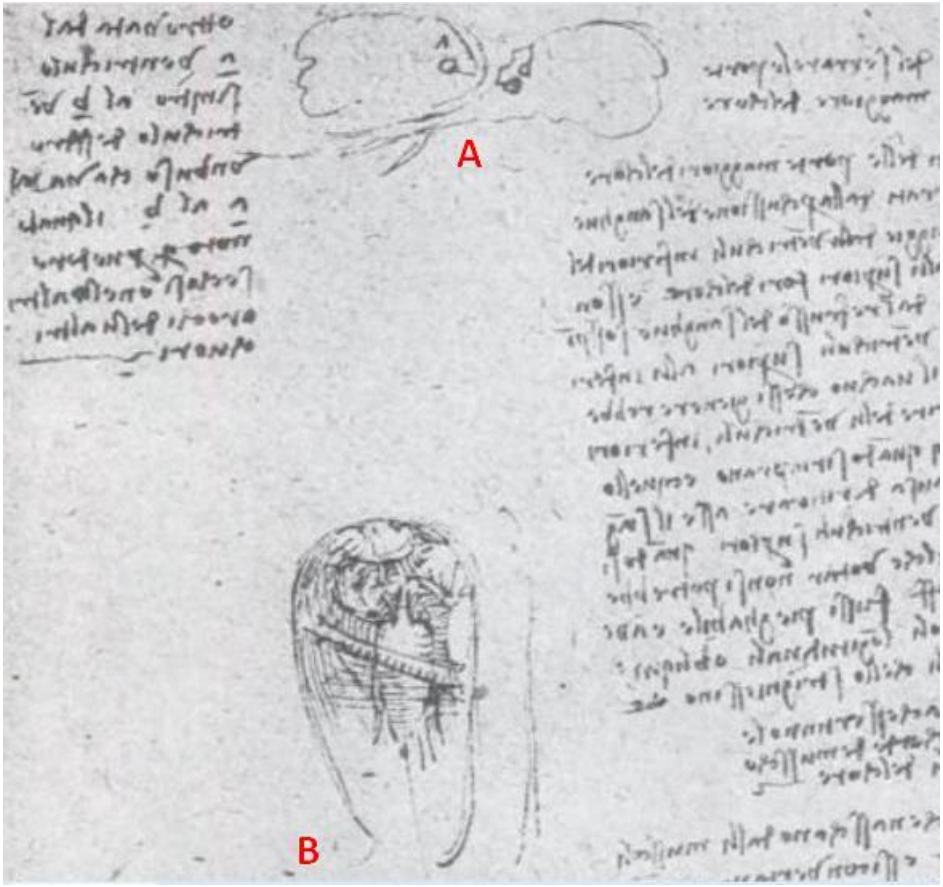

Figure 2.1 Sketches by Leonardo da Vinci [1]; A-CPFO communication, B-Right Ventricle.

In the 20th century, studies on CCDs increased through the radiologic development and imaging facilities. Marfan syndrome is one of the cardia abnormalities. In 1912, it is reported that a patient died at two and half months of age had this syndrome. In the postmortem observation it is found that the patient had mitral leaflet degeneration and CPFO [20]. Assman would be seen as a milestone in ASD and CPFO studies with respect to his findings in radiology [21]. In 1941 Bedford et al. [22] described the outline of ASD and CPFO types with radiologic and electrocardiographic landmarks. The analysis of normal and abnormal inter-atrial septum of Hudson [23] revealed a new rehearsal in atrial congenital shunts. Furthermore, recent researches followed his pathway to interpret ASD and CPFO with better imaging modalities and in *post-mortem* studies [24, 25, 26, 27]. Nowadays, congenital atrial defects are well known according to their anatomy, pathophysiology, genetical factors and epidemiology. However, its diagnosis, radiologic interpretation, grading, assessment and especially

a correct guidance in medical imaging are their challenges. Before going into the details of this problematic, it is crucial to get a brief introduction of heart evolution and to see the development of CPFO and ASD.

2.1 Congenital Atrial Diseases

The anatomical evolution in cardiac chambers begins in embryogenesis. Fetal lungs do not oxygenate blood but produce amniotic fluid. The blood may cross cardiac chambers without an interruption. Left and Right Atria (LA, RA) are not anatomically developed [28]. Normally, the heart would be visualized in the middle of the third week of fetal development.

After the birth, the beginning of breathing starts to fuse cardiac chambers regarding the pressure gradient. The septation process between chambers accomplishes the anatomical structure of a healty heart. Therefore, two atria are formed in the normal heart by a wall which is called atrial septum and also two ventricles separated with ventricular septum respectively (Figure 2.2).

On the other hand, hole-shape deformations, malocclusions which are characterized as septal shunts might be present on these septal walls. These malformations are identified as congenital diseases or defects regarding the severity and degree of these apertures. The major disease for atrial congenital defects is ASD. As a first study in this field, Lang et al. [29] investigated post-mortem cases and found the prevalence of ASD as 1%.

Corno et al. [30] investigated congenital atrial septal defects within two categories; true defects and interatrial communication. A schematization of atrial defects is represented in Figure 2.2. True atrial septal defects are identified through the floor of the fossa ovalis. When the flap valve moves the defect can be distinguished within the fossa. This type is called ostium secundum or secundum atrial septal defect. The valve movement would overlap but an automatic seal does not occur. The epidemiology of

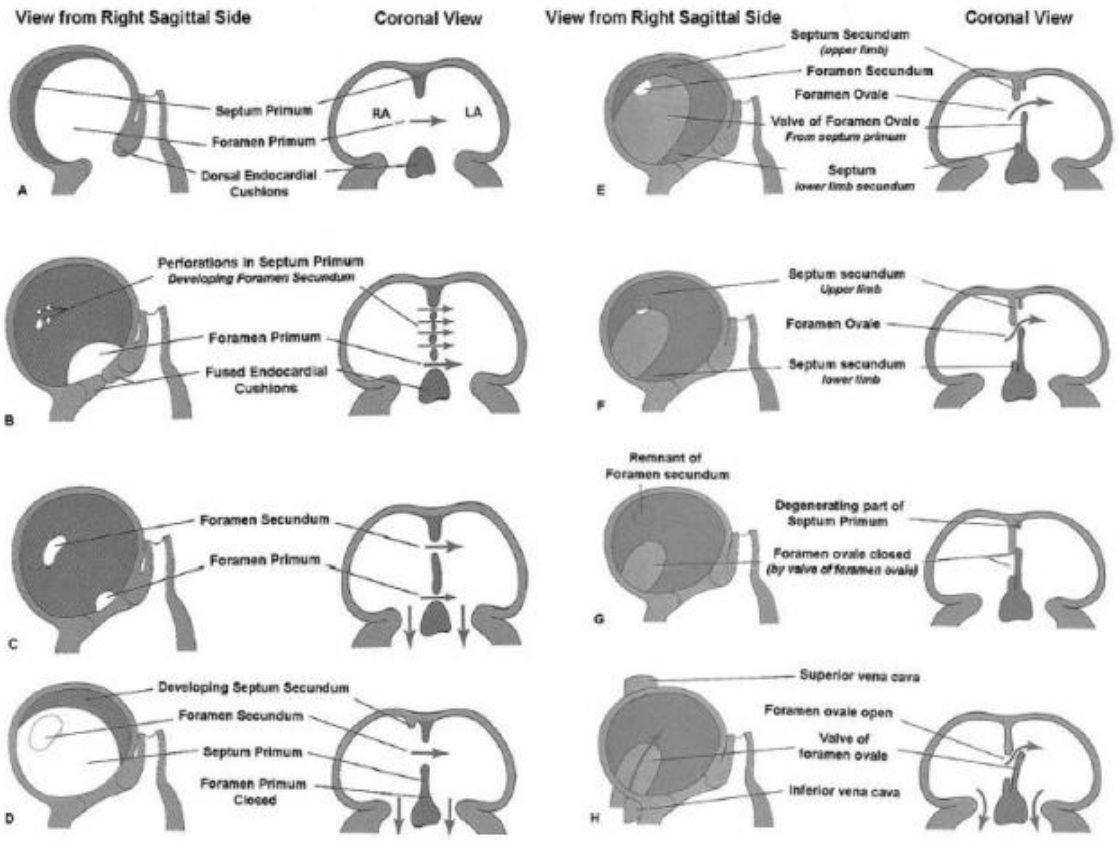

Figure 2.2 CPFO development from embryology from Hara et al. [2].

this form is higher as 70%-77% of all defects within atria [31, 32].

Second true ASD is identified as ostium primum type. It exists between the leading edge of the atrial septum and the upper margin of the ventricular septum. This class is also categorized into the atrioventricular defects due to its anatomical location. It consists 20% of ASD forms [32].

Interatrial communication for ASD is described into two categories; sinus venosus and coronary sinus. Sinus venous are localized usually at the superior part of vena cava. In some cases, it would be outside the floor of the fossa ovalis, near to the inferior part of vena cava. Coronary sinus exists through the mouth of the sinus. It is generally identified as a large shunt which separates the sinus and LA.

Partial anomalous pulmonary venous connection, mitral valvar prolapse, patent

ductus arteriosus, pulmonary valvar stenosis, peripheral pulmonary arterial stenosis, and persistence of the left superior vena cava are also classified as interatrial communications in the form of lesions [30].

The septation process after birth would never occur in 25-35% of subjects in a regular population [28, 33, 34]. It is generally accepted that approximately 1/3 of healthy people may have a CPFO but this percentage may tend to increase in specific groups with migraine or embolic events [35, 36].

Even CPFO and ASD are generally confounded, they are discriminated through the size, nature and duration of atrial aperture. For this purpose, clinicians use flow measurements, contrast enhanced visualization, manual measurement of shunts. As a standard, if atrial aperture is above 5 mm and open, congenital defect is characterized as ASD and the surgical treatment is advised [37].

Even ASD is more clearly studied due to its severe consequences; CPFO is not considered as a congenital disease but as a defect till last decades. Nowadays, there are still confusions in terms of its classification [38, 39, 40]. Even if Drighil et al. [41] introduced CPFO as an emerging new disease by its implication related to stroke and other complications, they remarked that most of the people with CPFO will never have any symptoms. However, its consequences, its relationships and its side effects are more quantitatively observed in depth through postmortem and clinical studies. In review papers, it is remarkable to note that there is an exponential growth to induce CPFO with several cases [33].

On the other hand, CPFO diagnosis is generally not done with the measurement of shunt size. The shunt is closed in normal pressure conditions if subject does not cough, strain, sing, yell, perform a manoeuver or strenuous activities. Therefore, an extra activity is required to trigger CPFO, open the shunt like a door and measure its activity. Nevertheless, the anatomical visualization does not bring information how this shunt is active physiologically. Therefore, a detailed procedure is required clinically for its examination.

In one of the most cited studies of CPFO literature, Hagen et al. [42] observed CPFO size in 965 autopsy specimens of human hearts to reveal a detailed significance of aperture. They found CPFO range between 1-19 mm in 263 specimens and a tendency to increase in CPFO size with ageing from a mean of 3.4 mm in the first decade to 5.8 mm in the tenth decade of life. On the other hand, Foster et al. [33] range CPFO diameter from 1 to 19 mm with a mean 4.9 mm.

Even if CPFO-microemboli relationship is generally expressed as the opening or the closure of the shunt, the measurement of total number of bubbles would be a good scale to observe the functionality of CPFO. At the same time, this functionality is highly correlated with the surface area of interatrial shunt. Penther [43] found that the average surface of CPFO area was 0.5 cm^2 (range between 0.2-1.5 cm^2).

The genetic factor in CPFO incidence was investigated by Arquizan et al. [44] to respond if "*CPFO is a family trait*". They reported that there was 3.6 times more CPFO in siblings of stroke patient with a CPFO than in siblings of patients without a CPFO. They concluded that the familial aggregation is higher in females and CPFO may contribute to genetic susceptibility to stroke. This hypothesis was retaken into account recently. Posch et al. [45] studied coding region of TBX20 in 170 subjects with CPFO&ASD and revealed the mutation effect of this region on congenital atrial defects. Briefly, this topic still arises in order to discover the concrete relationship between CPFO-ASD and genes with new experiments on animals and transcription factors [46, 47, 48, 49, 50]. The genetic factors for CPFO and ASD types would be summarized as follows in Table 2.1. Germonpré et al. [51] reported the changing prevalence of CPFO through time in a pioneering study for scuba divers.

2.2 CPFO Related Diseases

Over the last decades, it is remarkable to note that CPFO studies were mostly done in *post-mortem* or anatomical studies [33]. Therefore, it would be inferred that CPFO is considered as a silent congenital defect which is not associated with a systemic

Gene	Chromosomal location	Cardiac defect
ALK2	2q23-q24	ASD type I
BMPR2	2q33	ASD,PFO
CITED2	6q23.3	ASD,PFO
CRELD1	22p13	ASD type I
GATA4	8p23.1-p22	ASD,PFO
KRAS	12p12.1	ASD,PFO
MYH6	14q12	ASD type II
NKX2.5	5q34	ASD,PFO
NKX2.6	8p21	PFO
TBX5	12q24.1	ASD,PFO

Table 2.1
Gene mutation and phenotype for ASD & CPFO from *Clinical Cardiogenetics* [11].

or paradoxical disease.

Firstly, Cohnheim [52] developed a hypothesis to combine CPFO shunt and pradoxical embolism in a study with a *post-mortem* stroke case. Cabanes et al. [53] studied the prevalence of ASD, CPFO and mitral valve in 100 consecutive patients with ischemic stroke.

On the other hand, a detailed survey in stroke and microemboli started to reveal the adjunct effect of CPFO especially in an environment where air pressure changes drastically. The pressure gradient is a vital parameter for circulation and cardiopulmonary system. When a drastic change of air pressure in surounding environment occurs, microemboli starts to form in extravascular and intravascular platform. Astronauts performing extravehicular activities under hypobaric environment, pilots at high altitudes and divers under hyperbaric conditions are the subjects who suffer the problems related to microemboli creation. It is noted that hypobaric conditions are less risky than hyperbaric in terms of DCS [54]. Though the change of pressure gradi-

ent triggers mostly DCS, the symptoms and diagnosis are observed within two major types.

- Type I DCS covers musculoskeletal pains especially the skin and lymphatic nodes.
- Type II DCS involves serious symptoms including neurologic and cardiologic systems.

When a CPFO shunt is larger ($\approx$ 5 mm) and an large amount of microemboli ($\geq$ 20 bubbles in a single frame according to Germonpré et al. [55] criterion), cerebrovascular events would be associated with this congenital defect [56, 57].

If venous gas embolism occurs, as a result of decompression, a CPFO will be a risk factor for paradoxical arterial embolism and its sequelae [28, 55, 58, 59]. Torti et al. [60] showed in 250 scuba divers that the presence of a CPFO was related to a low absolute risk of suffering five major DCS events per 10 000 dives, the odds of which however were five times as high as for divers without CPFO. Waligora et al. [61] identified CPFO as a risk of Type II DCS for astronauts as well.

Bigal et al .[62] reported a positive association between CPFO and migraine with aura. Even the direct relationship between migraine and CPFO has not been demonstrated there are some hypoytheses to combine them [63];

Firstly, paradoxical emboli were found suspicious for causing cortical dysfunction due to the terminal branches of basilar artery [64, 65, 66, 67]. This hypothesis was supported with the findings of migraineurs with aura. Furthermore, migraineurs with aura were found more risky to ischemic strokes [68, 69, 70]. The incidence of subclinical brain lesions were found 13.7 times higher in migraineurs [71]. The brief report of Woods et al. [72] supports these results by showing a perfusion decrease in cerebral cortex.

Secondly, another hypothesis based on the plasma coagulation factors and hy-

poperfusion was introduced. This hypoxia theory was favored with the existence of CPFO by Sztajel et al. [73] as a trigger of migraine with aura with propagating hypoperfusion.

Finally, the interaction betwwen *vasoactivators* and monoaminooxydase would trigger migraine attacks [65, 74]. This effect would be increased if a right-to-left shunt might cause a direct circulation of *vasoactivators*. Another hypothesis supports that microemboli would activate thrombocytes which consolidate the migraine pathogenesis due to 5-hydroxytripyamine (a monoamine neurotransmitter) [75, 76].

Raymond-Martimbeau [77] identified sleep apnea, pulmonary hypertension and stroke as other risks associated to CPFO. Hacievliyagil et al. [78] revealed a meaningful prevalence of CPFO in patients with chronic obstructive pulmonary disease and associated CPFO as a leading factor of hypoxemia.

The relation between CPFO and hypoxemia following lung surgery due to to platypnea-orthodeoxia syndrome has been described and surgical shunt closure has been proposed [79]. Recent research revealed the increasing importance of CPFO closure. Surgical operations are encouraged for risky groups such as divers, pilots and astronauts.

Nowadays, migraine, cerebral ischemia and paradoxical embolism which are related with CPFO are also surgically treated. CPFO would cause also severe problems such as monocular blindness related with retinal artery occlusion [80, 81, 82], hemianopia (decrease in visual field) [83] and sudden deafness [84, 85]. There are however discrepancies about how and when to diagnose CPFO and discussions about a golden standard in terms of quantification and classification.

2.3 Decompression Sickness

In professional and recreational diving, several medical and computational studies are developed to prevent unwanted effects of decompression sickness. Diving tables, timing algorithms were the initial attempts in this area. Even if related procedures decrease the physiological risks and diving pitfalls, a total system to resolve relevant medical problems has not yet developed. Most of the DCS and side effects are classified as unexplained cases though all precautions were taken into account. For this purpose, researchers focus on a brand new subject; the models and effects of micro emboli. Balestra et al. [28] showed that the prevention of DCS and strokes are related to bubble physiology and morphology. On the other hand, studies between inter subjects and even same subjects considered in different dives could cause big variations in post decompression bubble formations [86].

2.4 Medical Imaging for CPFO and Microemboli

Cardiac imaging is always a big challenge in most of the imaging technologies due to several factors. Initial medical interpretation of CPFO or mainly CCDs was the dye dilution technique [87, 88] and ear oximetry [89]. Even these methods are still in use since 50s, better imaging approaches were introduced in 70s. Ultrasonography which is preferred as most widely applied imaging technique to see cardiac functions and anatomy became as the principal tool for diagnosis of CPFO and CPFO related diseases. A better understanding of CPFO regarding ultrasonography and other imaging modalities would be summarized as follows;

1. **Doppler Ultrasonography**: During the last three decades, bubble patterns were analyzed in the form of sound waves and recognition procedures were built up using Doppler ultrasound. First attempts of bubble monitoring were based to the Doppler effect of ultrasound modality in 70s and 80s. This approach and its automatization were mostly preferred due to the limitations of B-Mode and the

cost of hardware. Rubissow et al. [90] showed the development and location of microscopic bubbles as small as 5 microns in 1971. In different studies [91, 92], this practical and generally handheld modality is always preferred for post decompression surveys. However, these records are limited to venous examinations and all existent bubbles in circulation would not be observed. The noise interference and the lack of any information related to emboli morphology are other restrictions. Doppler ultrasound is also used as a tool to detect free air bubbles during extracorporeal circulation where the blood is oxygenated mechanically [93].

Nowadays, three modalities of ultrasound transthoracic echocardiography (TTE), transesophageal echocardiography (TEE) and transcranial Doppler (TCD) are mostly preferred to count bubbles and to diagnose congenital and cerebrovascular events. The preference depends to the application area, the patient, severity of the case and accuracy of the detection.

Di Tullio et al. [94] showed the performance of three methods in terms of their sensitivity and specificity as a pioneer study. Even TEE became the primary tool to detect atrial congenital defects regarding its high sensitivity in different studies [95, 96, 97, 98, 99, 100, 101], it should be taken into account several criteria; the visualization setup of recording media, the experience of clinician with correct manoevers and especially knowledge of visual bubble identification and tracking.

The experimental studies emphasized the importance of B-mode (Brightness mode) in ultrasound which gave rise to the development of echocardiographic modalities and the microembolic research within this modality.

2. **Trans Esophageal Echocardiogram**:Nowadays, TEE proved its superiority with respect to other modalities. Even the use of TEE requires a speciality due to probe localization, fasting and topical anesthesia of the patient. Despite its relatively invasive procedure, it is considered a golden standard for detection of right-to-left shunts and CPFO [3]. For contrast enhanced shunt detection several agents are in use but agitated saline is the most preferred agent thanks to low cost and good contrast. Agitated saline is prepared with 9 ml of saline and 0.1 ml of air which are pushed back and forth 10 times in a double syringe system to obtain

an homogenous opaque solution. Other contrast agents are Dextrose 5% (water D-galactose microparticle solution), Urea-linked gelatin and Oxypolygelatine.

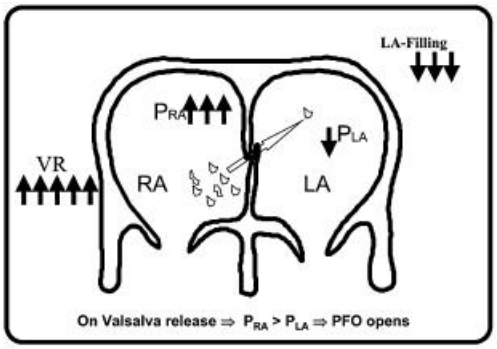

Figure 2.3 Mechanism of unrevealing right-to-left shunt by Valsalva manoeuvre, an arrow with head up means increase and head down is decrease, number of arrows represent how much is the change [3]. P_{LA}: left atrial pressure, P_{RA}: right atrial pressure and VR: venous return.

3. **Trans Thoracic Echocardiogram**:In TTE, clinician try to focus on Interatrial septum (IAS) wall and localize possible suspected shunts with color flow doppler [102]. After the initial inspection, atrial chambers are monitored. Several views would be used to show congenital defects on IAS. Subcostal four chamber (SC4C) and Apical four chamber (A4C) views are considered as the optimals for atrial congenital shunts. SC4C uses the perpendicular orientation to ultrasound scan plane. Parastenal Short Axis-Aortic Valve Level (PSAX-AVL) View is also another type to visualize congenital defects regarding cross sectional insights to chambers and aortic valves. It is generally used before applying A4C view in cTTE. Inspectetion with color flow doppler in IAS can usually reveal a possible shunt in IAS expect the smaller ones. Neverthless, the information generally remains anatomical in terms of aperture size and metrics. Therefore, a detailed examination using contrast modality is required to show shunt activity and grade.

4. **Trans Cranial Doppler Ultrasonography**: Brucher et al. [103] focused on this problem with a newer modality in this field; multifrequency TCD. They developed a system of automatic detection between 2-2.5 MHz. Improved imaging techniques in TCD facilitates microemboli detection in cases related to stroke. TCD is generally preferred for patients who have stroke in order to examine bubbles with small diameters. On the other hand a direct diagnosis of CPFO

would not necessarily imply a CCD [96]. Therefore, TCD monitoring would not guarantee the existence of CPFO. However, a standardized application of Valsalva maneuver would tend to increase the detection sensitivity [104]. Anzola [105] stated the important role of CPFO in a number of non-stroke conditions (such as migraine and the occurrence of attacks of transient global amnesia)and noted the utility of this modality as a simple diagnostic technique for right-to-left shunts. Stendel et al. [106] noticed that TCD would be a better technique than TTE for the monitoring of CPFO and the related venous air embolism.

Automatic embolus detection was also considered as a challendge within TCD. Several studies were focused on this problem and the agreement between the human experts [107, 108]. During TCD monitoring, embolic signals are characterized as an unidirectional intensity increase within the Doppler frequency spectrum [109]. At the same time, these signals occur randomly and they would be identified by a characteristic *chirp*, *click* or *whistle* sound. Even though automatic approaches tend to show feasible findings, these systems would be vulnerable to adaptive nature of embolus. Consequently, better methods would be developed by considering the advices of the human experts and the embolus quantifiers such as the spectral range and the noise.

2D Echocardiography which is available in portable forms serves as a better modality in cardiologic diagnosis. Clinicians who visualize bubbles in cardiac chambers count them manually within recorded and frozen frames. This human eye based recognition would cause big variations between trained and untrained observers [110]. Recent studies tried to resolve this recognition problem and to reduce the subjectivity by an automatization in fixed region of interests (ROI) placed onto Left Atrium (LA) or pulmonary artery [5, 111]. Moreover, variation in terms of pixel intensity and chamber opacification were analyzed by Norton et al. [112] to detect congenital shunts and bubbles. It is obvious that an objective recognition in echocardiography is always a difficult task due to image quality. Image assessment and visual interpretation are correlated with probe and patient stabilization. The experience of clinicians, acquisition setup and device specifications would also limit or enhance both manual and

computational recognition. Furthermore, inherent speckle noise and temporal loss of view in apical four chambers are major problems for computerized analysis.

Several imaging modalities such as Doppler and Intravascular Ultrasonography, contrast Echocardiography, Magnetic Resonance Imaging (MRI) and Computed Tomography (CT) are proposed for CPFO visualization and grading. Contrast Echocardiography becomes the golden standard for its portability and imaging quality [113]. Even if some speculations lower the CPFO diagnosis through the echocardiography in terms of false positives, Balestra et al. [28] emphasized the importance of proper maneuvering during imaging and diagnosis. On the other hand, it is not only important to diagnose the existence of CPFO; the assessment of its size is a crucial step in determining the need for closure as well. For this purpose, it is important to note that contrast enhanced Doppler ultrasound detects right-to-left shunts more sensitively, but it is unable to locate the hole as with echocardiography [113].

Until the recent developments, CPFO diagnosis with Magnetic Resonance Imaging was not feasible due to poor spatio-temporal resolution and the lack of the measurement through shunt openings [99]. Actually, Cardiovascular Magnetic Resonance (CMR) Imaging is preferred in congenital atrial defects especially for elder people and suboptimal views in echocardiography [114].

In 2005, Mohrs et al. [115] tried to show the feasibility of dynamic contrast in CMR combined with Valsalva manoever as a noninvasive method to diagnose CPFO and ASD. They adapted a grading level regarding CPFO severity in the same pilot study through signal-time curves in LA and PA. Same group [97] performed a similar comparative analysis in patients after CPFO closure and concluded that even MRI cannot replace TEE for the exclusion of potential embolic sources, it would be feasible as a non invasive procedure.

Nusser et al. [98] performed a longitudinal survey in 75 patients with cryptogenic ischemic events, before and after the closure of atrial shunt. They found that accurate PFO detection with CMR was two times lower than TEE. Moreover, Hamilton-Craig et

al. [99] pointed out a similar finding in 25 subjects with cryptogenic ischaemic stroke that CMR is less sensitive than cTEE. Even CMR would offer better contrast and intensity for the analysis of cardiac anatomy and functionality, time-signal intensity curves would lessen the sensitivity of PFO existence. Therefore, it is remarkable to state that cTEE combined with a good manoever (Valsalva or high strain Valsalva) would still offer a better diagnosis in CPFO compared to CMR.

CT or Spiral CT which are less applied modalities in the diagnosis of CPFO and the detection of cardiac sources of embolism are currently in use with their own grading systems. Even the pioneer papers of CT in emboli studies are dated back to the second half of 90s, it is remarkable to note that clinical application of CT and Spiral CT are so recent.

2.5 Bubble Analysis and Grading for CPFO Characterization

In medical reserch, microemboli analysis and CPFO grading evolved separetely from each other. Even if microemboli and CPFO relationship are mostly taken into account in diving physiology and hyperbaric medicine, there is a broad range of CPFO grading regarding the imaging modality.

In this part, microemboli grading and CPFO grading terms define the same medical expression; the functionality of IAS or basically how this shunt would open. As we would recall from the introduction, CPFO is considered as an anatomical and functional flap. Even though Schuchlenz et al. [116] suggested that aperure measurement would be more objective than the injection of a contrast medium especially saline contrast with TTE and TCD. The lack of standardization in bubble size which varies between 24-144 μm was the main remark which effects the signal power in ultrasound technology. Neverthless, this point of view is questionable if the functionality of CPFO is taken into account. The reason why this shunt opens is not the microemboli dimension but the relative microemboli quantity passing through the right-to-left aperture. On the other hand, the injection of bubble or contrast medium reveals its activity so

describes the functionality and physiology of congenital disease. It is not possible to discriminate how interseptal aperture is active without injection. For this purpose, functional grading techniques were developed according to these contrast media.

During our thesis, the measurements and analysis were performed using the ultrasonographic modalities; contrast TTE and contrast TEE. In this section we will review briefly the main techniques of CPFO grading especially in ultrasonography and echocardiography and also prospective techniques introduced with MRI and CT.

In a clinical environment, CPFO diagnosis is achieved with the monitoring of the existence or the non-existence of a shunt aperture on the echocardiographic frames. However, it is obvious that the contrast agent and the maneuver are crucial to stimulate the shunt [28]. The passage of bubbles are also essential to characterize the functionality of right-to-left shunts (RLS), especially CPFO. In general, specialists determine CPFO and measures its functionality using a visual-manual tool on frozen frames by the counting of microemboli crossing IAS. Bubble detection is the crucial step of the evaluation since the grading is achieved with reference to the number of right to left passing bubbles per cardiac cycle. Usually, three heart beats are taken into account as a convention when a visual interpretation of cardiac chamber is achieved.

Even if several grading algorithms [5, 55, 117, 118] were developed by different groups to classify bubble numbers, Eftedal et al. [5] attempted firstly to analyze video frames to detect bubbles. In this pioneer research, post decompression bubbles were counted within a user defined window that was placed manually on the ultrasound frame over right ventricle and pulmonary artery. Because of the lack of dynamic boundary detection, their method needed a very stable position of the ultrasound probe that could only be achieved with anaesthetized animals. The second approach is developed qualitatively by Norton et al. [112] using the contrast change called as opacification before and after injection and detected the CPFO existence without grading. Therefore, it is remarkable to note the lack of an automatic computational analysis in atrial congenital diseases and bubble detection.

Grade	Description
0	No bubble signal
I	Few bubble signal in some cardiac cycles
II	Many bubble signals in less than half cardiac cycles
III	Many bubble signals in most cardiac cycles
IV	Maximum bubble signal in continous form during cardiac cycles

Table 2.2
Spencer grading code.

During the analysis of CPFO recordings and bubble quantification, we adapted a similar reasoning proposed by Germonpré et al. [55] in Table 2.5. This method which is commonly in use during the observation and the detection of congenital defects has a relatively narrow scale than the previous grading codes. The first degree with 0 bubble represents the no-CPFO. The second and third degree are separated with a threshold (20 bubbles). For this purpose, our manuscript and related studies enlisted in Appendix were prepared using the nomenclature of Type I-CPFO (less than 20 bubbles) and Type II-CPFO (≥ 20) bubbles.

Eftedal et al. [110] developed a grading system to measure the agreement between trained and untrained observers. The amount of bubbles was graded according to a non-linear grading system with six levels as it is represented in Table 2.6. They showed that untrained observers perform equally as well as trained observers the manual detection and grading of bubbles.

As an alternative, Mohrs et al. [115, 97] used a CPFO grading system in their pilot study with MRI. This system is composed of 4 levels based on signal-time curves acquired through PA and LA. Similar to Eftedal et al. [5, 111] two manually fitted ROIs were placed without changing the size in every image.

- **Grade 0:** No contrast enhancement in the LA before the contrast agent reached

Code	Frequency	Percentage/Duration		Amplitude
	Bubbles per cardiac cycle	Cardiac cycles at rest(%)	Movement,duration cardiac cycles	
0	0	0	0	No bubbles
1	1-2	1-10	1-2	Barely perceptible; A(B)«A(C)
2	several,3-8	10-50	3-5	Moderately perceptible; A(B)<A(C)
3	rolling drumbeat$\geq$ 9	50-99	6-10	Loud; A(B)$\approx$A(C)
4	continous	100	>10	Maximal; A(B)>A(C)

Table 2.3
Kisman-Masurel grading code.

the pulmonary veins.

- **Grade 1:** Only slight contrast enhancement close to the atrial septum without enhancement of the entire LA before the contrast agent reached the pulmonary veins.
- **Grade 2:** Only slight contrast enhancement in the LA before the contrast agent reached the pulmonary veins.
- **Grade 3:** Bright contrast enhancement in the LA before the contrast agent reached the pulmonary veins.

CT modality would be considered as the less commonly used imaging technique for CPFO detection and microemboli grading. Even though there are more researches of ASD with CT, CPFO studies are dated back to the 90s. Williamson et al. [119] proposed a CT criteria for the detection of CPFO as follows;

- **Criterion 1**: Presence of a distinct flap in the LA at the expected location of the septum primum.

Spencer Code	Kisman-Masurel grading code
0	0
I	111/I- 112/I 113/I 211/I- 212/I 213/I+
II	121/I+ 122/II 123/II 221/II- 222/II 223/II+
III	232/III- 233/III 242/III 243/III 332/III 333/III 342/III+ 343/III+
IV	444/IV

Table 2.4
Conversion table between codes.

Grade	Description
0	No bubble passage
I	No or slight(less than 20) bubble passage
II	important (≥ 20) bubble passage

Table 2.5
Germonpré grading code.

- **Criterion 2**: Presence of a continuous column of contrast material between the septum primum and septum secundum, connecting the LA and RA.
- **Criterion 3**: Presence of a jet of contrast material from the column into the RA.

On the other hand, this grading method does not bring a direct relationship between microemboli and CPFO like MRI alternative. However, it would be seen as an indicator of shunt morphology and functionality regarding the contrast medium in CT.

The purpose of our current research is to offer an easy and reliable tool to quantify bubbles in cardiac chambers which will give us the CPFO motility and activity. It is also indispensable to fulfill computational gap in bubble analysis. The dynamic extraction of LA and automatic counting reveal the activity of septal shunt

Grade	Description
0	No observable bubbles
I	Occasional bubbles
II	At least one bubble every four heart cycles
III	At least one bubble every heart cycle
IV	At least one bubble per cm^2 in every image
V	White-out, single bubbles cannot be discriminated

Table 2.6
Eftedal-Brubakk grading code.

through bubbles in order to assess the CPFO using both cTEE and cTTE. We also suggest that standardization in CPFO using the comparison between existent procedures would offer a better diagnosis. Performance analysis reveals that our approach is satisfactory through false alarms. We hypothesize that our method provides better detection rates and increases the clinician subjective ease-of-use in terms of decision making in recognition.

One of the current methods for CPFO detection clinically in use is counting the bubbles crossing the septal aperture on echocardiography. Even Spencer and Kisman-Masurel grading code (given in Table 2.2 and 2.3, respectively) are used within Doppler Ultrasonography for microemboli counting, Germonpré grading code is preferred within echocardiography (Table 2.5). For Spencer and Kisman-Masurel grading codes, a conversion table (Table 2.4) is also developed in order to make a correspondce between 3 to 5 level systems.

The specificity of contrast Transthoracic Echocardiogram (cTTE), contrast Transoesophageal Echocardiogram (cTEE)and Transcranial Doppler are very high but the best sensitivity is obtained with cTEE. On the other hand, the cTTE and transcranial Doppler sensitivities were found to be as low as 47% and 65% respectively [94]. cTEE is the best invasive method for detection even though probe swallowing may cause discomfort for patients.

The functional size and activity of CPFO can be correctly determined by counting the bubbles. Automatic counting of bubbles in ultrasound images has been attempted by Eftedal et al. [5, 111] to estimate the decompression stress. However, their method is based on user defined constant window that was placed manually over the right ventricle and the pulmonary artery. Because of the lack of dynamic boundary detection, their method needed a very stable position of the ultrasound probe that could only be achieved with anaesthetized animals. The second approach is developed by Norton et al. [112] using the contrast change (opacification) before and after injection and detected the CPFO existence without grading.

In order to analyze a relevant frames, the role of an accurate maneuver should also be taken into account. Several procedures are applicable to stimulate IAS. However, their use would differ and may cause variations for CPFO characterization. Balestra et al. [28] cited six different maneuvers to generate bubble passage between two atria as it follows;

- Gentle Valsalva; Ordinary maneuver to equalize the middle ear pressure
- Forced Valsalva; Maximal Valsalva maneuver in a repeated way to equalize the middle ear pressure
- Calibrated Valsalva; Gradually increasing Valsalva maneuver
- Cough; Forceful coughing
- Knee Bend with Valsalva; Knee bending during breath hold
- Free Exhaling Knee Bend; Knee bending without breath hold

2.6 CPFO Closure

As CPFO is considered as a beauty spot [39, 120] or silent defect [121], its closure could not be taken into account as a primary solution for each person having

this shunt. In their review paper Drighil et al. [41] indicated the following steps before the final decision of the eligibility of CPFO closure and noted that the first four steps are essential;

1. Recurrent ischemic stroke with antiplatelet agents.
2. Age under 60 years and absence of overt atherosclerotic disease or more than one atherosclerotic risk factor.
3. Exclusion of other cardiac (atrial fibrillation, endocarditis, tumour) or vascular (carotid stenosis, spontaneous carotid or vertebral dissection, aortic atheromatosis) embolic sources.
4. CPFO with high anatomic risk: important inducible shunting and large CPFO, spontaneous right-to-left shunt at rest, long tunnel, ASD, Eustachian valve.
5. Contraindications against or unwillingness to undergo anticoagulation.

It is important to note that CPFO closure requires a lifelong implant [122]. Even if medium and long-term follow-up data are found encouraging for CPFO closure, there are no very long-term (more than 10 years) follow-up data available.

Over last two decades, CPFO treatment was debated for correct assessment of percutaneous closure techniques. The first transcatheter closure of a congenital defect was a closure of patent ductus arteriosus(PDA) in 1971 [123]. Similar techniques were adapted for the closure of ASDs in 1976 using a double disk device. Furthermore, Rashkind started to develop several types of PDA occluders (single and double forms) which is actually called as *Rashkind Umbrella* [124, 125]. Lock et al. [126, 127, 128] were the first group who tried to close in large numbers of congenital defects such as ASD, CPFO and Ventricular Septal Defect (VSD) using a new occluder *Bard Clamshell Device* [129, 130, 131, 132].

Nowadays, several techniques of surgical closure exist to undergo CPFO treatment. However some critical questions arise in the choice of occluder and the steps

before and after the surgery are still discussed regarding the advantages or side effects of these new devices.

Recent studies on migraine, cerebral ischemia, paradoxical embolism [34, 133, 134] suggested transcatheter closure of CPFO as a clinical intervention for associated problems. Which type of CPFO should be managed surgically, which closure device is ideal for which CPFO and related diseases (migraine, ischemia, embolism) complicate surgical steps. Although latest occluder technologies bring reliability and less side effects, a detailed examination of patient history must be taken into account to determine the correct procedure.

The overall success rate for CPFO closure using new and the most common closure devices was reported 99%, whereas the average risk of major complications was 1% [135]. According to Hara et al. [2] different technologies are available to occlude interatrial shunts as it is represented in Figure 2.6.

After implantation, a significant decrease in transient ischemic attack, stroke and peripheral emboli is reported [34, 133]. However, there are still discrepancies about how and when to diagnose CPFO [94].

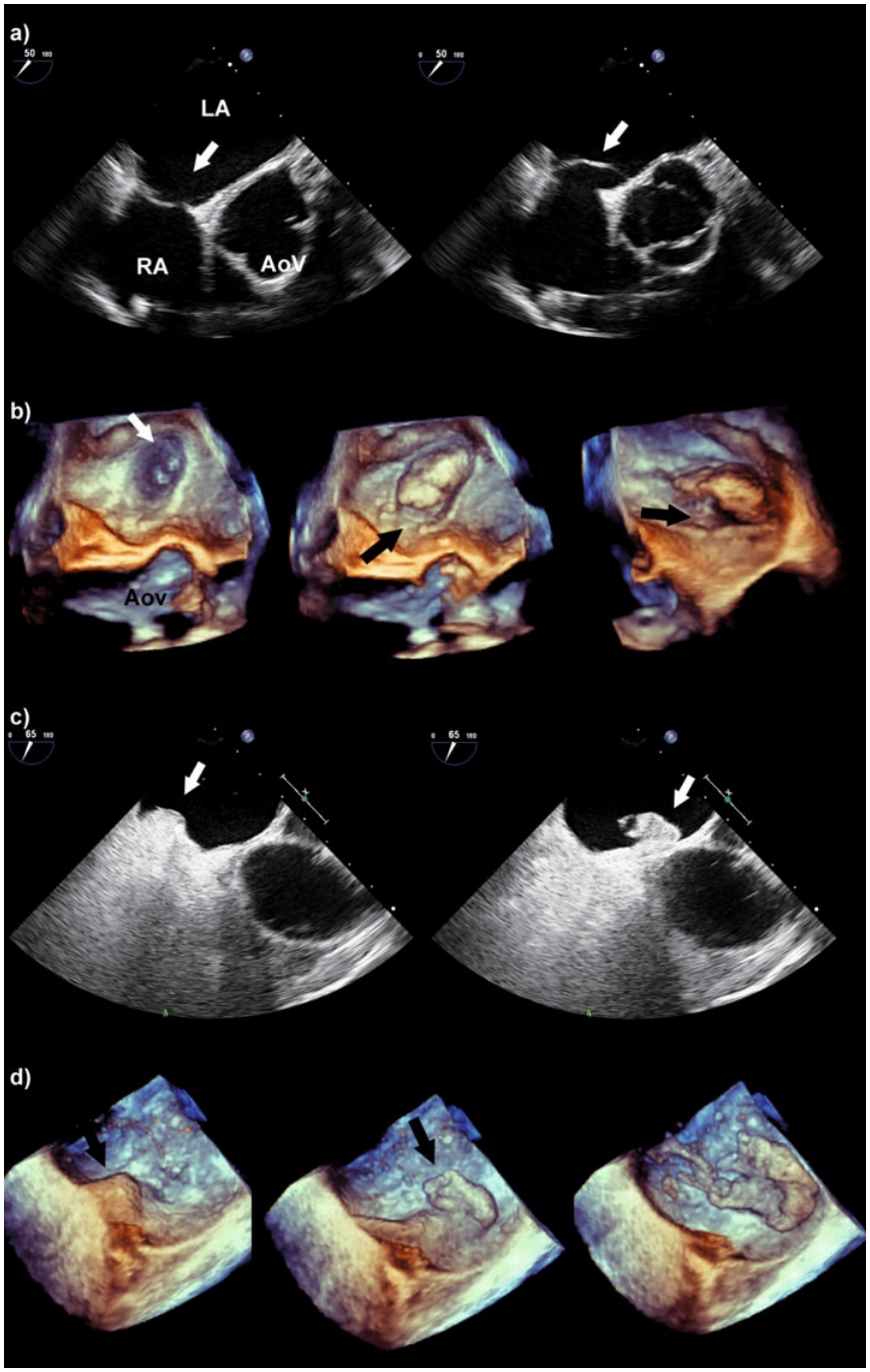

Figure 2.4 Type 2 CPFO with excessive contrast passage. (a) The 2D TEE shows an interatrial septum (IAS) aneurysm (white arrow) in aortic valve (AoV) short-axis view. (b) In live 3D zoom images, the complete IAS is shown with the fossa ovalis bulging towards the RA (left, white arrow) and detection of the PFO when the IAS is bulging towards the LA (black arrow). (c) 2D TEE proved the PFO by demonstration of IAS bulging toward the LA (left, arrow) with contrast passage across the IAS (right, arrow). (d) Live 3D zoom provided a 3D view of the entire LA space showing the IAS bulging (left, arrow) and the cloud of contrast bubbles passing through the IAS [4].

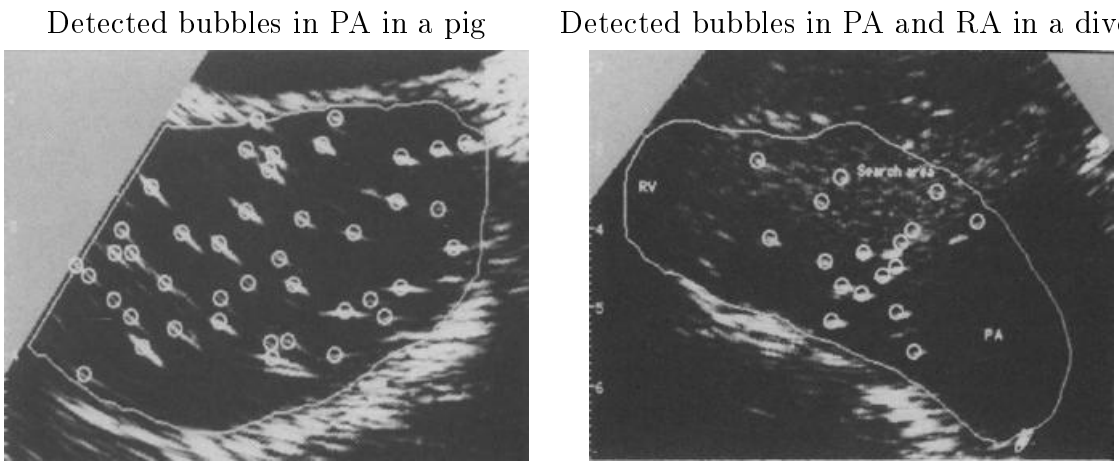

Figure 2.5 Detecting intravascular gas bubbles from Eftedal et al. [5]

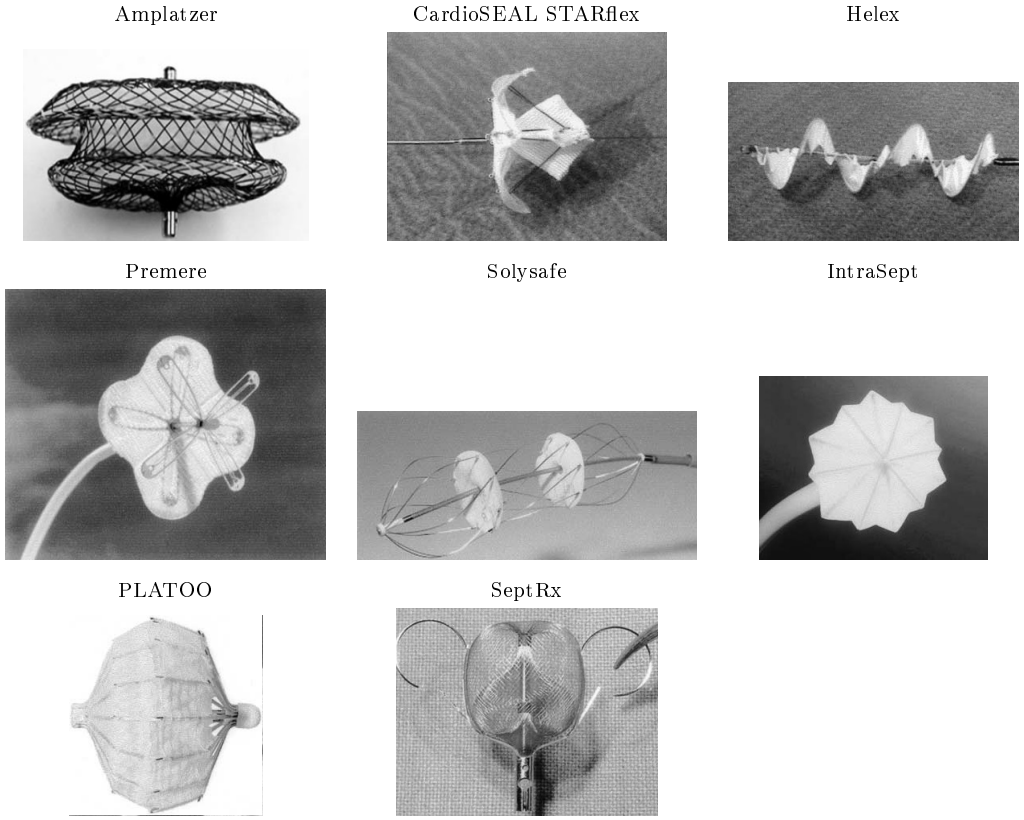

Figure 2.6 Different types of CPFO occluders [6].

3. RELATIONSHIP OF MICROEMBOLI WITH CPFO

In order to comprehend how microemboli and CPFO are related, it is important to formulate how bubble and microemboli are taken into account regarding their significance, behavior and role. In general, both terms are frequently used to represent an encapsulated substance-mass within an environment. However, this encapsulation is generally limited to air or gas filled structures. The surrounding environment and structure interaction would be occasionally a gas-to-gas, a liquid-to-gas or a solid-to-gas interaction. Obviously, the last one would not permit a free movement of bubble.

Bubble is a general identifier to designate the kernel of this interaction in all disciplines. On the other hand, the usage of microemboli is generally preferred within medicine, life sciences and some engineering fields like food, environmental and chemical engineering.

As a general point of view, this interaction is also called embolism in some cases regarding the nature of microemboli and site where the interaction occurs. The following classes point out the collection of embolism in medical systems with respect to their corresponding origins across CPFO shunt;

1. **Thromboembolism**: A blood clot or thrombus which is formed in circulation due to a systemic, metabolic problem, an inflammation would try to cross CPFO or ASD. In some cases, this passage might not occur and trapped thromboembolus start to grow next to this aperture. A partial separation would eventually cause a paradoxical embolism due to the size of thromboembolus. In echocardiographic monitoring, this mobile mass would eventually be detected without difficulty due to its size and motility. Recently, several groups published detailed case reports regarding this rare condition [136, 137, 138, 139, 140].

   The activation of thromboxane prostanoid receptors in various capillary beds and the cooperation of Thromboxane A2 stimulates the generation of the platelet

masses and the future thrombosis [141]. In these cases, aspirin, warfarin anticoagulation technique, thromboxane prostanoid antagonists, preventive pharmacologic procedures are considered to reduce this risk which would cooperate with a silent CPFO [142]. However, these preventive techniques would not treat ASD nor CPFO. Furthermore, the study of Mas et al. [143] stated that the risk of stroke or transient ischemic attack would be as high as 19.2 % even if an aspirin prevention was applied at 4 years. It would be infered that these preventive procedures would not be advantageous in high risk groups.

2. **Cholesterol embolism**: Cholesterol embolism is generally characterized as an atherosclerotic plaque which arises inside a vessel and is also called as atheromatous. This type is well known and related to cerebral embolism. However, a direct relationship with CPFO has not been fully understood yet. Obviously, cholesterol emboli might occlude several cerebral arteries. Few studies would be related as an indirect correlation with CPFO-chlesterol embolism. [144, 145, 146].

3. **Fat embolism**: Bone fracture and collection of fat droplets are considered as main causes of fat embolism. Unlike cholesterol embolism, fat embolism is much more related with CPFO aperture. Bone fractures especially tibial and femoral fractures in elder people are found as the potential source of fat embolism. The case studies of Pell et al. [147, 148] and Etchells et al. [149] emphasized this relationship of fat mass and CPFO after fracture. Unknown sources of paradoxical embolism [150], respiratory failure and sudden death would also be related with this type of CPFO-embolism relationship.

4. **Cancer embolism**: Cancer embolism is considered as a mass of cancerogenic structures-plaque that leaves the tumour source and starts to travel into the circulation. It would be remarked that this type of embolism is less studied than other types regarding the number of published articles. Although its relationship with CPFO is not so clear, it is remarkable to see that cancer embolism would cause stroke due to rare invasion in pulmonary vein [151]. Lung, pancreatic and hepatic cancers are mostly related as sites which would cause cancer embolism with or without operation or resection [152, 153]. CPFO would be a potential

source for arterial tumor embolism, primary tumor of the aorta and direct tumor invasion of the aorta [151].

5. **Septic embolism**: Septic embolism is categorized as a pus enriched by dead or living bacteria which leaves an inflammation site (sepsis) and travels in the circulation. Its correlation with CPFO was shown in several publications [154, 155, 156, 157].

6. **Air embolism**: Air embolism is the main objective in this study. It is also called gas embolism. Microemboli in this thesis will mainly signify air embolism. This type of embolus is eventually studied by different groups with respect to diseases, physiological systems, origins and main pathways. Unlike the number of publications, the mystery of microemboli formation is still a hot topic for several research projects due to the variation between subject, environment and tasks.

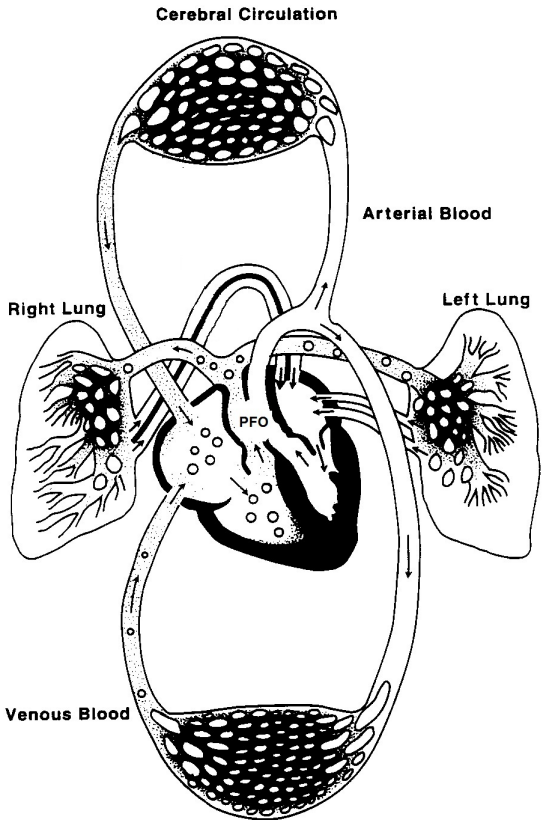

Figure 3.1 Intravascular venous microemboli circulation and CPFO shunt [7].

Microemboli in CPFO and DCS would be considered as a form of air embolism and is classified into two different categories; intravascular and extravascular. These categories are considered as principal sources of microemboli formation in the body even if exact origins are not yet revealed but estimated with physiological models and experiences. Intravascular form of microemboli is categorized as *arterial*, *venous* and *capillary* whereas extravascular form is classified as *intracellular*, *interstitial* and *lymphatic*.

Arterial gas embolism is briefly defined when the gas enters the vascular system beyond the pulmonary filter (i.e, at the point of the pulmonary veins, left heart or systemic arteries). On the other hand venous gas embolism is identified when the gas enters the vascular system before the pulmonary filter [158].

Microemboli formation along arterial circulation is not a commonly encountered case due to its physical properties. Inert gas tensions along arterial pathway are generally in equilibrium with alveolar gas, so arterial blood is not supersaturated with inert gas [7]. At the same time the hydraulic pressure in the heart prevents any microemboli generation.

On the other hand, venous circulation would be considered as a suspicous site for the significant numbers of microemboli. However, a direct relationship between bubble generation and venous blood might not be possible. No bubble formation occurs in an extracted blood filled *venae cavae* when a decompression procedure is applied [159]. Therefore, a realistic way to see the microemboli generation would be a better comprehension of capillary beds and extravascular tissues.

The physical properties of the surrounding environment determine the shape, morphology and behavior of this encapsulation. At the same time, they affect the consequences such as the vascular obstruction and the formation of gas-blood interface. As the embolus behaves as an uncommon object within the blood stream; platelets, leukocytes, fibrinogen and thrombin get close to the embolus [158]. This interaction might increase the forces of adhesion between the embolus and the vascular wall and

resist further embolus migration. Consequently, a damage in the vascular wall may occur and cause an oedema in the tissue.

The air embolism depends mainly on the solubility of the gas in the blood. CO_2, O_2, Air, NO_2, N_2O, He and Ar are the most encountered gases with a decreasing order. Other factors would be cited as the embolus volume, the rate of injection and the hemodynamic effects for the air embolism [158].

Vukovic et al. [160] recalled that microemboli detection would be assessed within several applications. Carotid artery stenosis, aortic arch plaques, atrial fibrillation, myocardial infarction, prosthetic heart valves, patent foramen ovale, valvular stenosis, during invasive procedures (angiography, percutaneous transluminal angioplasty), surgery (carotid, cardiopulmonary bypass, orthopedic), and in certain systemic diseases are the main areas where microemboli survey plays an important role to prevent injuries especially ischemic stroke.

Air embolism complications related to CPFO would be severe during a neurosurgery in the sitting position. Fathi et al. [135] who conducted a systematic survey within the databases Medline, Embase, and Cochrane Controlled Trial Register noticed that the overall rate of venous air embolism during neurosurgery in sitting position was 39% for posterior fossa surgery and 12% for cervical surgery. Therefore, a detailed screening for CPFO before a neurosurgery and its closure in cases in the sitting position is highly recommended.

Moreover, the relationship between CPFO and air embolism could be apparent during and sometimes after these following cases [109]; Extracranial carotid artery stenosis [161], intracranial carotid artery and middle cerebral artery stenosis, aneurysmal subarachnoid hemorrhage, carotid or vertebral artery dissection, mechanical heart valves, heart valve bioprosthesis, bacterial endocarditis, Behcet's disease [162, 163], Antiphospholipid syndrome [164, 165], Eisenmenger's syndrome [166, 167].

4. METHODOLOGY

As a brief introduction to pattern theory, Grenander [168] summarizes his ideas as; *In pattern synthesis one proceeds from low to high levels in the system. Pattern analysis represents the inverse process: starting from a high pattern level one tries to analyze the pattern object into lower level objects.* In this research, the starting point was to develop an automatic method to analyze spatio-temporal echocardiographic frames for CPFO which are interpreted manually depending on the visual experience of cardiologist. Briefly, our thesis which is directly related to echocardiographic images would be considered in a similar fashion of Grenander [168]; bubble synthesis for simulation and atria segmentation for bubble detection.

As CPFO is monitored with contrast material, detection, counting and grading of microemboli are highly subjective and people are mostly focused on the total number of bubbles which we call *Qualitative Analysis*. On the other hand, microemboli size, morphology, possible pathways, future behaviour in circulation would be so crucial when they are in cardiopulmonary system. Even some difficulties arise due to echocardiographic restrictions, most of the information would be retrieved from spatio-temporal (therefore 3D) echocardiographic frames with appropriate approaches. This point of view is called as *Quantitative Analysis*. Allen [169] characterizes the quantitative analysis of particles within six levels and emphasizes the automatic feature analysis by counting the shape, the size and other selected parameters of the particle which is a bubble in our study. As more specific informations would be generated regarding CPFO grade, microemboli size and morphology using this approach, this point of view would be more advantageous than giving only the chart of total bubble number in *Qualitative Analysis*. This specification is summarized briefly in Figure 4.1.

Detection results in Figure 4.2 illustrates the difference between two approaches. Qualitative approach determines the central part of candidate bubbles and returns total bubble number in a frame whereas Quantitative approach would return morphological

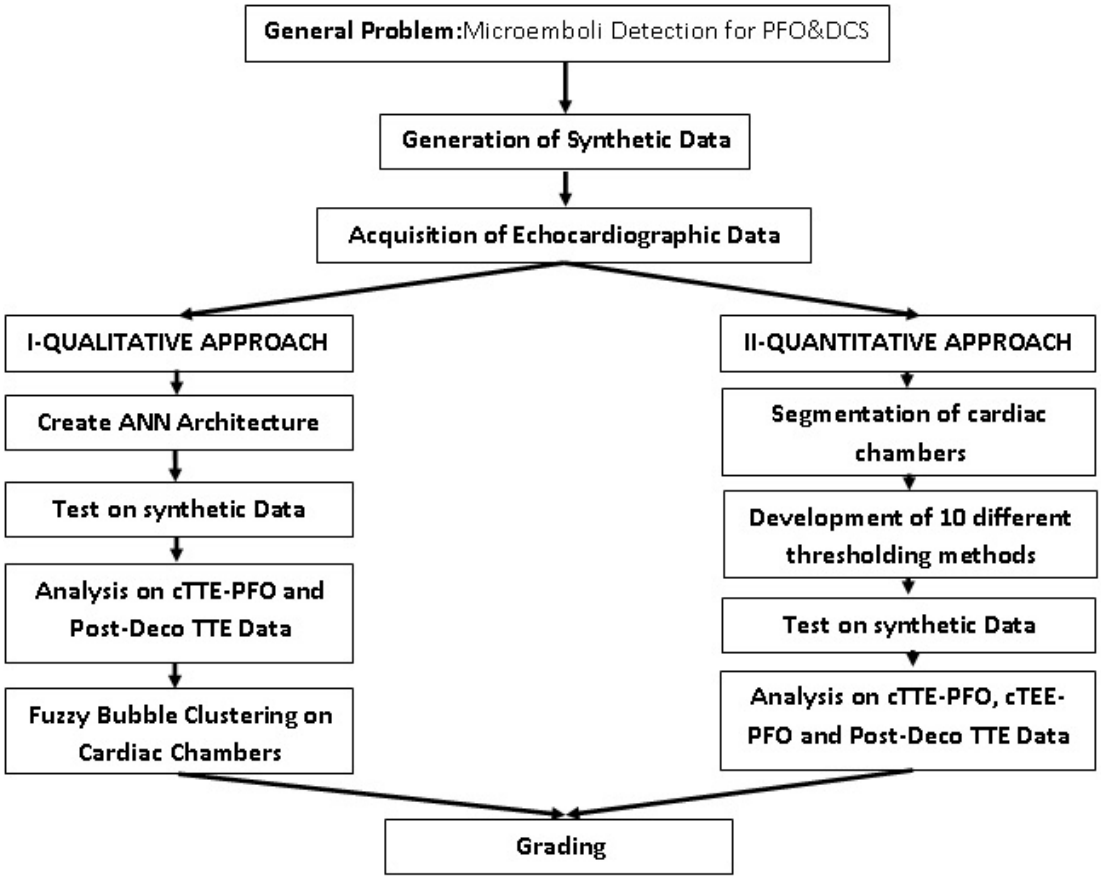

Figure 4.1 General view of the analysis flowchart.

aspects of a single microemboli in the frame such as; total area, centroid, convex hull, axis lengths, orientation, perimeter, bounding box.

First of all, a benchmarking with simulation data is always a good approach to test current and prospective methods. Before monitoring of the real microemboli which would cross CPFO aperture, synthetic bubbles were firstly created by mathematical models. Then, two different modalities of echocardiography; contrast TTE and contrast TEE were used to collect CPFO data with **contrast microemboli**. At the same time, cTTE was used to collect post decompression data with **intravascular microemboli**. Furthermore, all approaches were set to analyze those synthetic and real data. Finally, the findings were graded with conventional criterion [55].

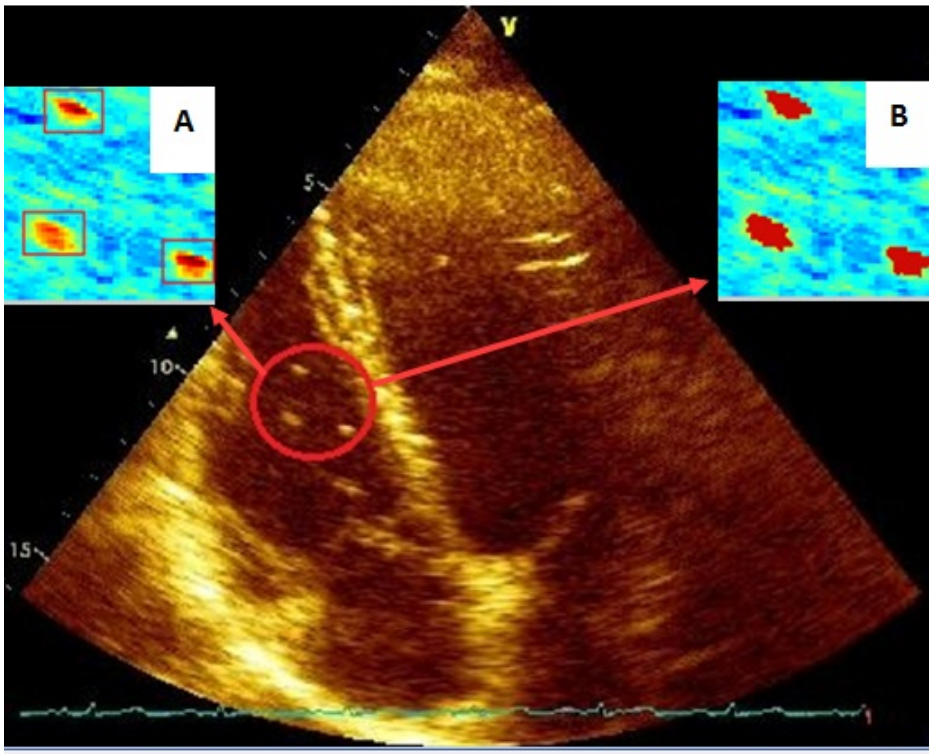

Figure 4.2 Detected microemboli with two different approaches in a post decompression TTE record; A-Qualitative B-Quanitative.

4.1 Generation of Simulation Data

In order to evaluate the performance of all methods which are taken into account, a simulation is always crucial to see the success rate of existent and proposed routines regarding their statistical errors and their aimed accuracy.

In general, realistic bubble models, imaging procedures, monitoring tools are mostly introduced by research groups in fluid dynamics, metallurgy, material science and mechanical engineering. This challenging domain is not yet fully simulated in human body and especially in pulmonary circulatory system due to the imaging restrictions such as; noise, resolution, chaotic dynamics, vortex formation and non-Newtonian properties.

In order to create a simulation environment, it was indispensable to see the morphology of a bubble in In echocardiographic records, bubbles are travelling dynamically and same bubbles generally might be seen in two previous or posterior frames if there

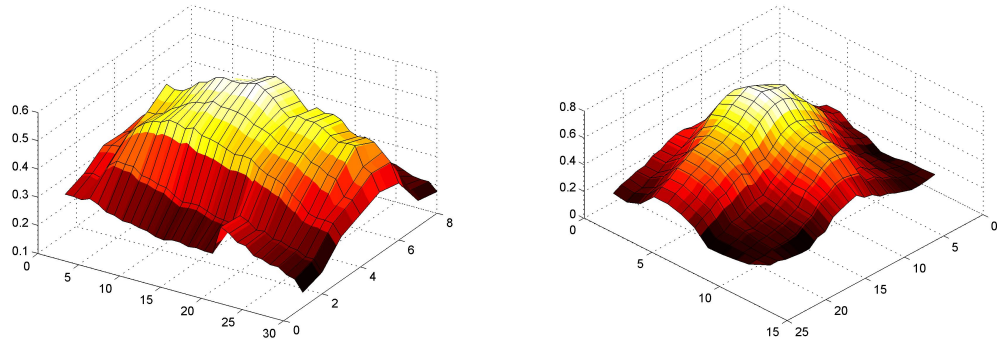

Figure 4.3 Real microemboli images acquired with cTTE.

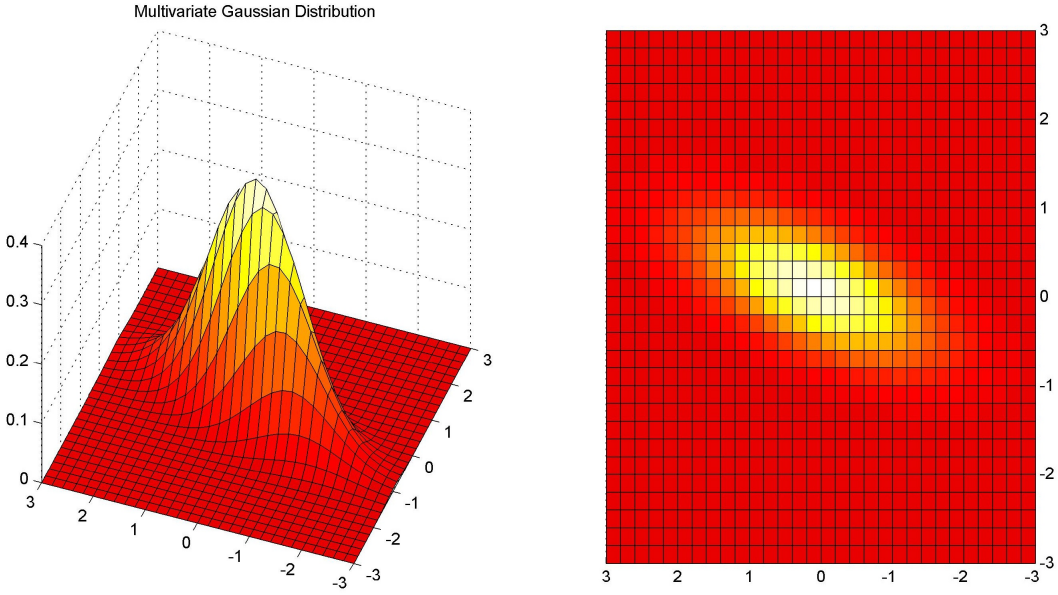

Figure 4.4 Development of a synthetic bubble.

is not a massive opacification. This manual and visual tracking procedure is applied by clinicians to lower errors. In order to set the same echocardiographic environment and bubble behaviour, synthetic microemboli would be either placed in previous or next frames by translating, rotating or removing.

Secondly, total number of microemboli during spatio-temporal analysis alters the grading score of CPFO. As Germonpré et al. [55] criterion for bubble classification in congenital diseases is adopted in this study, two different data sets were generated. When the number of bubbles in examined area is more or less than 20, subjects are grouped as Type 1 and Type 2 CPFO, respectively. Furthermore, bubble overlapping

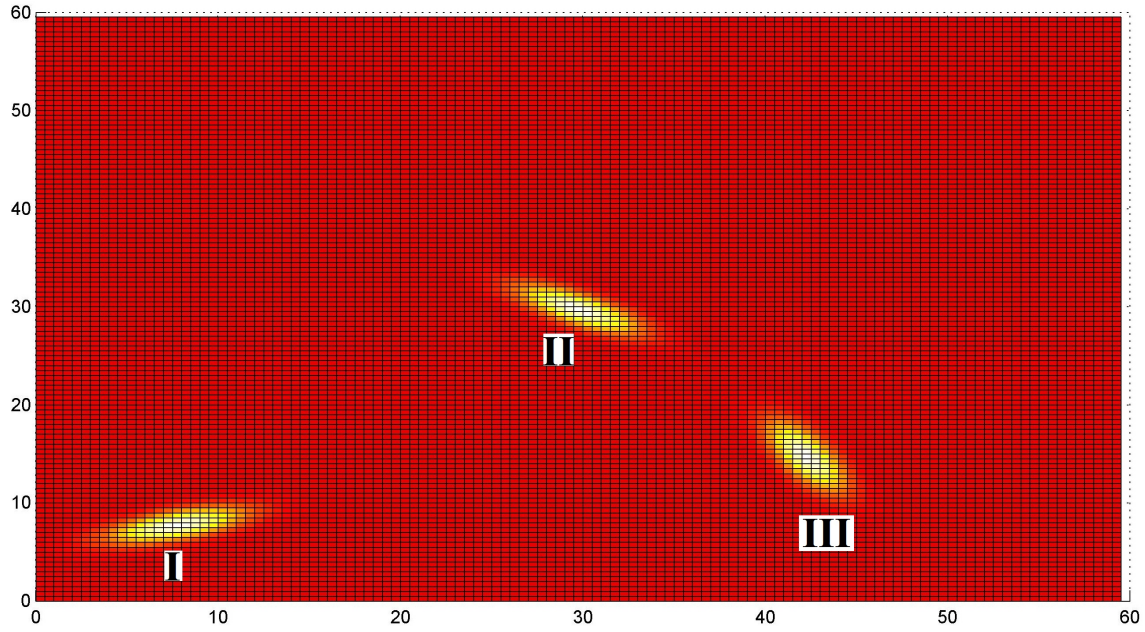

Figure 4.5 Representation of a random displacement of the same synthetic bubble in four consecutive frames onto one image; in the last frame bubble disapeared.

which is a common problem in bubble studies [8, 170] was simulated in another data set. These three different simulative data sets were pointed out as congenital atrial video records. Simulated frames were set as 160×120 pixels, the average size of segmented LA in real records. Each video stream was 1 sec long and 25 frames/sec (*fps*).

In order to generate artificial bubbles, we started to extract real bubbles from the Brightness (B) mode echocardiography frames represented in Figure 4.3. Furthermore, we built up a two dimensional theoretical model to represent bubbles as in the heart. A synthetic bubble was generated through multivariate gaussian model (Figure 4.4). As in Figure 4.5, the frames were in two dimensions where a bivariate normal distribution was used as follows;

$$P(x_1, x_2) = \frac{1}{2\pi\sigma_1\sigma_2\sqrt{1-p^2}} e^{[-\frac{\kappa}{2(1-p^2)}]} \tag{4.1}$$

where

$$\kappa = \frac{(x_1-\mu_1)^2}{\sigma_1^2} - \frac{2\rho(x_1-\mu_1)(x_2-\mu_2)}{\sigma_1\sigma_2} + \frac{(x_2-\mu_2)^2}{\sigma_2^2} \tag{4.2}$$

and

$$\rho = cor(x_1, x_2) = \frac{V_{12}}{\sigma_1 \sigma_2} \tag{4.3}$$

is the correlation of x_1 and x_2 and V_{12} is the covariance.

Bubbles on simulation datasets were placed randomly as in a realistic environment. Their contrasts were close to those of real emboli. In our study, a gradual speckle

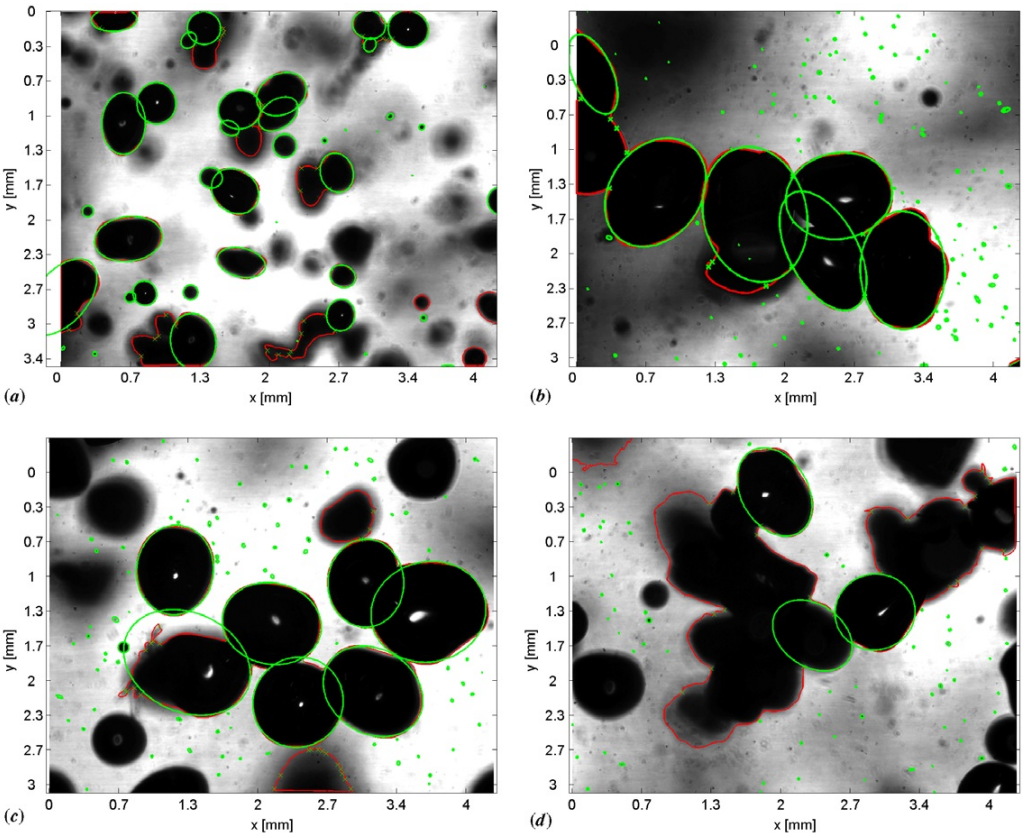

Figure 4.6 Detection of overlapped bubbles in the outlet pipe of a centrifugal pump [8].

noise is added onto simulation frames using the following criterion;

$$Frame_{noisy} = Frame_{original} + n * Frame_{original} \tag{4.4}$$

where n is uniformly distributed random noise with mean 0 and variance v. In order to compare the performance of methods, v was set between $0.05 - 1$.

Furthermore, the noise criterion Signal-to-Noise Ratio (SNR) defined in dB was calculated by using;

$$SNR = 20log_{10}(\frac{V_{original}}{V_{noisy}}) \tag{4.5}$$

where $V_{original}$ and V_{noisy} are the variances of the original frame and noisy frame, respectively.

We can summarize our simulation process as follows;

Generate blank frame (160×120)
for $n \geq 100000$ **do**
  if $CPFOType = 1$ **then**
    $1 \leq microembolinumber \leq 20$
    Generate randomly centroids of microemboli on the image
    Generate ellipses around centroids as isolines
    for $Outerellipse \geq ellipse_i \geq Centroid$ **do**
      Assign a decreasing brightness value
    end for
  end if
  if $CPFOType = 2$ **then**
    $20 \leq microembolinumber$
    Generate randomly centroids of microemboli on the image
    Generate ellipses around centroids as isolines
    for $Outerellipse \geq ellipse_i \geq Centroid$ **do**
      Assign a decreasing brightness value
      if $ellipse_i$ coincides with another $ellipse_j$ of $microemboli_j$ **then**
        Sum up the brightness in the intersection zone
      end if
    end for
  end if
end for

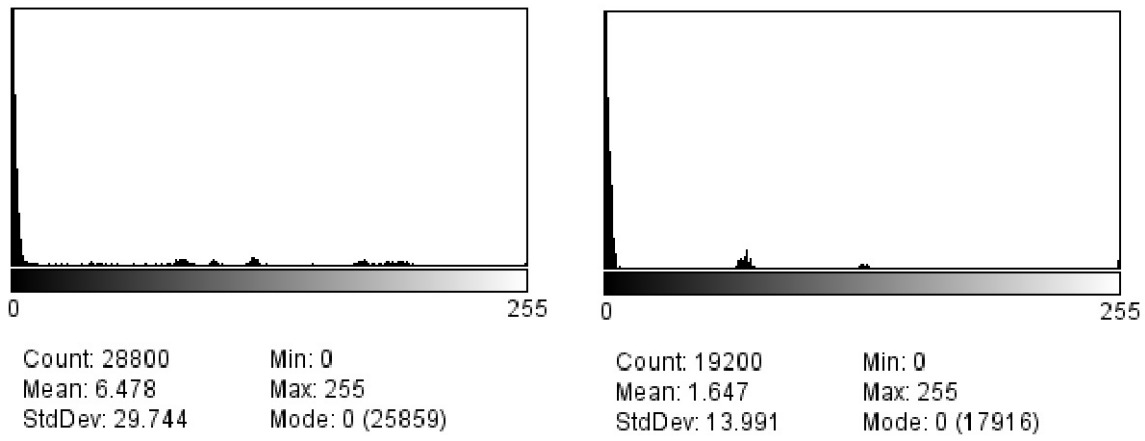

Figure 4.7 Simulation histograms; (Left) Histogram of a frame without noise (Right) Mean Histogram (100000 frames).

4.2 Echocardiographic Data Acquisition

We performed this analysis on twenty professional divers; 3 females - 17 males, ranging from 20 to 46 years old. The study protocol was approved in advance by Istanbul Memorial Hospital Ethics Committee. Each subject provided written informed consent before participating the experiment and to join the study.

CPFO detection and bubble visualization protocol described by Germonpré et al. [55] is utilized for each subject. All divers underwent cTTE and cTEE with agitated saline for contrast. All cTTE and cTEE video frames were recorded using either Sony DCR-PC101E PAL Mini DV camera connected to S-Video output of Ultrasound (3-8 Mhz, MicroMaxx, SonoSite Inc, WA) or directly through Ultrasound. For all subjects, acquisition is performed three times for each modality to ascertain CPFO grading by echocardiologists. Neverthless, in four subjects cTEE acquisition has been repeated four times due to subject motion, probe movement and the absence of a clear view of both right and left atrium. All participants underwent two-dimensional, M-mode and Doppler echocardiographic examination performed by an experienced research echocardiographer in accordance with the American Society of Echocardiography guidelines. cTTE images were acquired in the apical four chamber window. cTEE was performed with a 3-8 MHz multiplane transducer after an 6 hours of fasting, and topical anesthesia was achieved by lidocaine spray. TEE images were acquired in the bicaval plane

(110°). For cTEE, Ultrasound probe is positioned to view both right and left atrium. On the other hand all cardiac chambers are set for monitoring in cTTE.

Furthermore, we prepared the agitated saline contrast medium which is composed of 9.5 ml saline and 0.5 ml air echo contrast medium (ad hoc sonicated mixture of 0.5 ml air plus 9.5 ml plasma expander).

This solution is pushed back and forth 10 times in a double syringe system and injected through antebrachial vein. A massive opacification in the right atrium is visualized.

After at least two injections, each with a 1-min interval to clear the right atrium completely from the remaining bubbles, the patient was asked to perform a high-strain Valsalva maneuver, which was held for 10 sec before release. Agitated saline was injected during this maneuver. At the arrival of the first bubbles in the right atrium, the patient was instructed to release the strain.

Two different types of video acquisition were performed using a high (480x640 pixel) and a low (288x352 pixel) resolution video frames. In high resolution streams recorded by ultrasound, the video recording time was limited to 5 seconds. Total acquisition time in each modality was on the average 240 seconds for one individual. The video streams were captured in no compression-AVI movie format (28 frames/sec for low resolution and 32 frames/sec for high resolution). 240 x 28 = 6720 low resolution and 240 x 32 = 7680 high resolution frames were digitally stored in which 3.5 seconds 3.5 x 28 = 98 low resolution frames 3.5 x 28 = 112 high resolution frames were studied for each subject. We have chosen 3.5 seconds because the subjective method to grade the CPFO was based on the evaluation of three heart cycles following straining of the patient. In our analysis conventional three level bubble counting is adopted for both cTEE and cTTE. (Germonpré et al. [55]). All records were analyzed using Matlab R2010A, The MathWorks Inc, Massachusetts.

4.3 Qualitative Recognition

4.3.1 Gabor Wavelet

In this study, the Gabor kernel which is generalized by Daugman [171] was utilized to perform the Gabor Wavelet transformation. Gabor Transform is reliable approach in visual recognition systems [172]. Thus, a similar reasoning was was adapted for the bubbles (either contrast/synthetic or air/gas embolus) in cardiology which are mainly detected by the clinician depending on the perception based on the visual memory and experience.

$$\Psi_i(\overrightarrow{x}) = \frac{\left\|\overrightarrow{k_i}\right\|^2}{\sigma^2} e^{-\frac{\left\|\overrightarrow{k_i}\right\|^2 \left\|\overrightarrow{x}\right\|^2}{2\sigma^2}} [e^{i\overrightarrow{k_i}\overrightarrow{x}} - e^{-\frac{\sigma^2}{2}}] \tag{4.6}$$

Here each Ψ surface is identified with $\overrightarrow{k_i}$ vector. $\overrightarrow{k_i}$ vector which is engendered in a Gaussian function with standard deviation σ. The central frequency of ith is defined as;

$$\overrightarrow{k_i} = \begin{pmatrix} k_{ix} \\ k_{iy} \end{pmatrix} = \begin{pmatrix} k_v \cos(\theta_\mu) \\ k_v \sin(\theta_\mu) \end{pmatrix} \tag{4.7}$$

where;

$$k_v = 2^{\frac{2-v}{2}} \tag{4.8}$$

$$\theta_\mu = \mu \frac{\pi}{8} \tag{4.9}$$

The v and μ s express five spatial frequencies and eight orientations, respectively whose structure is represented in Figure 4.8.

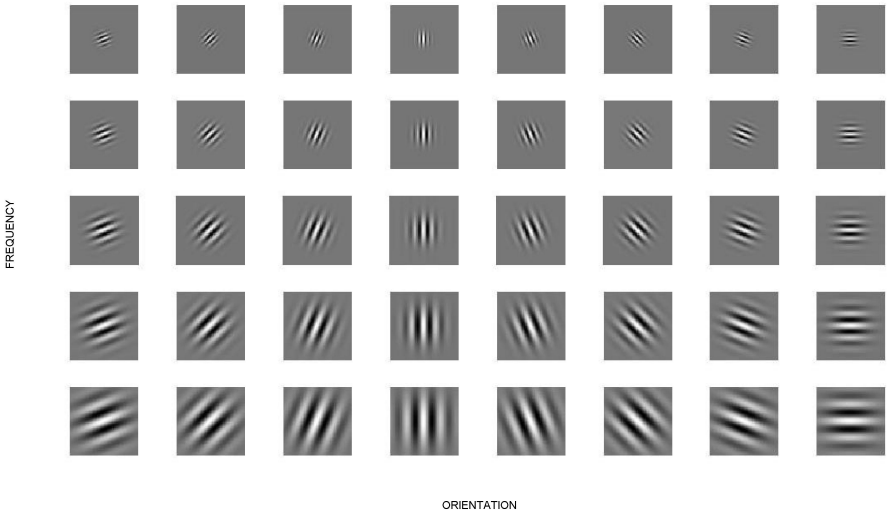

Figure 4.8 Gabor wavelet for microemboli detection.

4.3.2 Artificial Neural Networks

Our hierarchy in ANN is constructed as feed forward neural network which has three main layers. While hidden layer has 100 neurons, output layer has one output neuron. The initial weight vectors are defined using *Nguyen Widrow* method. Hyperbolic tangent function is utilized as transfer function during learning phase. This function is defined as follows;

$$\tanh(x) = \frac{e^{2x} - 1}{e^{2x} + 1} \tag{4.10}$$

Our network layer is trained with candidate bubbles whose contrast, shape and resolution are similar to those in considered records. 250 different candidate bubble examples are manually segmented from different videos apart from TTE records in this paper. Some examples from these bubbles are represented in Figure 5.3

All TTE frames within this study which may contain microemboli are firstly convolved with Gabor kernel function. Secondly, convolved patterns are transferred to ANN. Output layer expresses probable bubbles onto the result frame and gives their corresponding centroids.

4.3.3 Fuzzy Clustering

Fuzzy K-Means Clustering Algorithm is found as a suitable data classification routine in several domains. Detected bubbles would be considered as spatial points in heart which is briefly composed by four cardiac chambers. Even the initial means would affect the final results in noisy data sets. We hypothesize that there will be two clusters in our image and their spatial locations do not change drastically if any perturbation from patient or probe side does not occur.

We initialize our method by setting the two the initial guesses of cluster centroids. As we separate ventricles and atrium, we place two points on upper and lower parts. Our frame is formed by 640x480 pixels. Therefore, the cluster centre of ventricles and atria are set to 80x240 and 480x240 respectively. As this method iterates, in the next steps we repeat to assign each point in our data set according to its closest mean. The degree of membership is performed through Euclidean distance. Therefore, all points will be assigned to two groups; ventricles and atrium.

We can summarize our Fuzzy K-Means method as follows;

Initialize $mean_{ventricle}$ and $mean_{atrium}$
while *means* do not change **do**
  for $1 \leq m \leq max_{numberofpoint}$ **do**
    for $1 \leq n \leq 2$ **do**
      $1 \leq microembolinumber \leq 20$
      Calculate degree of membership:U(m,n) of point x_m in $Cluster_n$
    end for
  end for

for $1 \leq Cluster \leq 2$ **do**

Evaluate the fuzzy means with respect to new assigned points

end for

end while

4.4 Quantitative Recognition

In clinicial assessment of CPFO, total bubble number would be considered as sufficient to check if the shunt is active or not. This problem would be resolved via qualitative recognition. However, it is crucial to describe how the bubbles may behave during the activation of CPFO. All diseases related to CPFO are generally conducted with the interaction of bubbles and how they act within this process. They would separate or merge and enter to the circulation afterwards.

As the microemboli-CPFO interaction is described in Chapter III, a quantitative approach would be indispendable to reveal microemboli size and morphology when the embolism was related to CPFO. This approach could be interpreted via the quantifiers in Figure 4.9, their distribution with respect to cardiac chambers or the decaying curves. An automatic analysis becomes more important in cases where long lasting echocardiographic records are acquired. Therefore, the detection of bubbles and their significant quantifiers would help to define preventive techniques in microemboli generation.

In this thesis, the starting point of quantitative detection was based on low resolution analoguous video records through multiplane echocardiographic probe (HP Sonos 2500) in cTEE. A direct application of recognition procedures failed because of all possible microemboli in the frame. For this purpose a preprocessing step was designed. This processing step consists of prefiltering and segmentation.

As far as speckle noise might be existent on echocardiographic frames, direct application of segmentation procedures fails in low resolution noisy frames if a correct

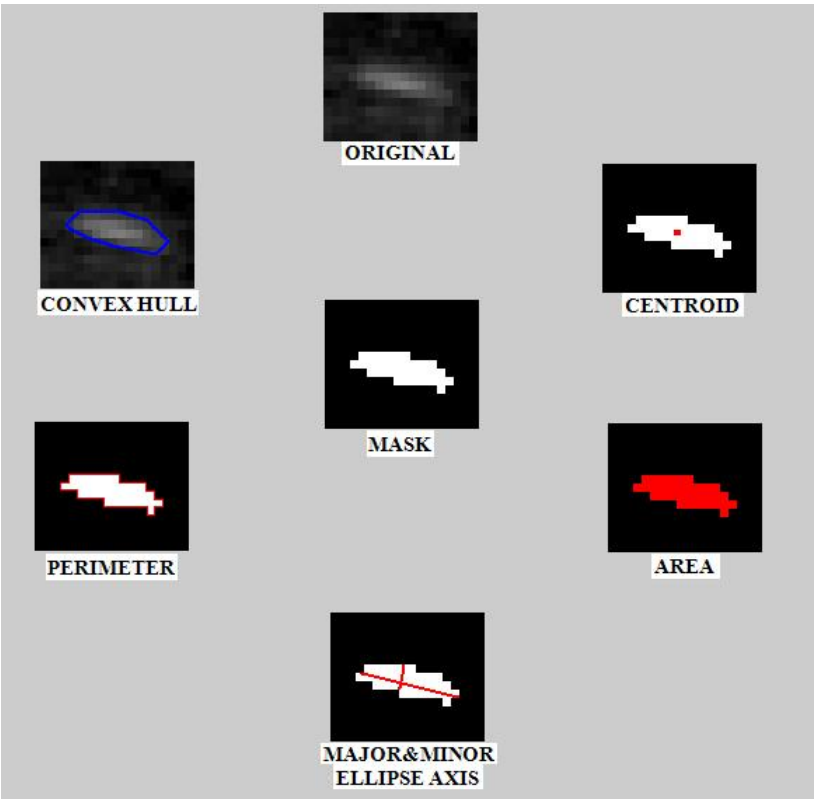

Figure 4.9 Morphologic informations of detected bubble called as microemboli quantifiers.

noise removal is not achieved. Some types of prefiltering methods give better results for speckle noise. Before the evaluation of segmentation, we tested the performance of 2D Median, 2D Wiener, Anisomorphic Filters and Wavelet Denoising methods. We remarked that this fundamental step in low resolution and noisy frames would be skipped in high resolution, good scaled frames After this prefiltering, frames were segmented to quantify cardiac chambers in which candidate microemboli would circulate. This segmentation step was achieved using Active Contours.

Furthermore, raw segmented cardiac frames were processed via thresholding algorithms in order to detect candidate microemboli. This step which is called pixel thresholding or blob detection in the literature of image processing. Nine existent methods and a new proposed method were tested on preprocessed frames. Three methods were found as accurate detection methods through their performance, high sensitivity and specificity. The outline of quantitative recognition is summarized in Figure 4.10.

4.4.1 Preprocessing

Median filter is a non linear technique which preserves edge formation on applied image areas and prevents edge blurring. It is a spatial technique which replaces central value through the neighborhood of applied kernel [173].

Similarly, Wiener filter is a stochastic process which eliminates additive noise by interpreting pixel statistics; local mean; μ and local variance; σ^2 surrounding each pixel. By calculating μ and σ^2 we created a Wiener process and estimated each pixel through η which represents noise variance [173].

Initially we started to perform our segmentation using active contours implemented via level set introduced by Caselles et al. [174]. In this approach contours are found using a Lagrangian formulation based on the evolution of parametrized curve. We remarked that the partial differential equation so called evolution is relatively slow in terms of computational time on video sequences. Therefore, we adopted a modified level set formulation and combined the methods of Chan et al. [175] and Vemuri et al. [176].

An initial level set by fronts Γ is expressed by a distance function; $\phi(x) = \pm d_\Gamma(x)$. It is represented in Figure 4.10 by red rectangle. A zero level set function is denoted;

$$\Gamma(t) = \{(x, y) : \phi(x) = 0\} \tag{4.11}$$

Given the front Γ, let $F(x)$ be the speed function in the direction of the normal of Γ and $x(t)$ be a point on Γ which evolves progressively then $\phi(x(t), t) \equiv 0$ for all t. When we differentiate this expression with respect to t;

$$\frac{\partial \phi}{\partial t} + \nabla \phi \frac{dx}{dt} = 0 \tag{4.12}$$

Level set function has both positive and negative terms including zeroes and is called

signed distance function

$$\frac{\partial \phi}{\partial t} = sign(\phi)(1 - |\nabla \phi|) \tag{4.13}$$

where

$$sign(x) = \begin{cases} -1 & \text{if } x < 0 \\ 0 & \text{if } x = 0 \\ 1 & \text{if } x > 0 \end{cases} \tag{4.14}$$

In Figure 4.10 white contours depicts the final form of ϕ therefore, the final level set function which is equal to Γ_{final}. We resolved this equation by interpreting without re-initialization. This approach is based on modified formulation that consists of two energy terms; internal and external. Internal term prevents the deviation of level set from signed distance function whereas external term conducts a motion on zero level set up to the final pattern features especially contours. A consequent evolution of this level set is a gradient flow and it minimizes the energy function as it is expressed in Equation 2.2 and 2.3. Segmentation results are validated by the experts and the performance of fixed ROI used by Eftedal et al. [5] is compared with the dynamic ROI.

4.4.2 Bubble Thresholding

In order to detect candidate bubbles on echocardiographic frames, different methods have to be proposed. Though correct recognition is important, it should be born in mind that computational time and synchronization is also crucial when long lasting decompression videos are analyzed with microemboli activities. Even if pseudo colors or RGB records would be used, cardiac patterns and especially heart chambers are composed of graylevel patterns.

Thresholding methods offer us not only the advantage to label spots but also returns a binarized form of images on which morphological properties would be calculated in a quantitative manner. Thresholding algorithms would create binary level

images using either RGB color or graylevel images and return candidate bubbles which are characterized as blobs.

In their review paper, Sezgin et al. [177, 178] studied in depth variant methods of multilevel thresholding on different images with diverse nature and noise level. They classified thresholding methods in six different categories;

- Histogram shape information
- Measurement of space clustering
- Histogram entropy information
- Image attribute information
- Spatial information
- Local chatacteristics

At the beginning of this thesis, we started to compute bubbles on low resolution images with the Otsu [179] method which is based on the measurement of space clustering. Afterwards, ten thresholding methods one of which is proposed in this thesis were tested individually in a simulation environment. In our simulation and real echogenic videos, bubbles would be easily identified through relevant threshols. However, it should be remarked that ultrasonic image processing is sensitive to inherent speckle noise. This type of interference would cause misleadings in detection, affect binary level image or introduce false alarms within the target blobs. In our study, these blobs correspond to candidate bubbles.

Pixel thresholding is applied both manually and with an automatic procedure whereas spatial thresholding is set as a predefined algorithm based on the long and short axial diameters of the elliptic bubble. Methods are implemented with automatic pixel thresholding through Otsu algorithm [179]. Spatial thresholding is predefined within 8-40 pixel distance (mean 16.75 pixels) for high resolution frames and 2-14 pixel

distance (mean 9.24 pixels) for low resolution frames. Ultrasonic studies [180, 181] indicate that bubbles are modeled as ellipse shape structures rather than star shape or lozenge. Therefore, we adopted similar structure for realistic bubble thresholding. Spatial thresholding based on ellipse axes filters out small or big structures besides the defined values. In our study we started to compare the effect of distances between 1-80 pixels through ellipse' axes. We remarked that bubbles on image frames are within 2-40 pixels.

In order to compare the performance between our study and recent work of Eftedal et al. [5], we performed a statistical analysis based on the evaluation of dynamic and static segmentation of LA. After the segmentation, eight proposed methods for bubble detection are applied for both approaches.

The static areas are not set randomly. For one video sequence, we extracted the minimal LA area in atrial diastole respecting the whole image frames. We started to set this area as a mask and detected bubbles within this limited zone for each frame on our recorded data.

All bubble detection results are validated by two specialists. The performance of methods 1 to 8 are evaluated by comparing missed and false detected bubbles with respect to the bubbles marked by the experts according to type 1 and type 2 errors [182]. For each sequence of recorded data, we determined true & false positives and true & false negatives in order to obtain Type 1 and Type 2 errors.

The sensitivity, specificity, positive & negative likelihood ratios and positive & negative predictive values are calculated using mean values through detected bubbles. In statistical analysis, the success of a method is measured through higher sensitivity and specificity rates. Furthermore, likelihood ratios greater than 1 depict that results are related with the findings. Generally a method is considered accurate for estimation by the terms of statistical inference, if its positive likelihood ratio is greater than 5 or its negative likelihood ratio is less than 0.2. In this case results can be interpreted as a priori information for medical data survey and pre-test probabilities. Positive

and negative predictive values guide us to determine the new probability or the new occurrence of the same procedure. Predictive value for both positive and negative tests represents the post-test probability related with CPFO. Therefore, a higher positive & negative predictive value would indicate that it is more probable with this approach to find bubbles on LA related with CPFO.

The performance of eight proposed methods is compared using recursive Bland-Altman plots through the difference of False Positives and False Negatives. For each step, mean and $\pm$ 1.96 times standard deviation bands are sketched. In each step we found the methods out of these bands or near to them in order to exclude these methods in the next step of Bland-Altman analysis.

4.4.3 Proposed Method

2D Cardiac images form a 3D data when frames are acquired sequentially through a device dependent fps. Therefore, all pixels in LA have a time series. It would be forseen that when a bubblewise structure will be present on this pixel, its graylevel will change suddenly. For this reason, a dynamic threshold which is applied to each pixel time series would reveal candidate bubbles as it is shown in Figure 5.25- 5.16.

This dynamic threshold is set using mean μ and σ of pixel time series. When a pixel value is above $\mu + 2\sigma$ this pixel is recognized as a bubble candidate in time. After this recognition procedure, all candidates of bubble are summed up on both corresponding frame and also as a novelty into one single frame. This single frame gathers all candidates and facilitates the recognition phase for a clinician.

After automatic recognition statistical analysis was performed to compare the real bubbles marked by the two clinicians and the computational recognition.

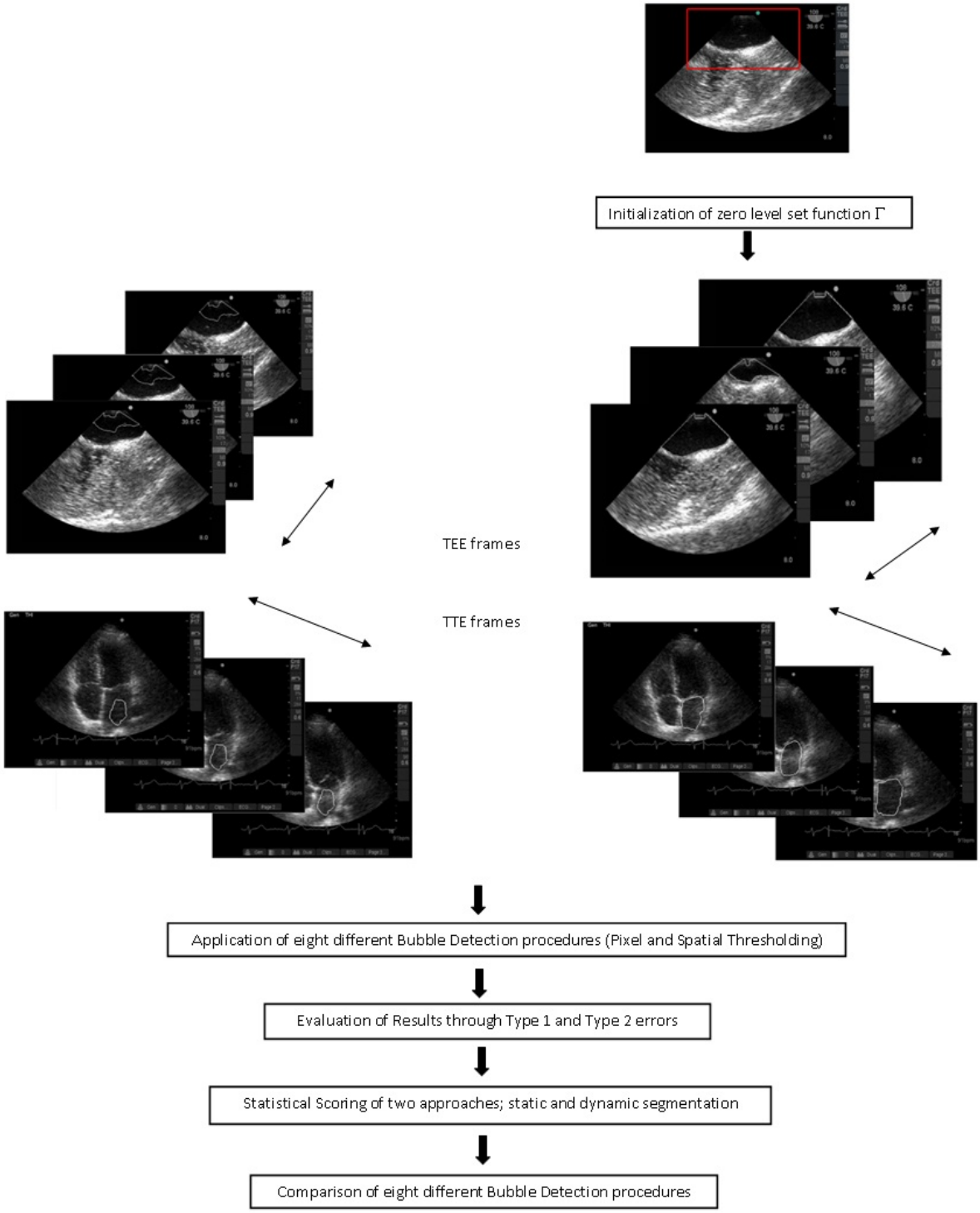

Figure 4.10 Flowchart of quantitative microemboli-CPFO recognition.

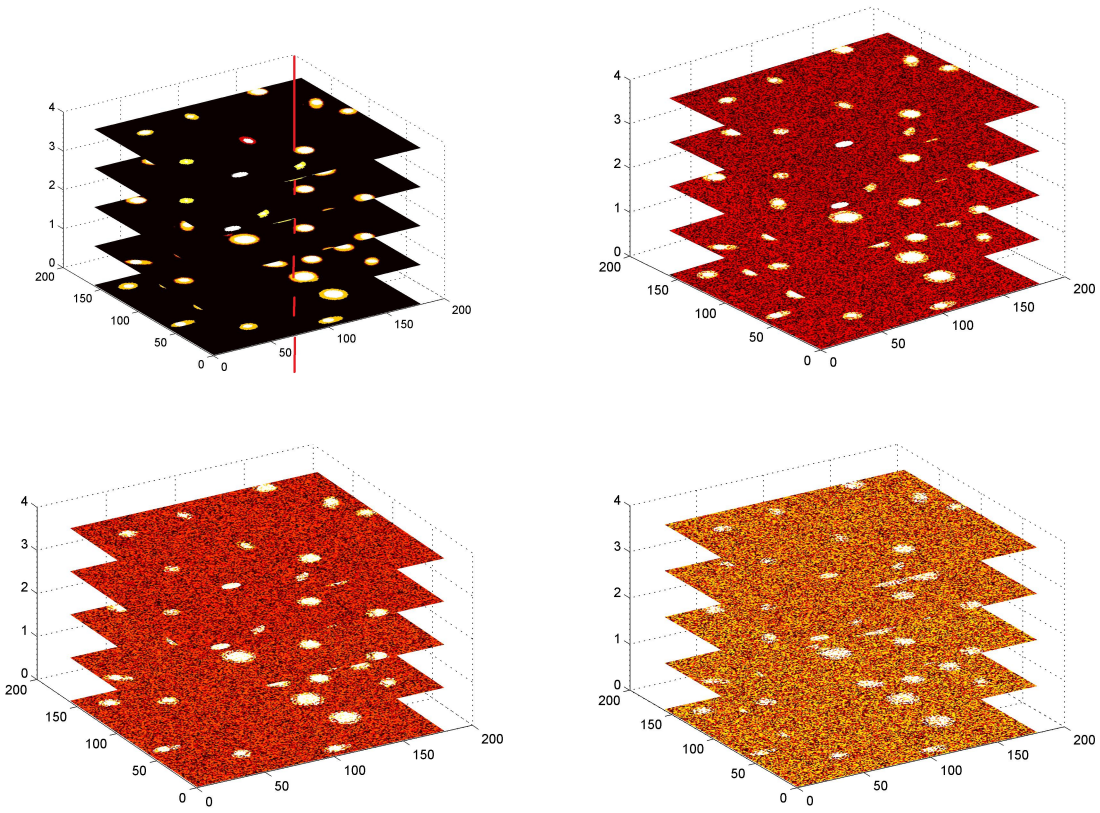

Figure 4.11 Comparison of three different methods in simulated LA.

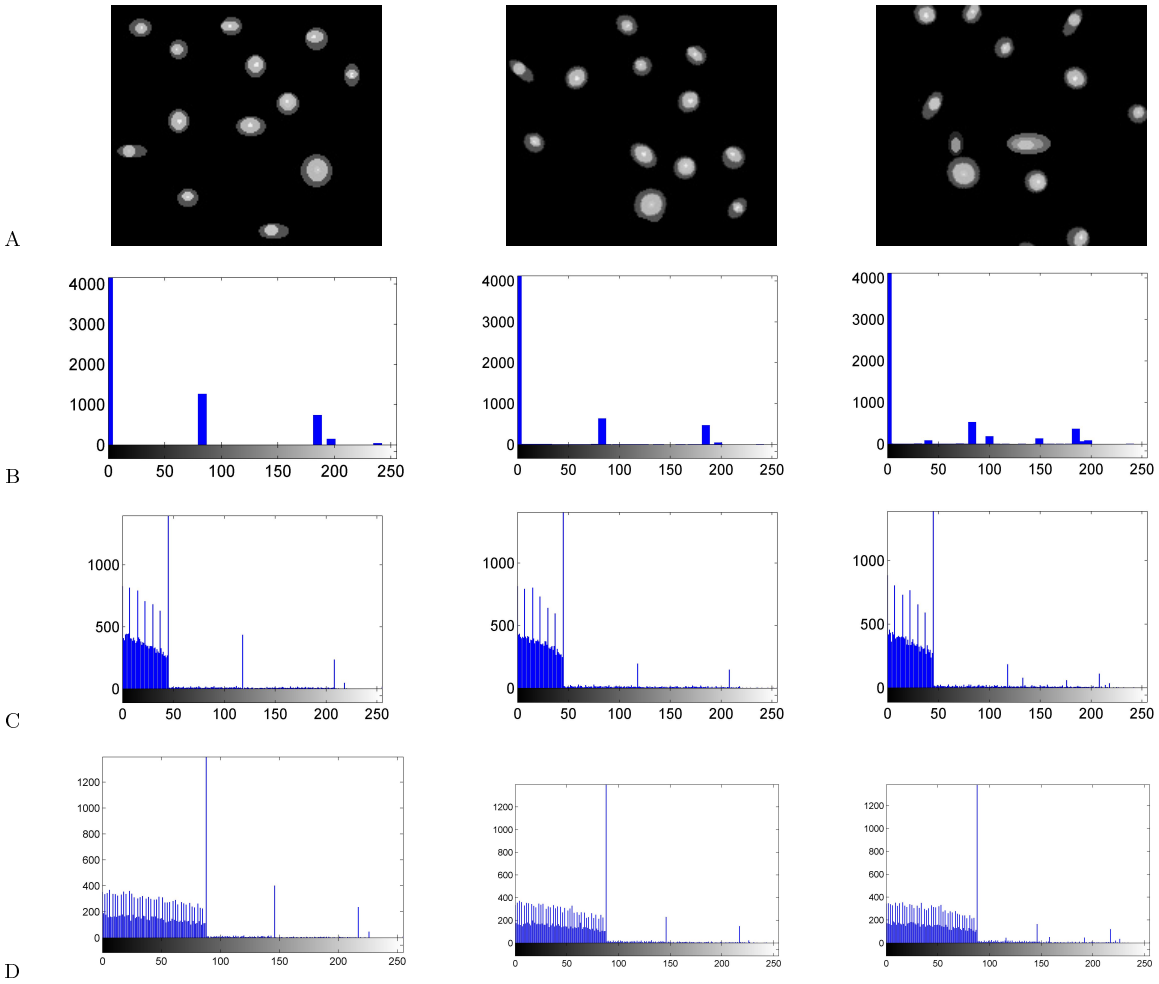

Figure 4.12 Generation of simulation bubbles and corresponding histograms; (A) Original frames, (B) Without noise, (C) Speckle noise variance; 0.2, (D) Speckle noise variance; 0.5

5. RESULTS

In this section, the generation of simulated microemboli were presented with different noise levels. CPFO analysis and microemboli detection were performed with two different approaches; Qualitative and Quantitative Recognition. Their corresponding results were presented with the respective methods. The detection results were interpreted statistically and bubble decay curves were described.

5.1 Generation of Simulation Data

5.2 Qualitative Assessment

In all subjects who were staying in post decompression interval, we found microemboli in four cardiac chambers. These detected bubbles in all frames were gathered into one spatial data set for each subject. Data sets were clustered via fuzzy k-means method within the corresponding chamber of the heart. Detection and classification results are given in Table 5.3 and 5.2.

In our initial phase of detection, we had the assumption of variant bubble morphologies for ANN training phase in Fig. 5.3. As it might be observed in Fig. 5.6, detected nine bubbles are located in different cardiac chambers. Their shapes and surfaces are not same but resemble to our assumption.

Even if all nine bubbles in Fig. 5.6 would be treated as true positives, manual double blind detection results revealed that bubbles fifth, eighth and nineth are false positives. We observe that our approach would recognize probable bubble spots through our training phase but it may not identify nor distinguish if a detected spot is a real bubble or not. In this case of Fig. 5.6 it might be remarked that false positives are located on endocardial boundary and valves. These structures are generally

continuously visualized without fragmentation. However, patient and/or probe movements may introduce convexities and discontinuities onto the apical or bicaval views of neighborhood tissues which would be detected as false bubbles.

We performed a comparison between double blind manual detection and ANN based detection in Table 5.3. Our bubble detection rates are between 82.7-94.3% (mean 89.63%). We observe that bubbles are mostly located on the right side which is meaningful physiologically. Bubbles in circulation would be filtered in lungs. Therefore, fewer bubbles are detected in left atria and ventricle.

In the initiation phase of fuzzy k-means method we set our spatial cluster means on upper and lower parts of image frame whose resolution is 640x480 pixels. These upper and lower parts correspond to ventricles and atrium as initial guess. When the spatial points were evaluated the centroids moved iteratively. We reached to the final locations of spatial distributions in 4-5 iterations. Two clusters are visualized in Fig. 5.7.

In order to evaluate the correctness of detection and the accuracy of bubble distribution, all records were analyzed double blinded. The green ellipse zones illustrate major false positive regions; endocardial boundary, valves and speckle shadows. In Table 5.3, we note that detection rates may differ due to visual speculation of human bubble detection in boundary zones, artifacts or within suboptimal frames. As it is shown in Table 5.2, the spatial classification into two clusters with fuzzy k-means were achieved for both detection approaches; manual and ANN based in order to compare how classification might be affected by computerized detection. In Table 5.2 we note that our classification rates are between 84.3-93.7% (mean 90.48%). We should note that classification rates through manual detection were 82.18-88.65% (mean 84.73%).

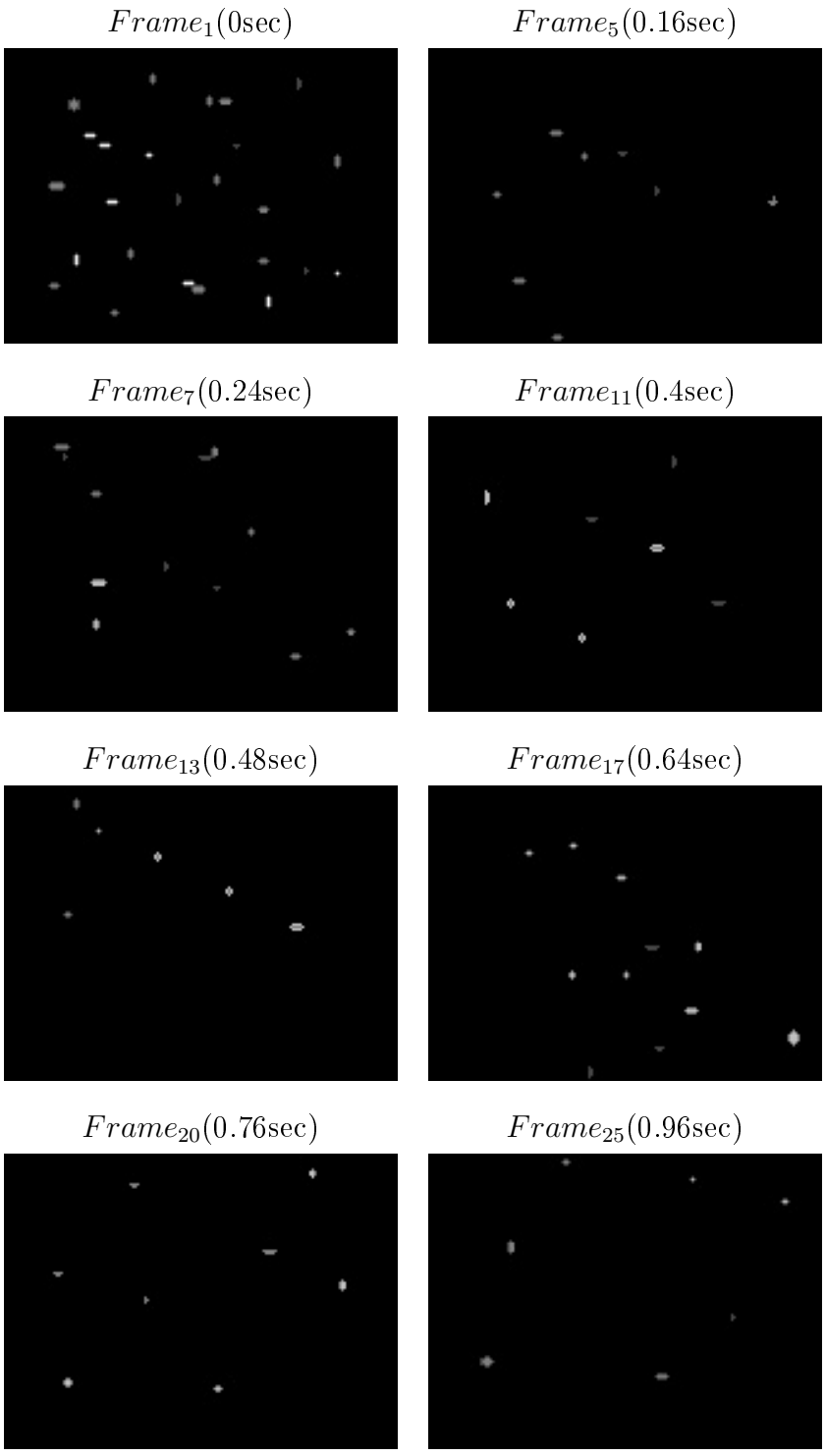

Figure 5.1 Generation of 1 sec (25fps) of Type-2 microemboli sequence.

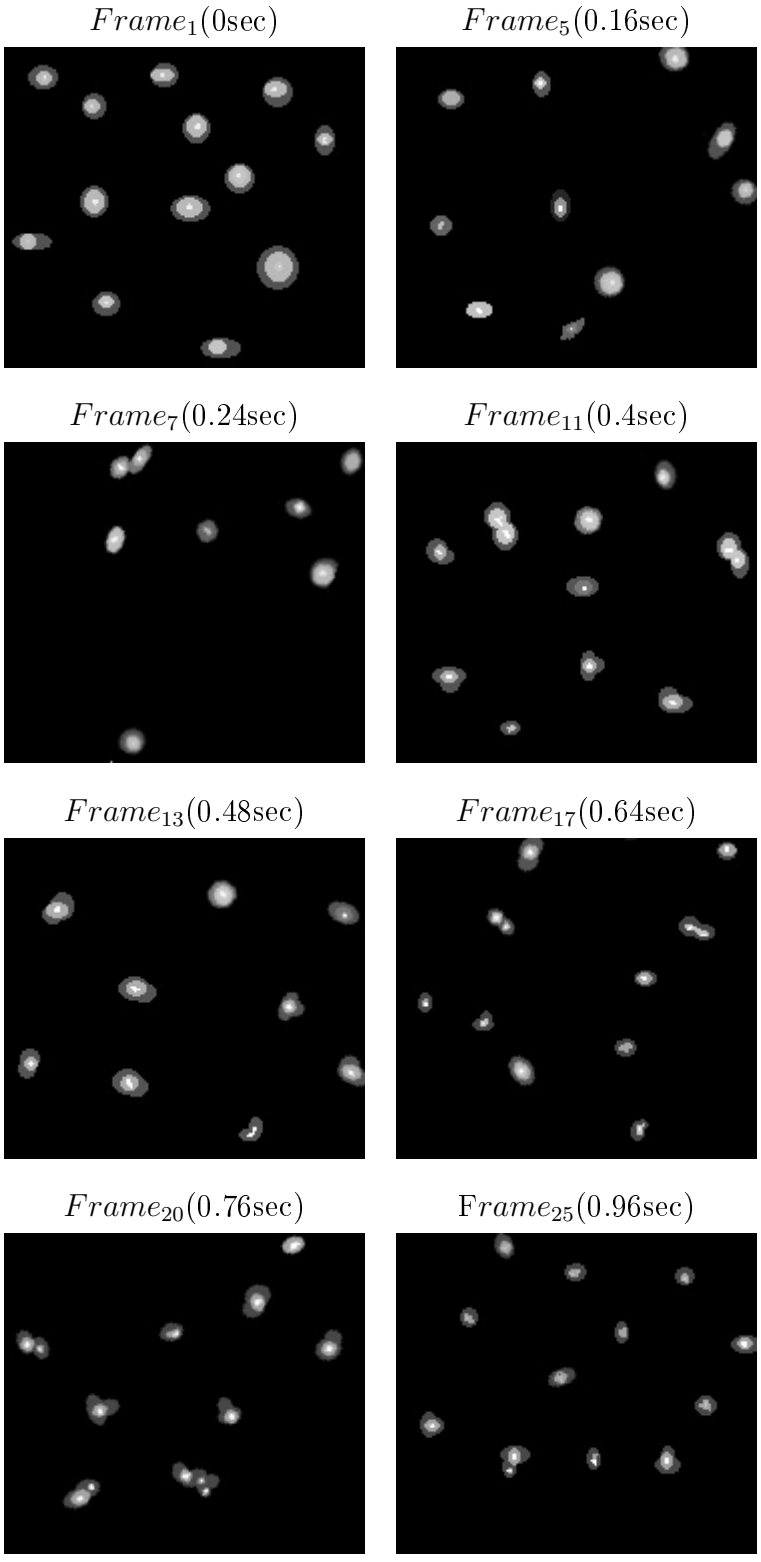

Figure 5.2 Generation of 1 sec (25fps) of overlapped microemboli sequence.

Figure 5.3 Example of bubbles for the training of ANN (left), their binary representations (right).

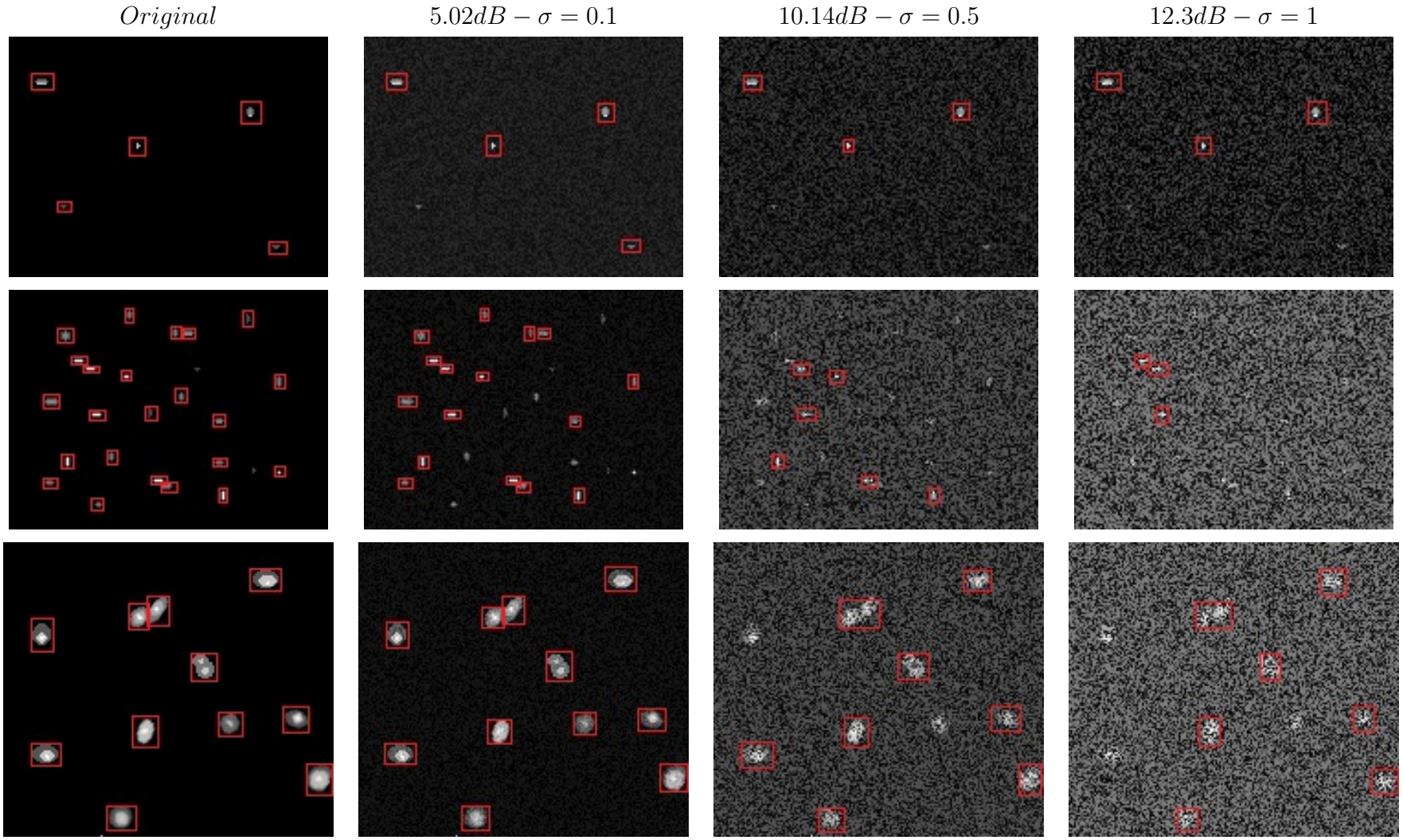

Figure 5.4 Generation 1 sec (25fps) overlapped microemboli sequence.

	Detected Bubbles			Detection Rate of ANN(%)	
	ANN	Clinician1	Clinician2	Through Clinician1	Through Clinician2
Subject #1	475	405	428	82.71	89.01
Subject #2	1396	1302	1287	92.78	91.53
Subject #3	864	818	800	94.37	92

Table 5.1
Evaluation of detection results.

	Ventricular		Atrial	
	Bubbles	Clustering Rate(%)	Bubbles	Clustering Rate(%)
Subject #1	288	87.65	187	89.23
Subject #2	915	84.32	481	91.85
Subject #3	587	92.19	277	93.76

Table 5.2
Evaluation of classification results.

5.3 Quantitative Assessment

In this thesis, the algorithms were tested for the detection of the simulation and the real echogenic bubbles. In both steps, our proposed method offered better accuracy and low I-II errors than the existent methods.

In the simulation phase ten methods including our method were tested on two different congenital forms through increasing noise levels. Simulation results were compared in Table 5.3 and Fig. 5.8- 5.9. Only three methods were satisfactory under high noise levels. Therefore, we selected them to compare their performance in real datasets.

In real echogenic forms, recognition algorithms offered reliable results as shown in Table 5.4. However, existent methods were sensitive to inherent noise and endo-

	Simulation1			Simulation2		
	Original	$\sigma = 0.07$	$\sigma = 0.5$	*Original*	$\sigma = 0.07$	$\sigma = 0.5$
Otsu[179]	100%	96.7%	6.4%	100%	97.3%	3.2%
Yen et al.[183]	100%	99.1%	97.5%	100%	98.4%	97.2%
Ramesh et al.[184]	98.7%	98.3%	96.7%	100%	99.1%	97.4%
Beghdadi et al.[9]	99.6%	5.2%	0%	100%	9.5%	0%
Proposed method	100%	98.8%	97.2%	100%	99.3%	98.1%

Table 5.3
Evaluation of detection results in simulated data.

	Video 1 Detection Ration	Video 2 Detection Ration	Mean Ratio
Ramesh et al.[184]	85.8%	87.1%	86.2%
Yen et al.[183]	87.6%	88.9%	88.3%
Proposed method	93.8%	96.5%	95.7%

Table 5.4
Evaluation of detection results in real cardiac videos.

cardial structures. It is noted in Fig. 5.16 that boundary structures could not be thresholded efficiently with Ramesh et al. [184] or Yen et al. [183]. Our proposed method detects bubbles with low Type I-II errors. It is also evident that bubble detection map which bring all recognized candidates into one frame is a novelty in this study. In Fig. 5.26, the visualization of all detected microemboli onto one single frame brings an ease of use for bubble movements.

Frame1

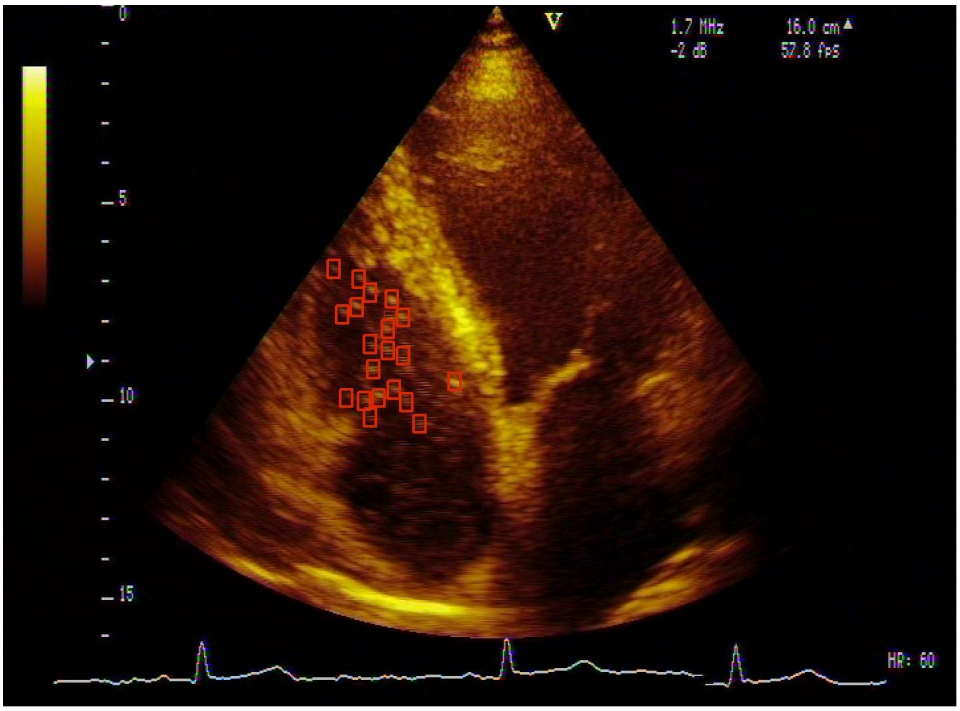

Frame12

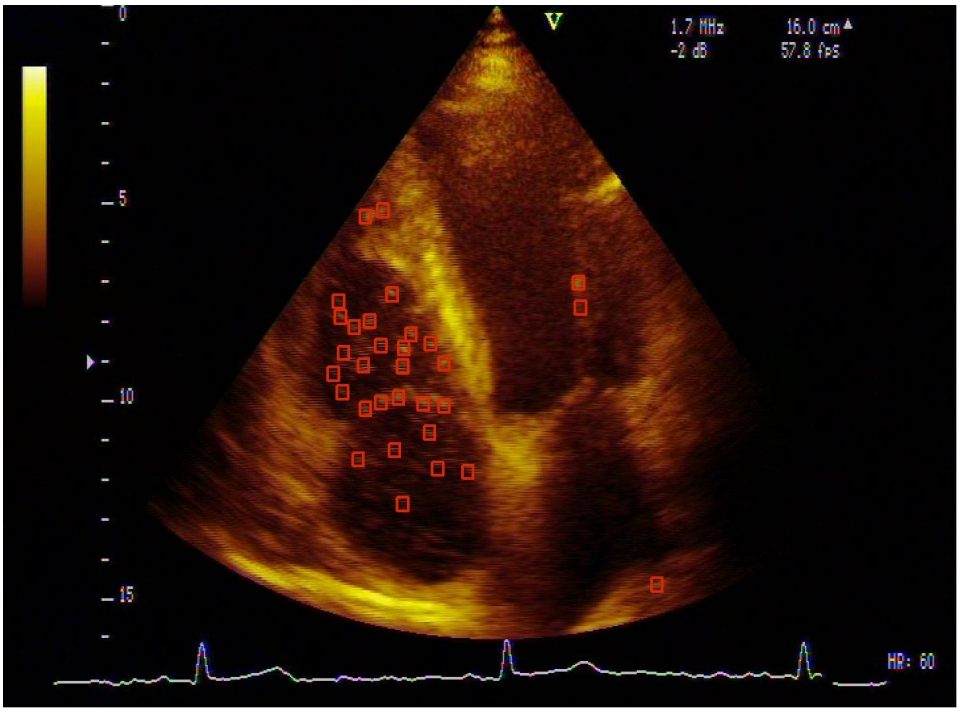

Figure 5.5 Detection 0.5 sec (25fps) overlapped microemboli sequence.

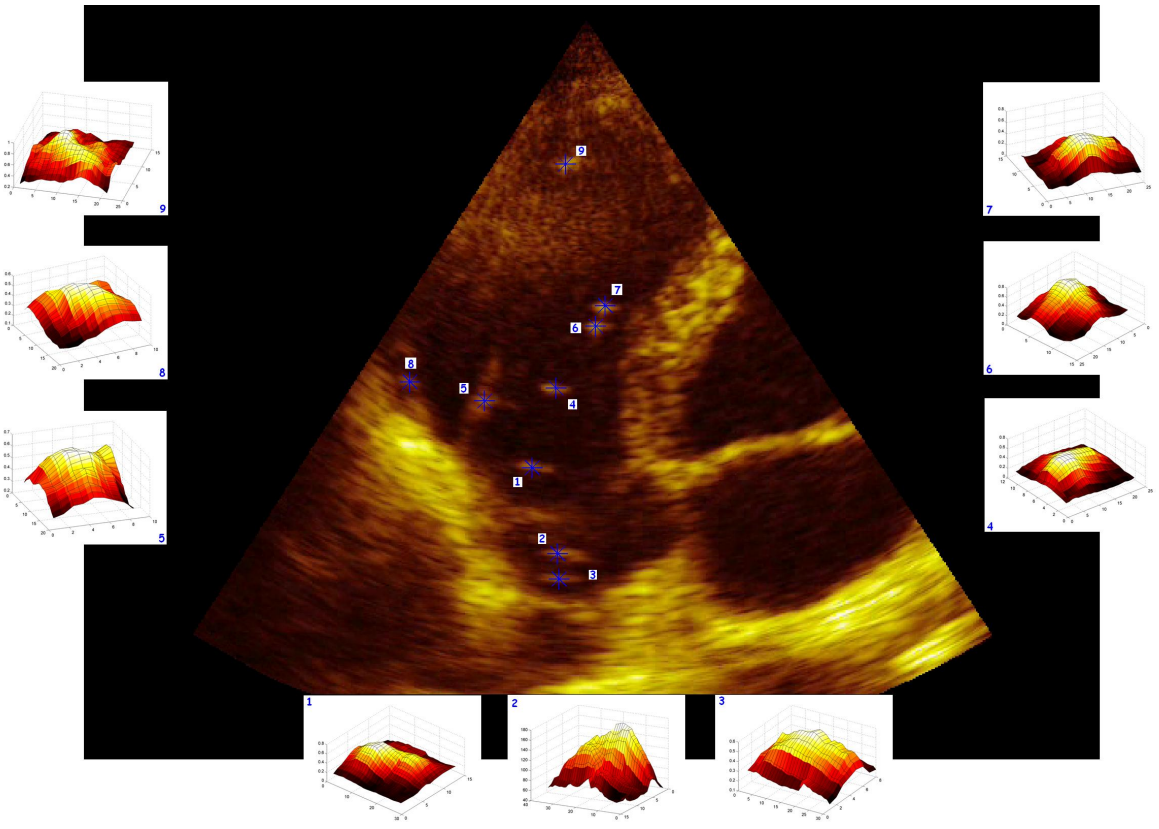

Figure 5.6 Detection results and Bubble Surfaces.

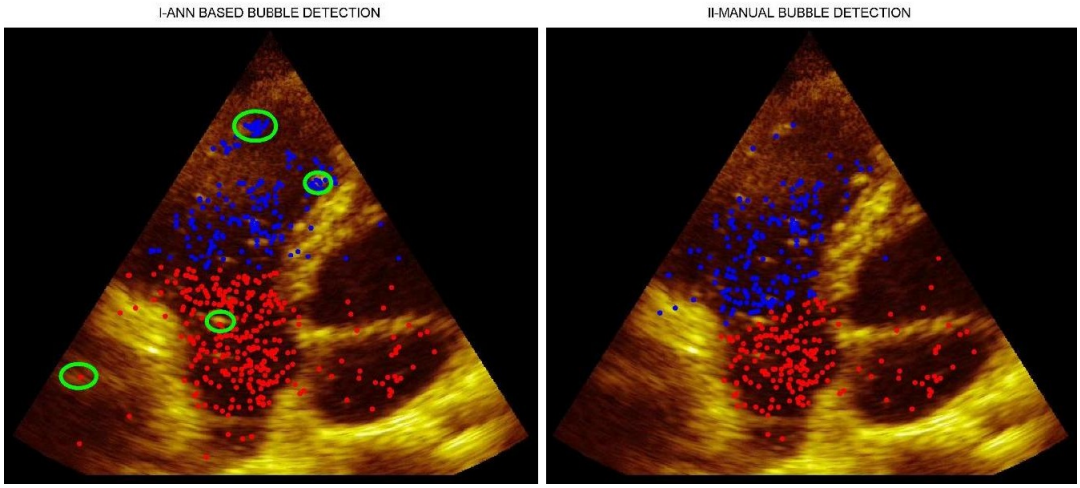

Figure 5.7 Comparison of the classification between ANN based (Left) and Manual (Right) Detection; red and blue dots represent the microemboli in atria and ventricles respectively. Green ellipses indicate the false alarms.

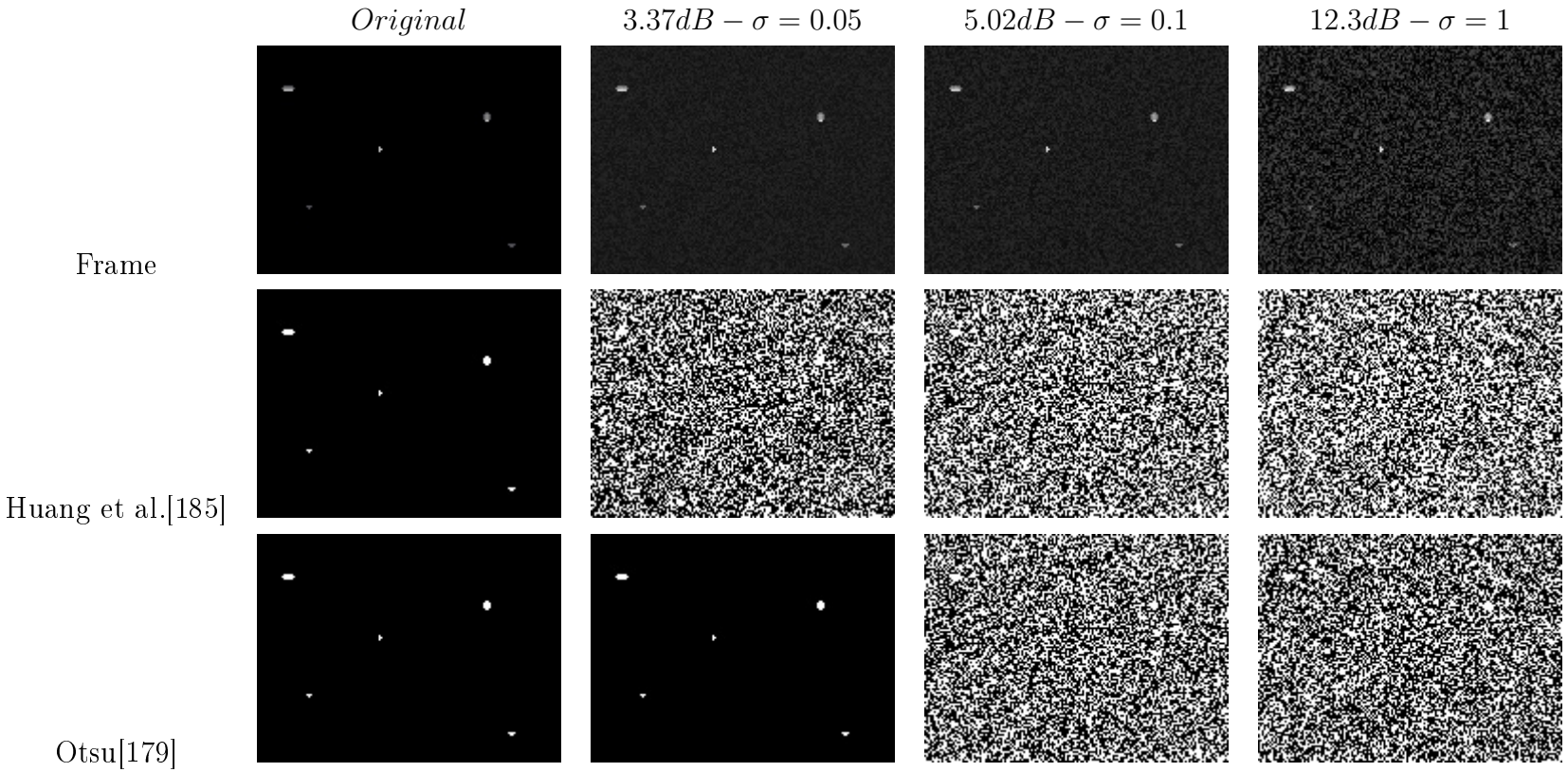

Figure 5.8 Comparison of bubble detection for ten different methods.

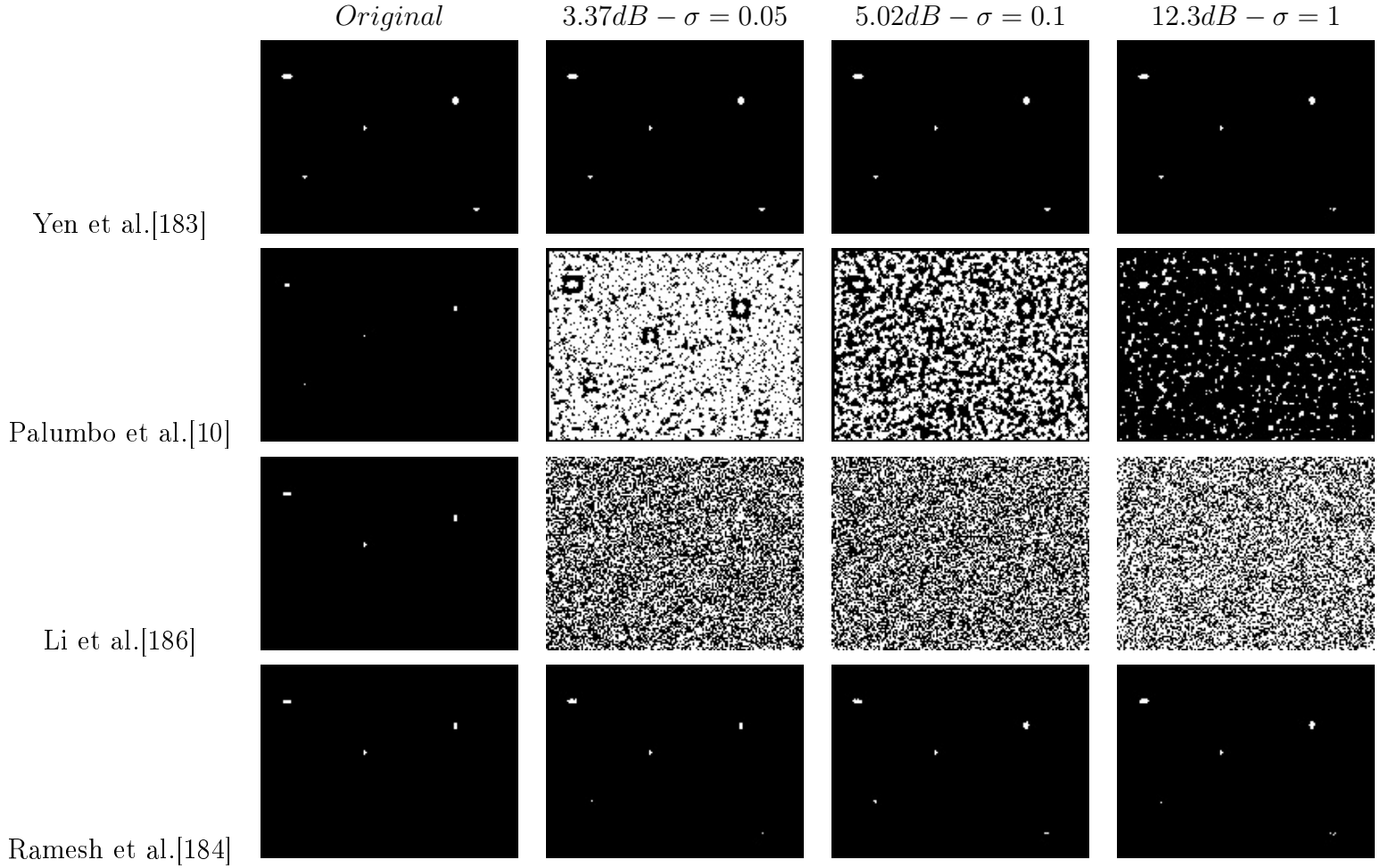

Figure 5.9 Comparison of bubble detection for ten different methods (continued).

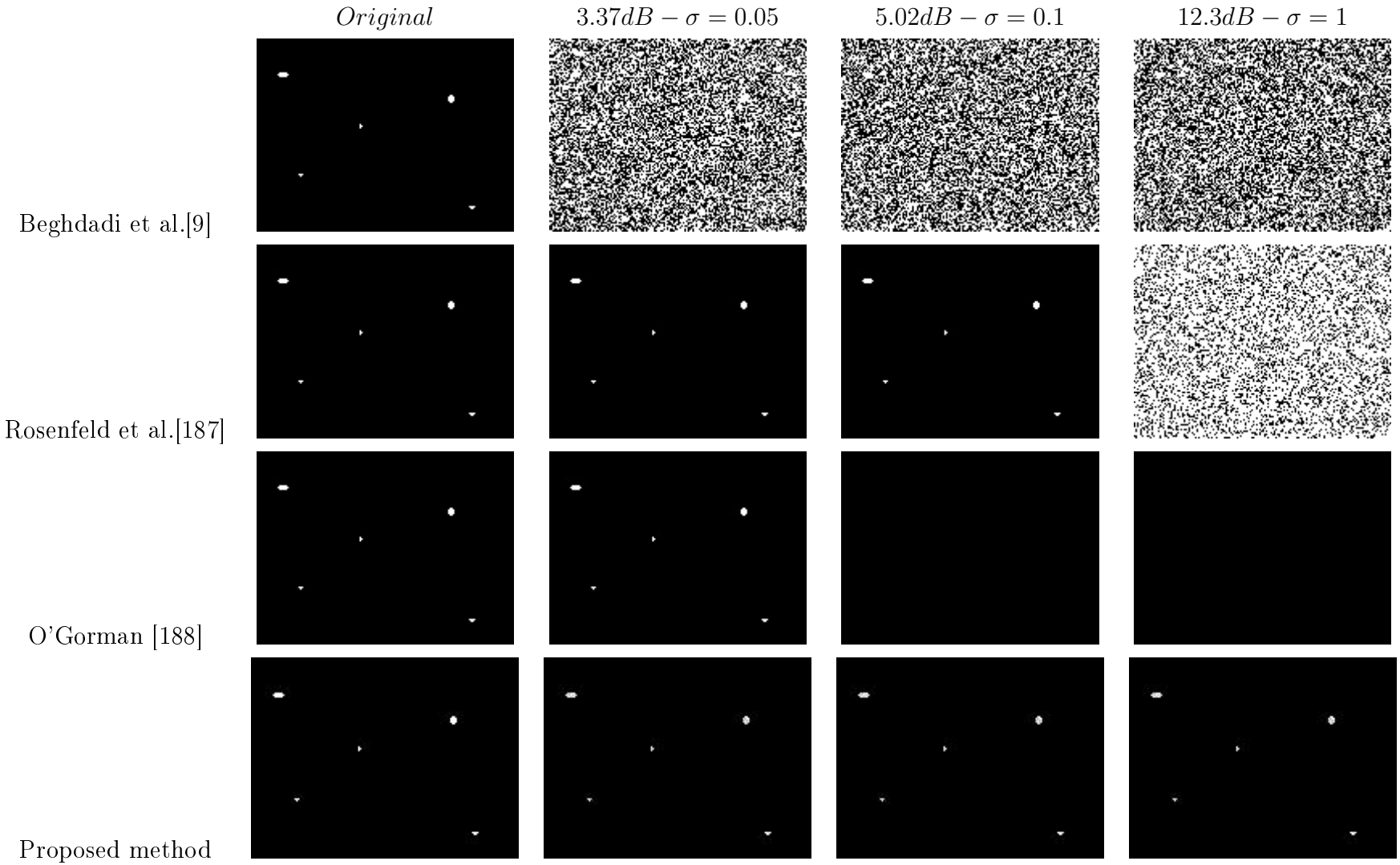

Figure 5.10 Comparison of bubble detection for ten different methods (continued).

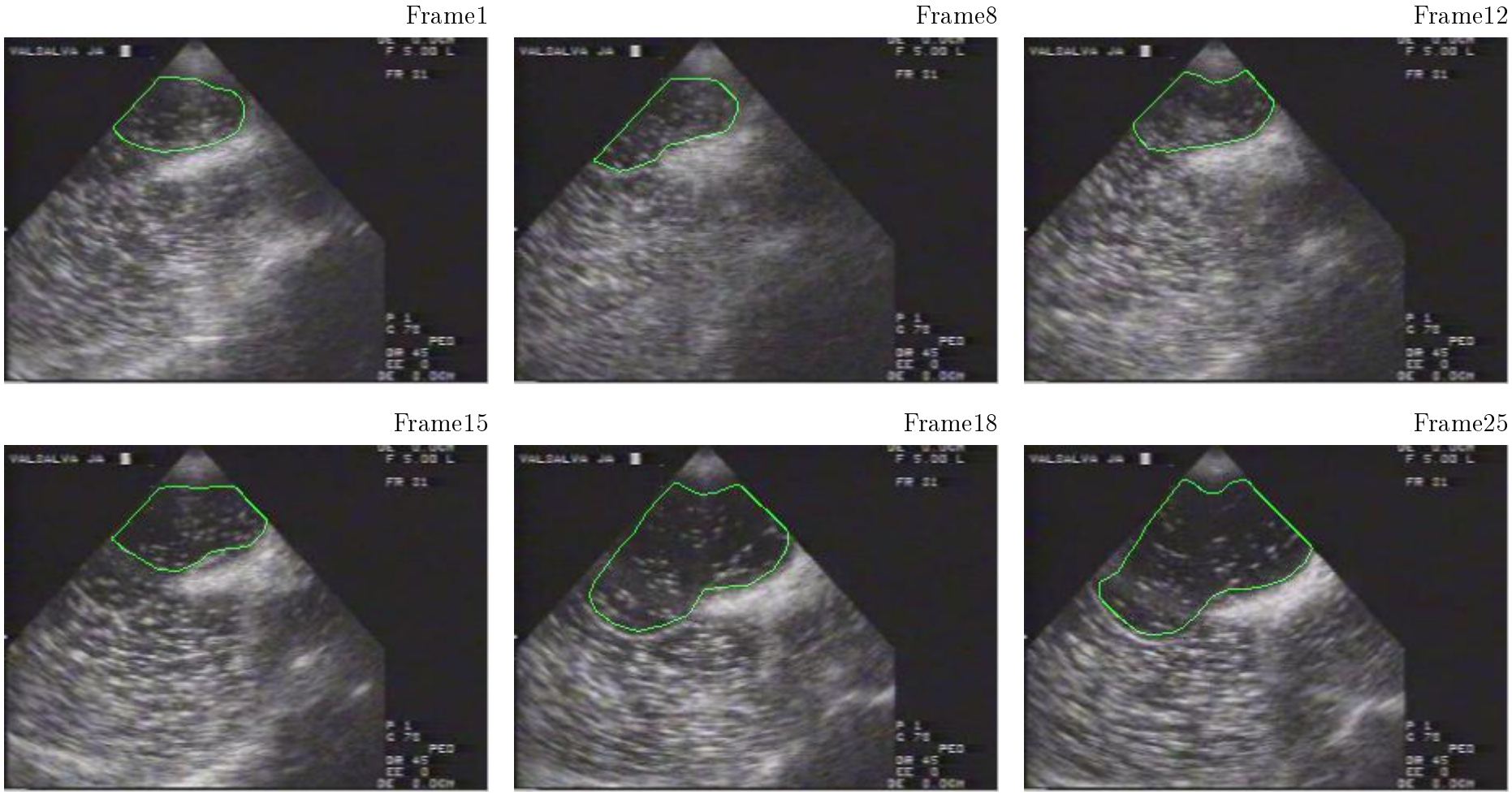

Figure 5.11 Contour Detecttion for 1 sec (25fps) of cTEE acquisition.

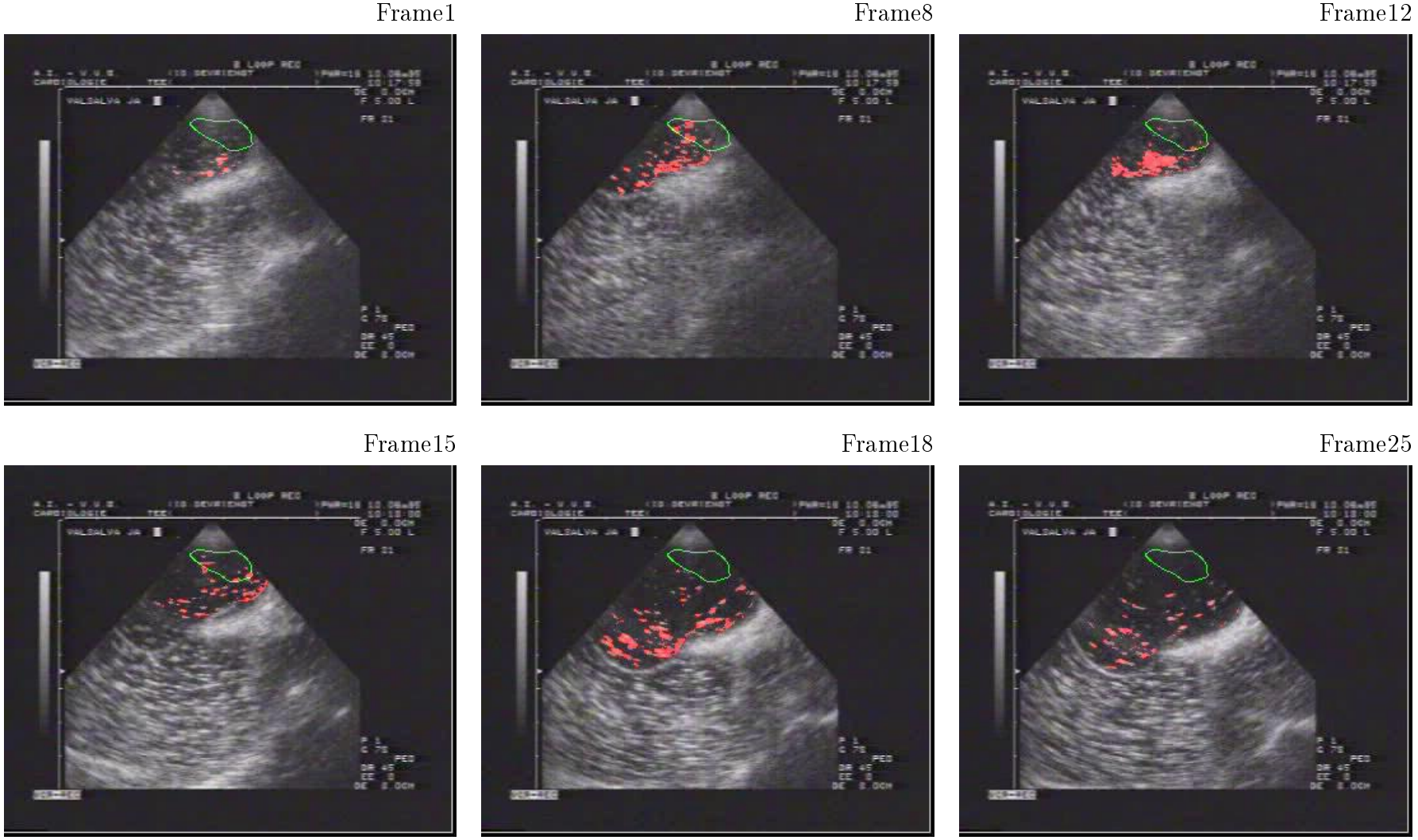

Figure 5.12 Effect of static ROI (green, smallest LA in systole) for bubble detection (red, detected regions).

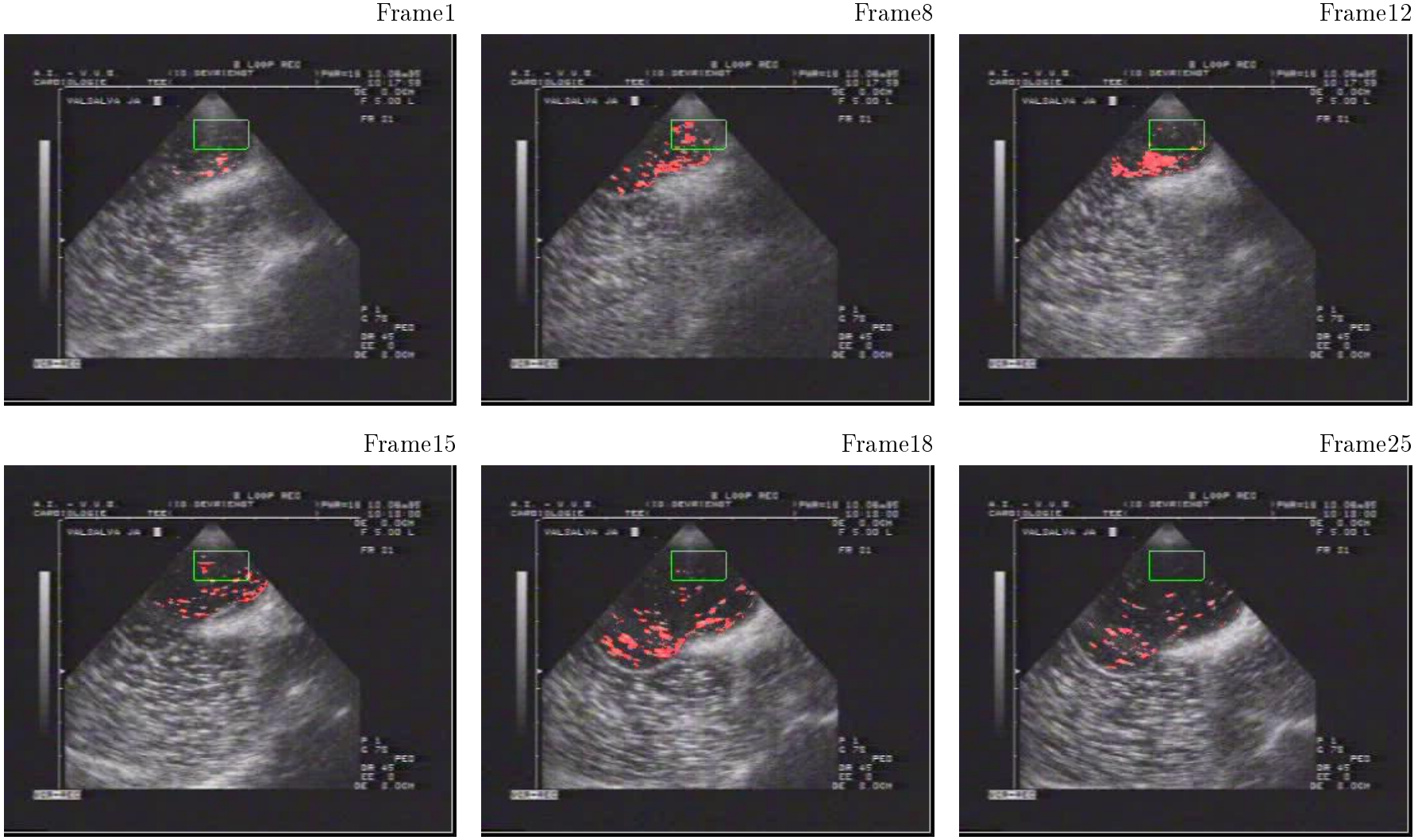

Figure 5.13 Effect of freehand tracing of ROI (green, rectangle) for bubble detection (red, detected regions).

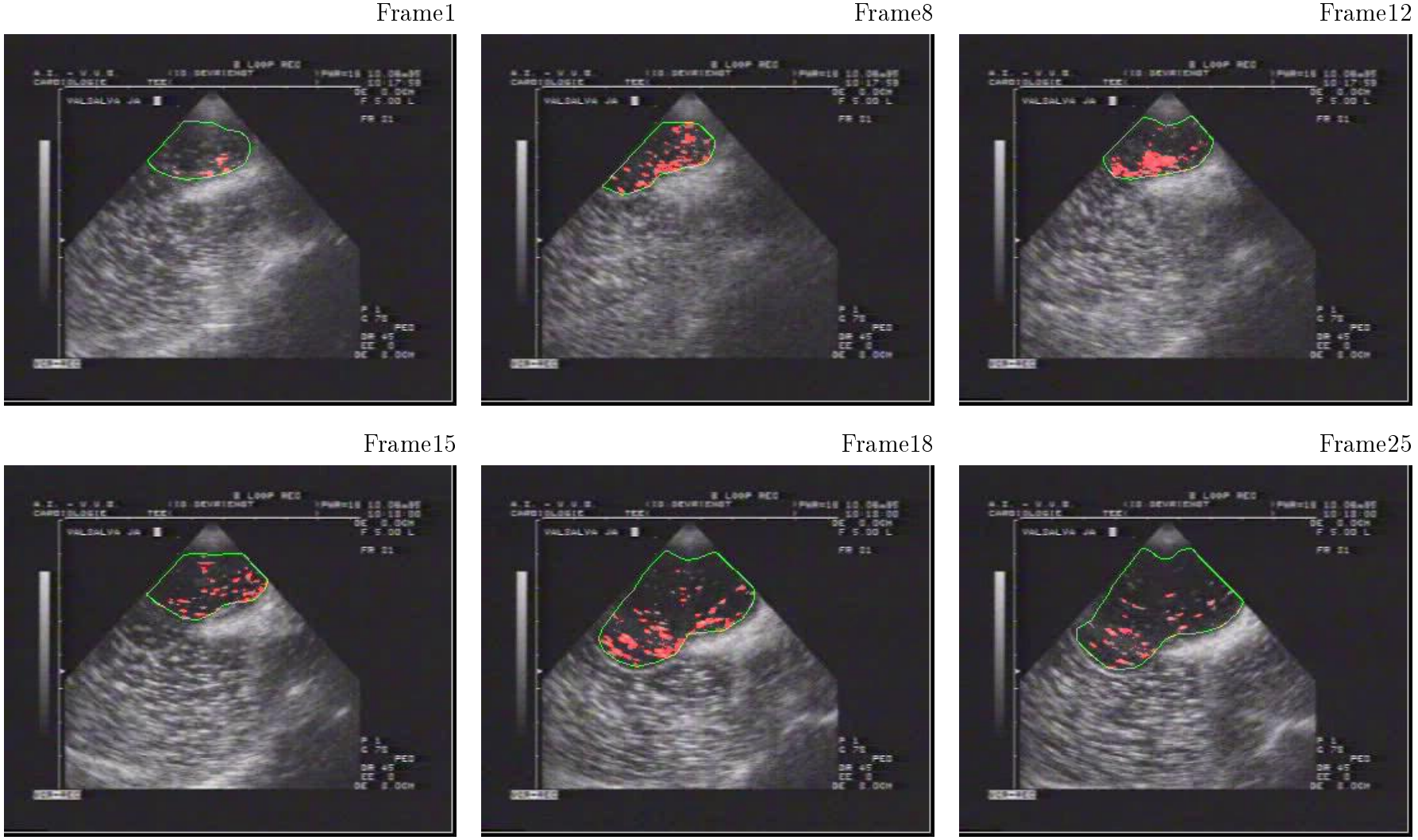

Figure 5.14 Effect of dynamic ROI (green, rectangle) for bubble detection (red regions).

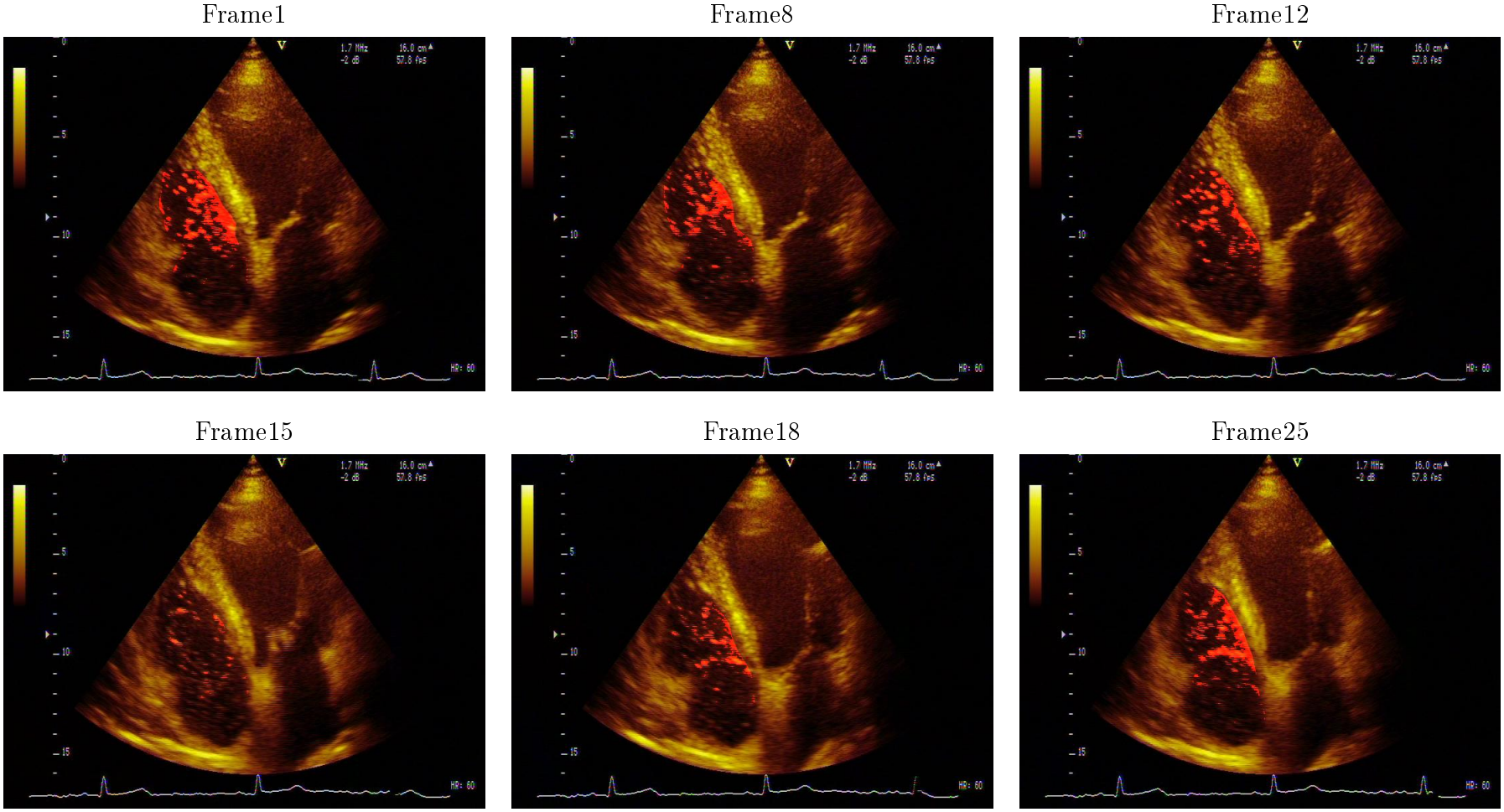

Figure 5.15 Detection of bubble in cTTE for 1 sec (25fps).

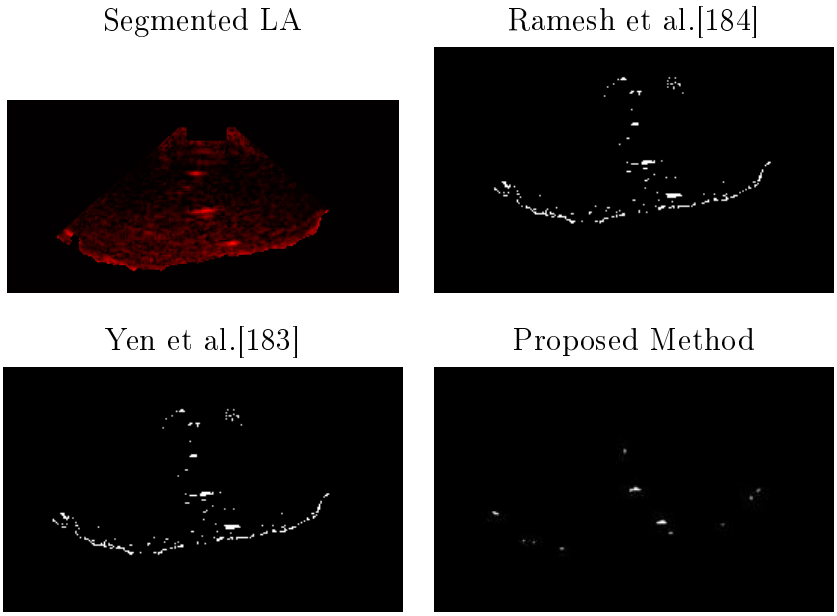

Figure 5.16 Comparison of three different methods in TEE

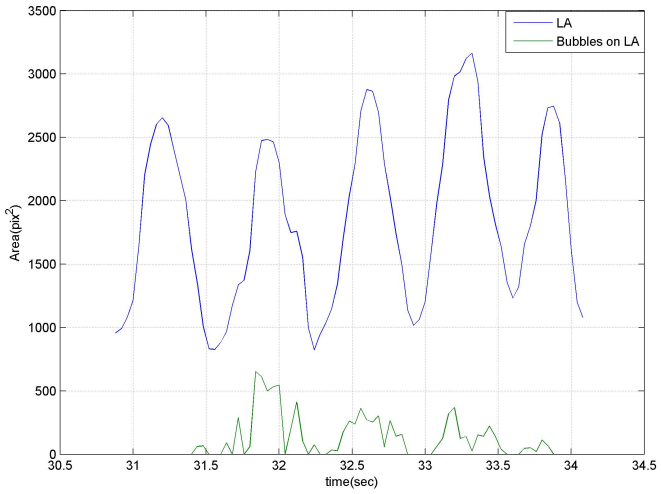

Figure 5.17 Evaluation of the size of LA and bubbles through cTEE.

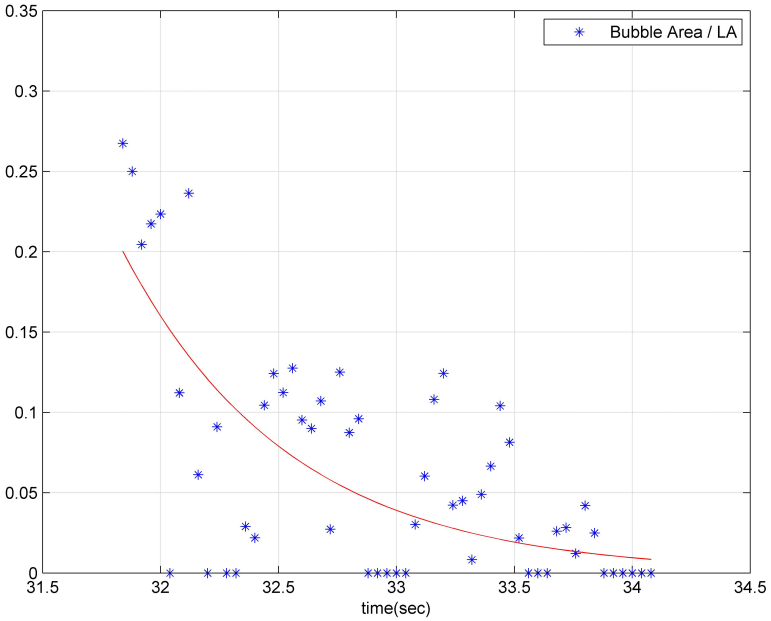

Figure 5.18 Evaluation of the clearance of bubbles within LA through cTEE.

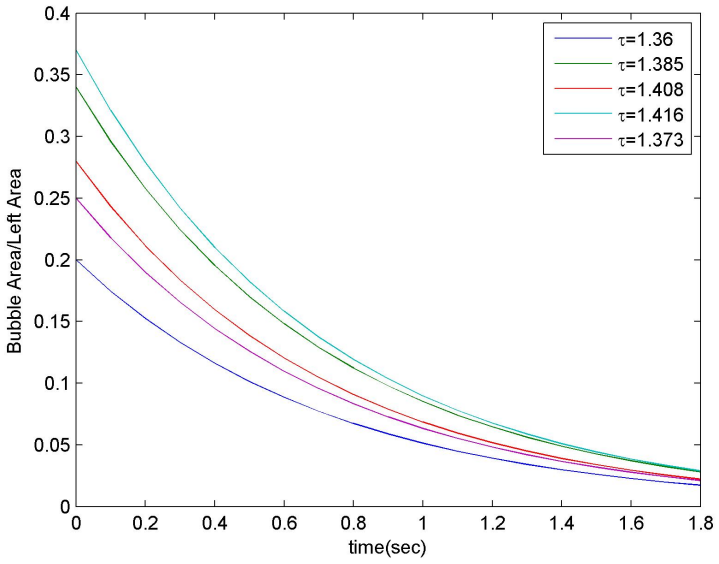

Figure 5.19 Evaluation of the clearance of bubbles for different subjects through cTEE where τ depicts the decay parameter of the first order system.

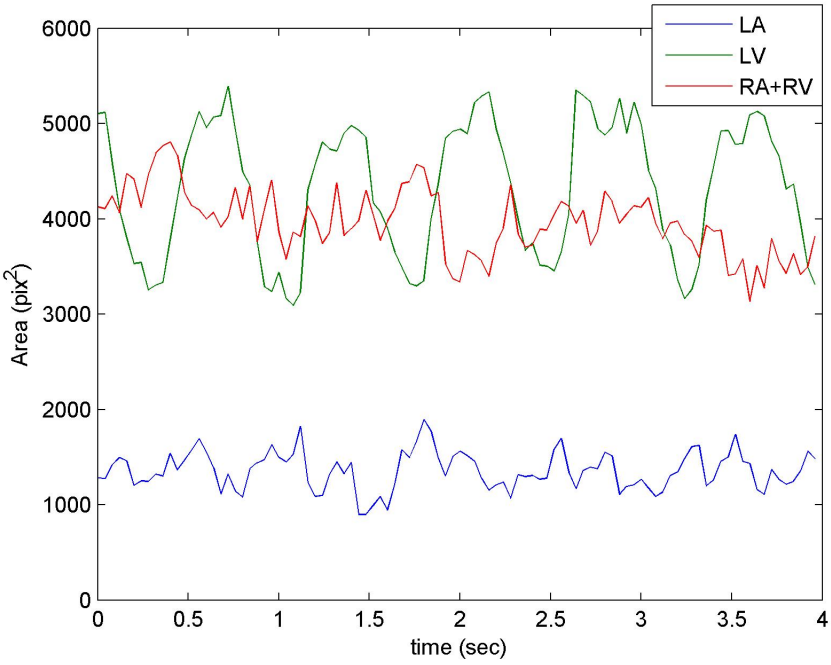

Figure 5.20 Evaluation of the size of LA, RA, LV and RV through cTTE.

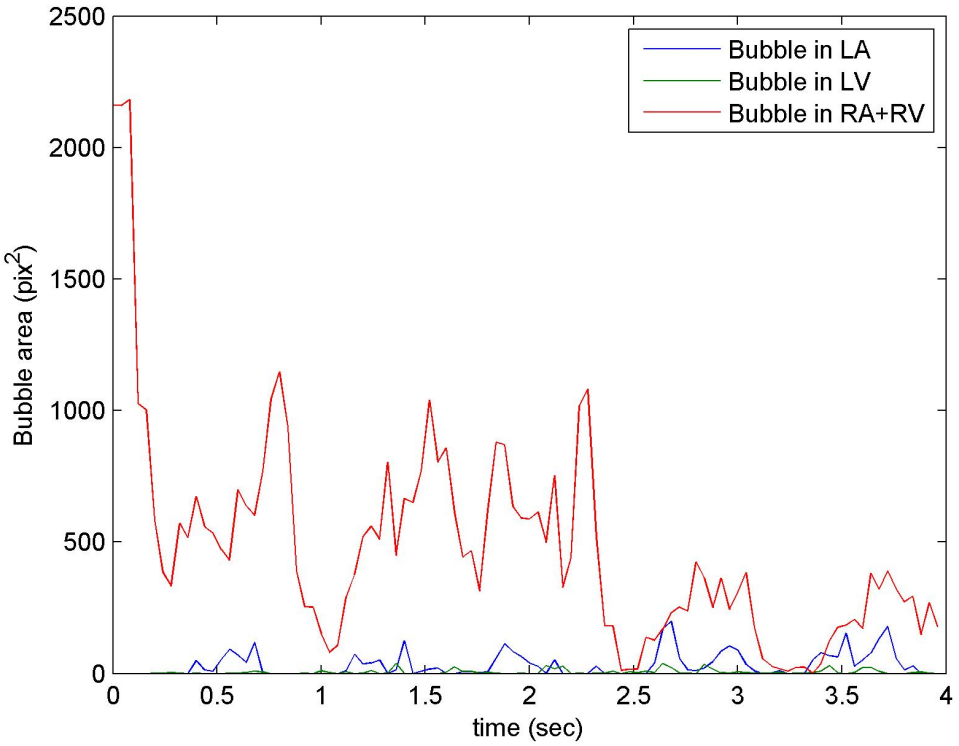

Figure 5.21 Evaluation of the clearance of bubbles within RA and RV through cTTE.

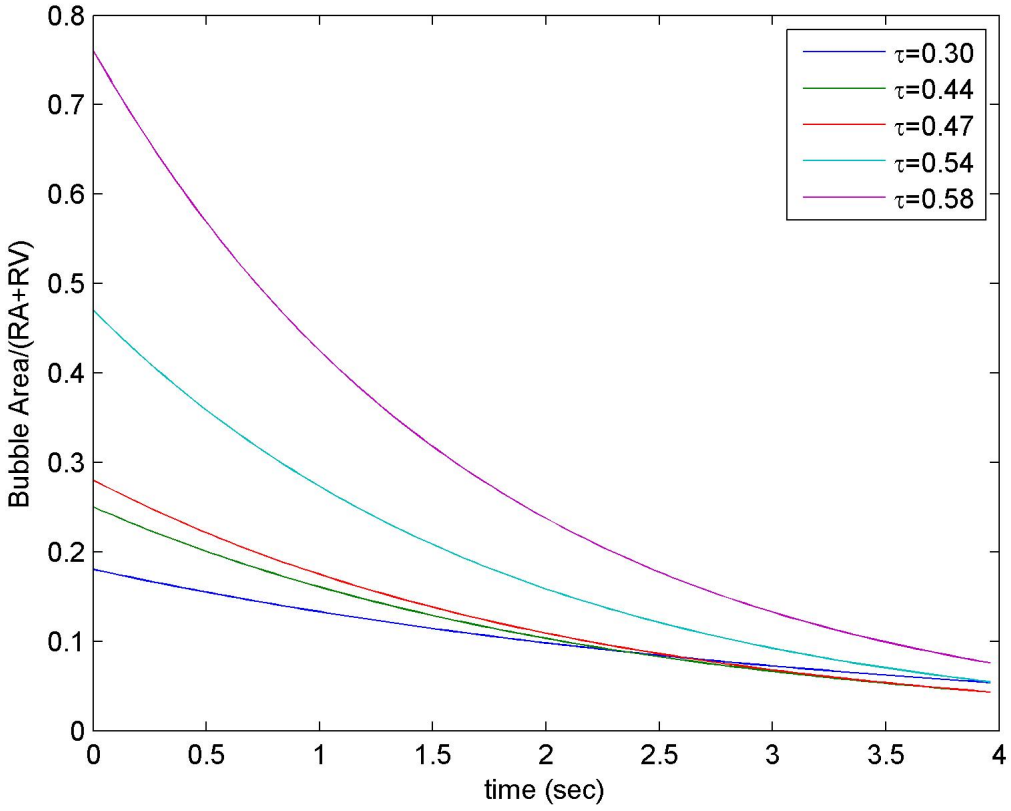

Figure 5.22 Evaluation of the clearance of bubbles for different subjects through cTTE where τ depicts the decay parameter of the first order system.

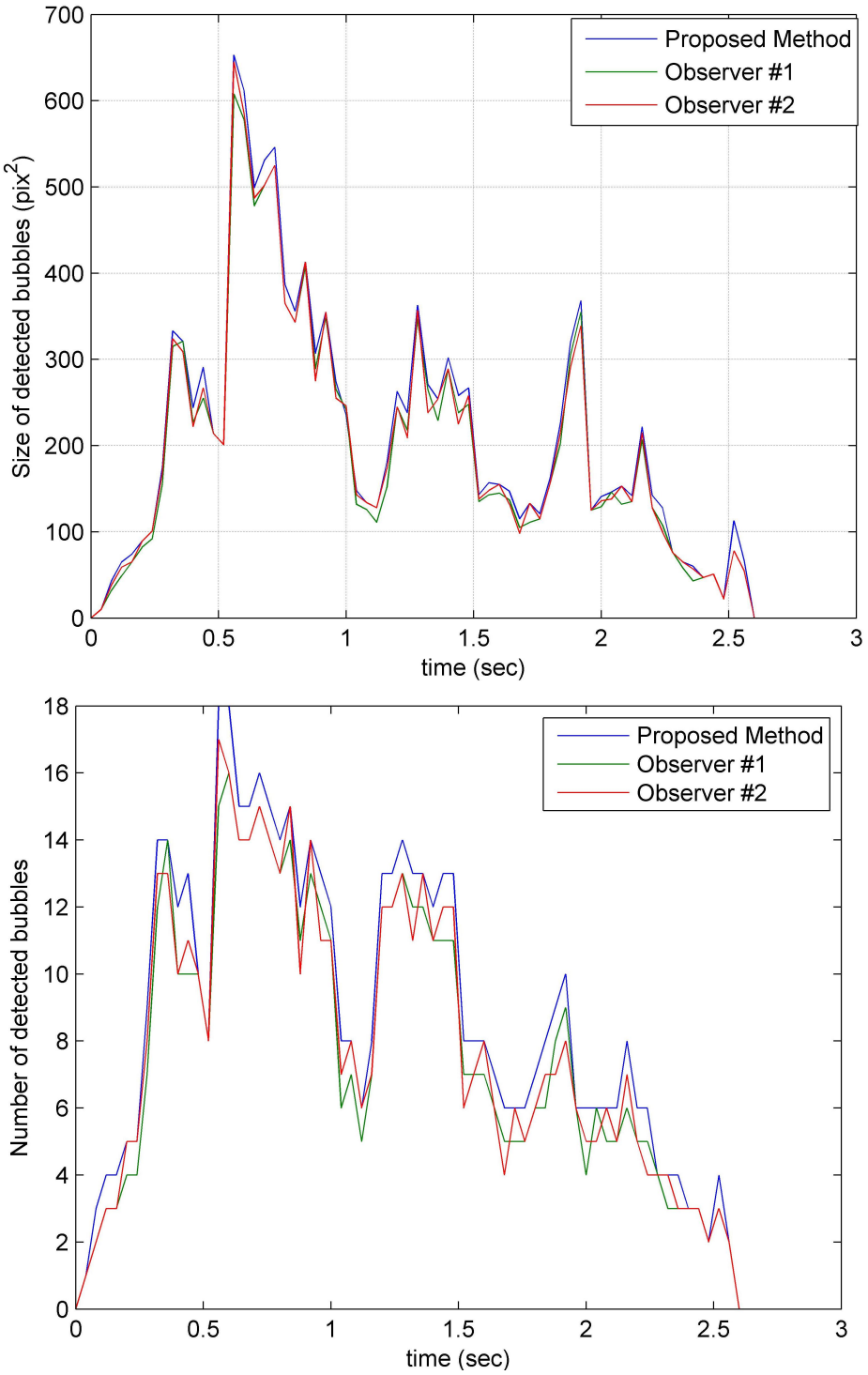

Figure 5.23 Number and total area of detected bubbles for a subject Grade 1 in low resolution video record.

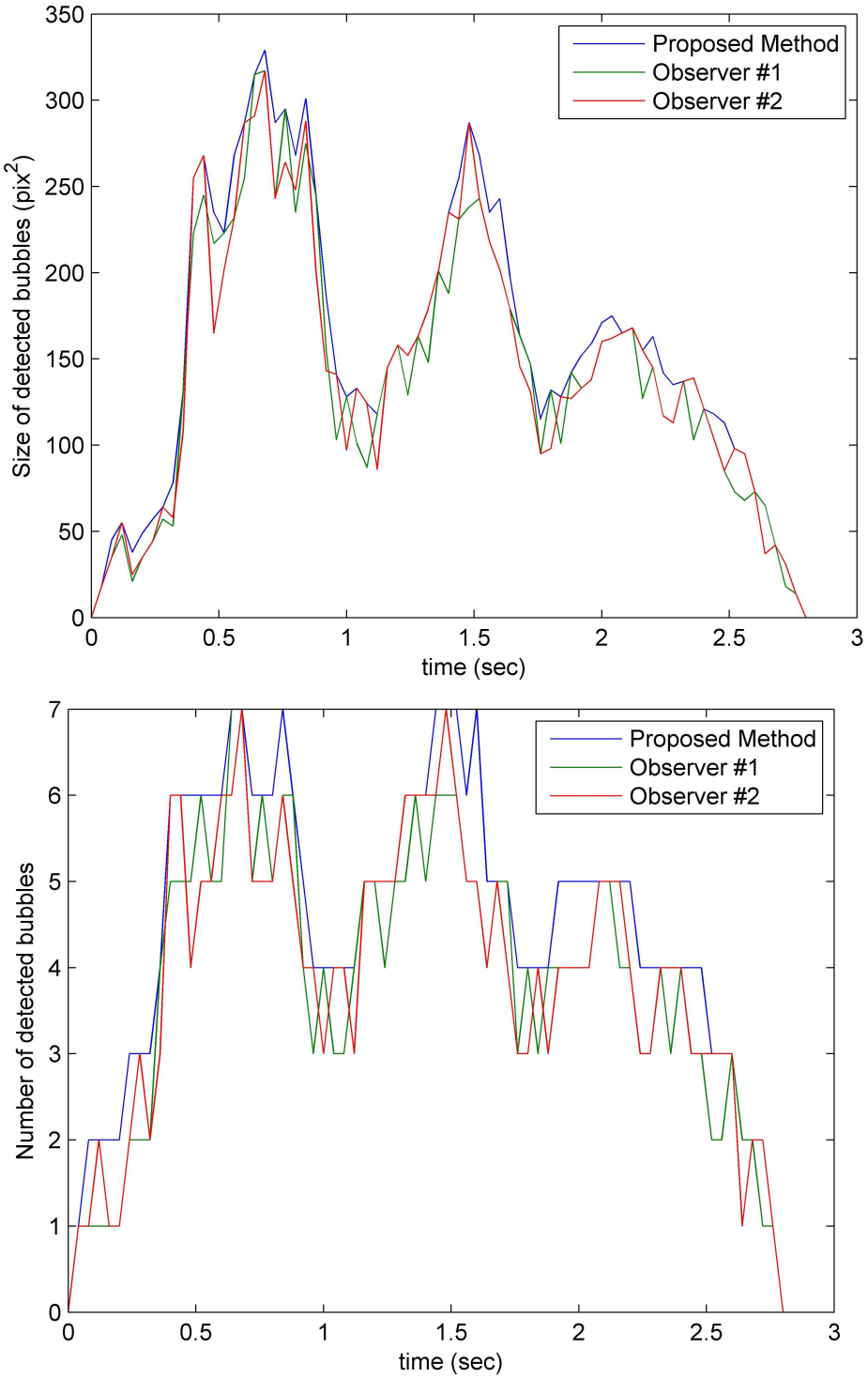

Figure 5.24 Number and total area of detected bubbles for a subject Grade 1 in high resolution video record.

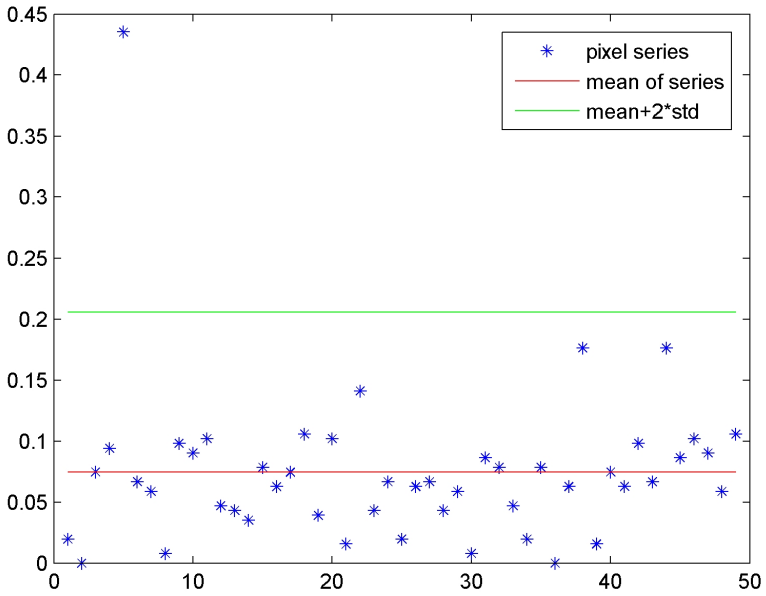

Figure 5.25 Dynamic thresholding of pixel through intensity in proposed method.

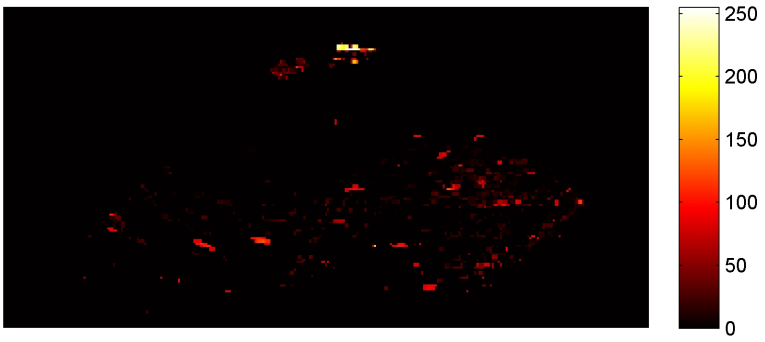

Figure 5.26 Bubble map of video sequence.

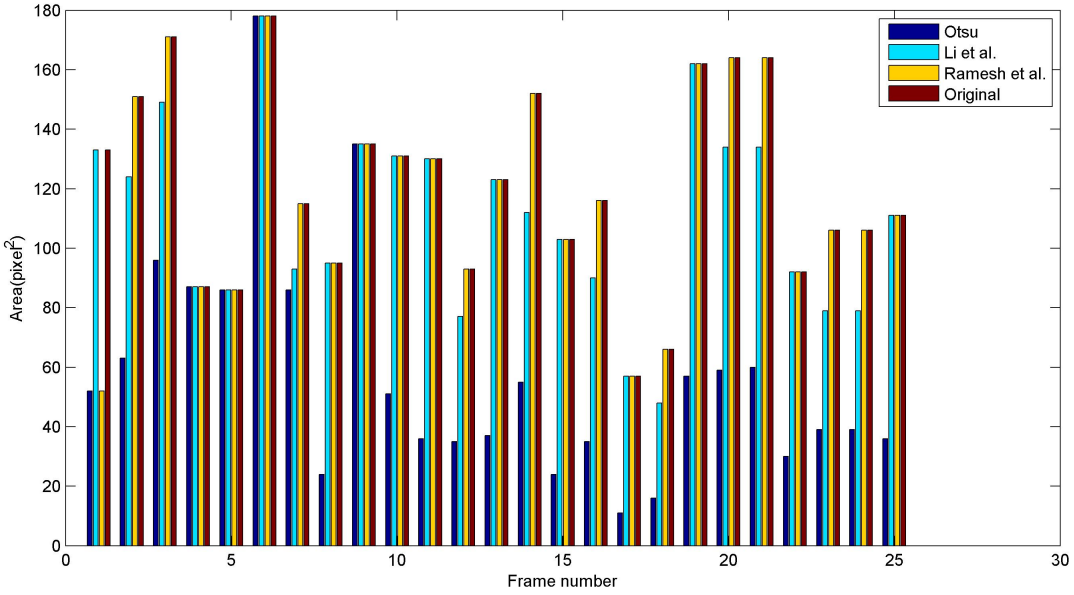

Figure 5.27 Without noise.

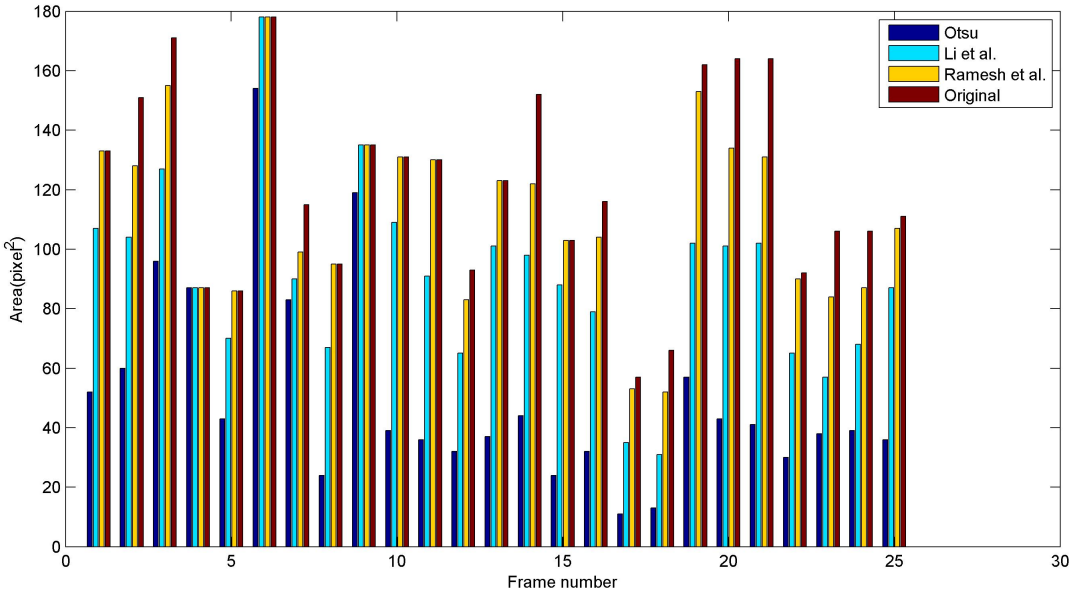

Figure 5.28 Speckle noise 0.1.

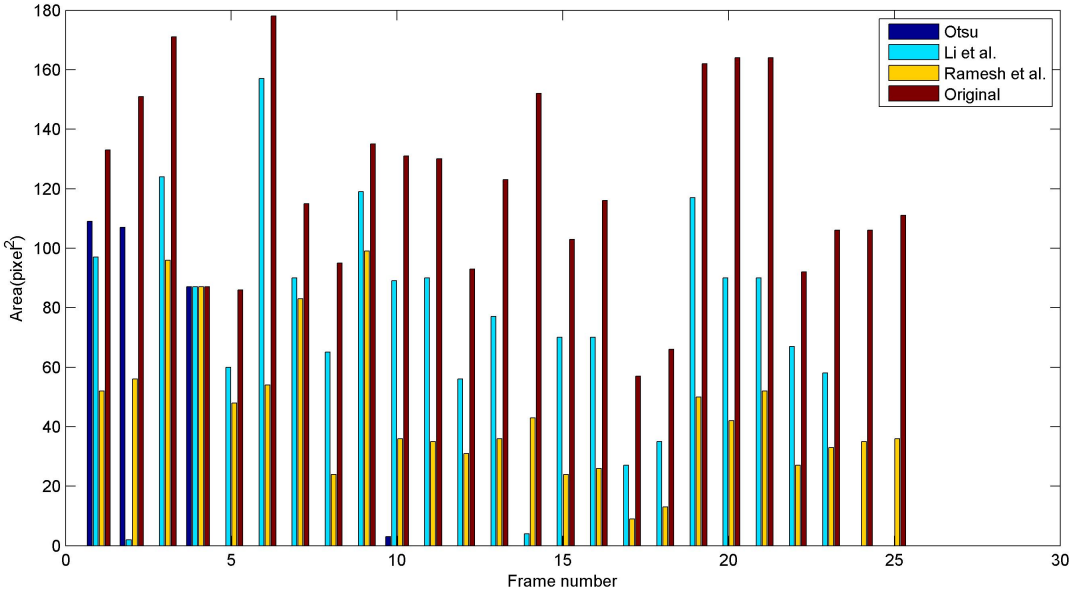

Figure 5.29 Speckle noise 0.2.

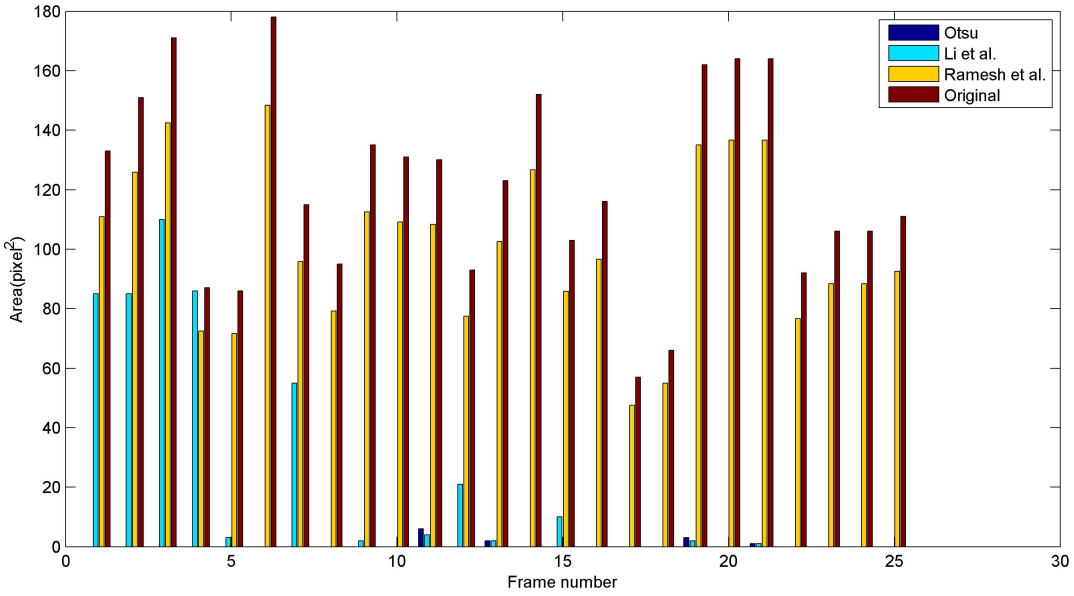

Figure 5.30 Speckle noise 0.3.

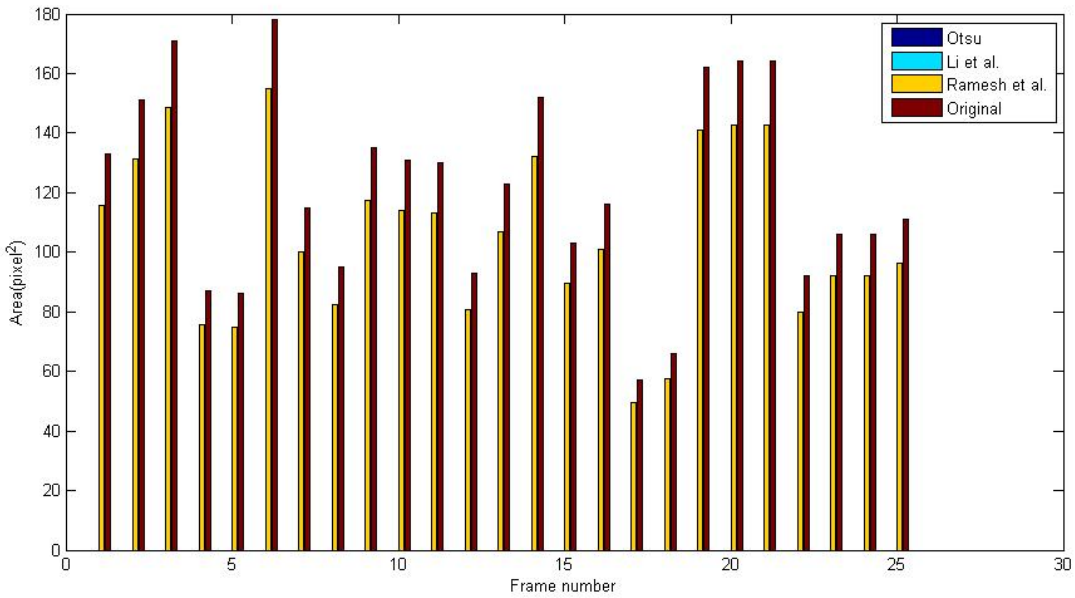

Figure 5.31 Speckle noise 0.5.

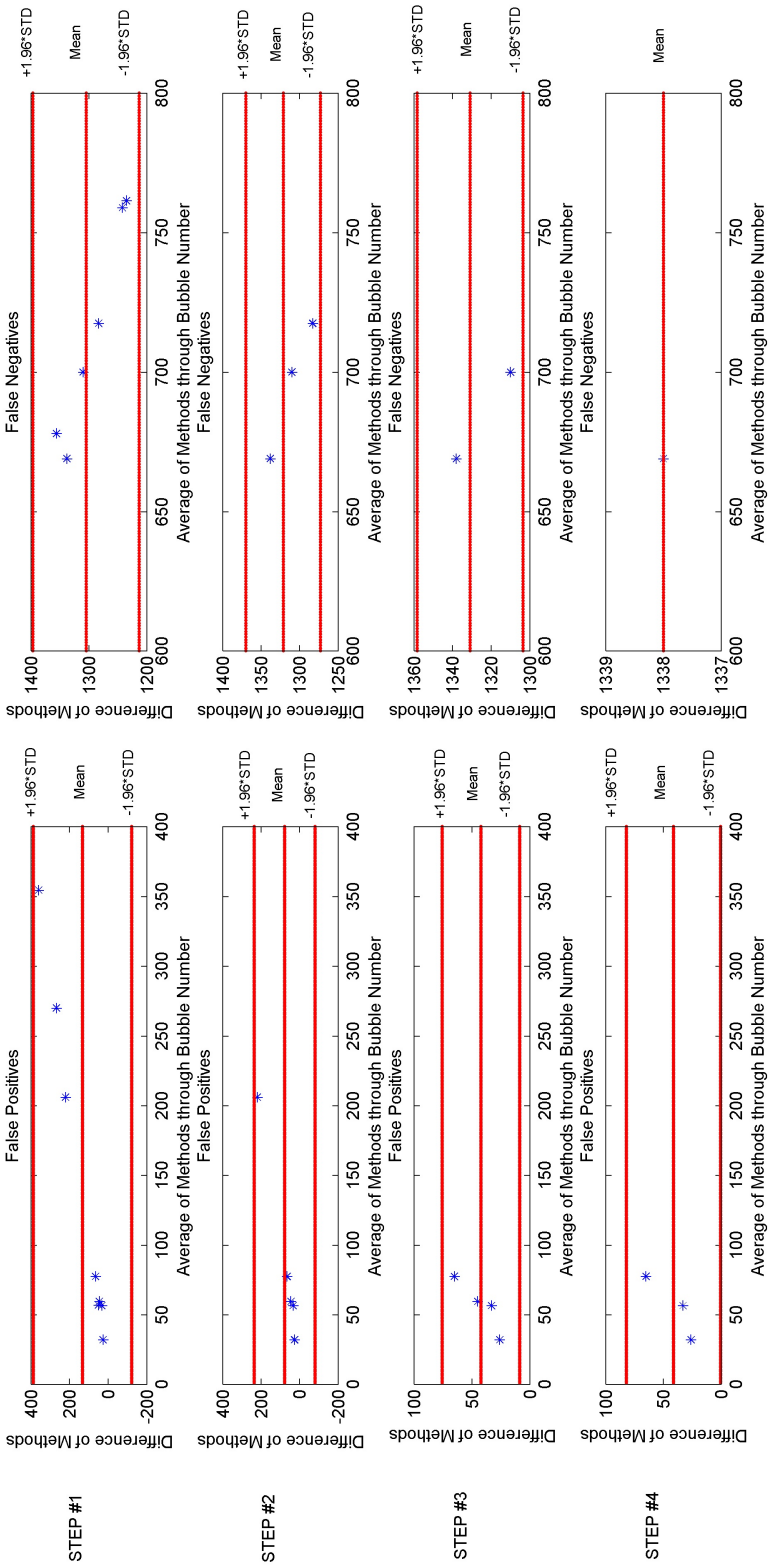

Figure 5.32 Performance analysis of the eight methods using Bland Altman method.

6. DISCUSSION

CPFO is considered as a silent atrial shunt in normal conditions. It is interpreted as a congenital disease or defect regarding the viewpoint of the study. Mainly, CPFO studies in medical literature were oriented either to reveal its anatomical epidemiology or to find its existence and relationship with other diseases. These major illnesses are categorized within stroke, DCS, paradoxical embolism and migraine which affect patients whose epicrisis is not related with CPFO.

On the other hand, CPFO studies with engineering aspects were mostly focused on either its diagnosis or automatic assessment with the measurement of crossed bubbles in a semi-automatic manner. Theses routines provided computational utilities to measure the functionality of this aperture through total number of microemboli crossing CPFO.

Clinically, CPFO studies have three major aspects; anatomical perspective in *post-mortem* studies, congenital perspective as a combined disease in a broad range from stroke to migraine and finally a silent microemboli gateway in extreme conditions such as hypobaric and hyperbaric environments.

The CPFO imaging and diagnosis are generally done via ultrasonographic technologies. On the other hand some prospective approaches and newer grading techniques were proposed recently [97, 115, 119].

Even if saline injected TTE and TEE modalities are mostly in clinical use, there are still discussions about the standardization and the subjectivity between CPFO and bubbles. At this point two questions arise for correct CPFO detection and microemboli grading either in normal conditions or in post decompression period. The first problem is that CPFO size measurement would be accurate than bubble counting due to the heterogeneity of bubbles in contrast solution which cause a variation in signal power

for ultrasonography [116]. Even if this remark would be seen as logical if we are doing an anatomical research, it is important to recall that bubble injection reveals how IAS active so the functionality of congenital disease. Furthermore, this approach would bring a physiological information of bubble clearance in circulation as it is described in Figure 5.23 and 5.24. The second problem is the subjectivity of bubbles or how bubbles would lie [189]. Bubbles would lie when a correct positioning of ultrasound probe has not considered or a correct manoever like high strain Valsalva has not achieved, therefore, bubbles would not be considered guilty to cause a misgrading [189, 28]. Therefore, the experience of the clinician would confer a correct diagnosis of CPFO during the acquisition and microemboli observation [110].

In this thesis, we adopted both aspects of CPFO studies. Firstly, qualitative and quantitative methods were developed to resolve the assessment problem as it can be considered like the engineering aspect of our work. Secondly, provided methods were applied to assess CPFO and its relationship with DCS for medical viewpoints.

When detecting microemboli on echocardiographic frames, we were faced with the dilemma; counting only the number of bubbles or recognizing them with their morphological information such as area, centroid, convex hull and perimeter. In both approaches there are advantages and disadvantages. While the first one can be solved with good training set, the second one does not necessiate any a priori analysis for microemboli recognition. On the other hand, a segmentation step is indispensable for quantitative analysis to reveal the target area in which the bubbles will be analyzed. This step introduces additional computational time since an iterative contour evaluation converges to the relevant cardiac chamber. Furthermore, the first approach is structured as a qualitative approach without image segmentation destined to give bubble number with its distribution on cardiac chambers.

Endocardial contours are essential to manipulate both qualitative and quantitative information about cardiac physiology and functionality. Due to blurring effects of speckle noise, probe and patient motions and elasticity of the contours, the performance of fundamental methods such as morphological operators, image binarization, and edge

detection are not satisfactory [174, 175, 190]. Either these methods bring boundary structures into segmented area or they fail without generating a corresponding output. These remarks are almost evident in low resolution images where noise level increases due to circulation turbulence near chamber walls and during subject movements.

As it can be observed from Figure 5.12 and 5.13, placing a fixed ROI may lead to erroneous results. CPFO grading should be done by taking into account entirely all bubbles which may exist in 2D Echocardiography modalities. It is almost obvious that static ROIs would miss bubbles even if a relevant threshold is already set. Furthermore, it is crucial to note that a bubble which transverses the septal wall might be skipped or be identified as a blur even though its contrast is within the histogram band of bubble recognition. Static segmentation lowers obviously the sensitivity of detection methods even if the specificity may remain higher. When the detection procedures are applied on statically segmented areas, we missed bubbles within LA but out of segmented areas.

Thresholding routines compared with the observations of the experts are in an acceptable range. Especially, median prefiltering and pixelwise thresholding give valid results in terms of low false positive ratio, higher sensitivity and specificity. Method 1, 4 and 8 also have higher sensitivities but their specificities are lower. Positive and Negative likelihood ratios are meaningful when they are greater than 1. Method 5, 8, 7, 3 and 7 have positive likelihood ratios greater than 5 and negative likelihood ratios less than 0.2 for dynamic segmentation. We infer that these procedures would bring a priori information for medical survey of bubble detection in CPFO. Both Positive and Negative predictive values which are close to 1 mean that these methods are more convenient to bring the information about bubble detection using post-test probability. Method 5, 1, 8 and 7 satisfy this inference for detection statistics.

Bland-Altman plots are important to depict the performance of eight detection procedures (Figure 5.32). This analysis is achieved recursively by excluding diverged methods which are close to 1.96 times standard deviation bands. In step 1, method 4, 2 and 3 are excluded. In step 2, method 6 is excluded. Finally in step 3, method 7 is

extracted. These methods are close to +1.96 times standard deviation band. Bland Altman is a powerful analysis to compare methods which introduce some errors. In our study these errors are characterized with Type 1 and Type 2 errors. Finally we infer that that Method 5, 1 and 8 have less false positive values than others because in step 4, limits of agreement are coincided with mean band for false negatives.

We note that spatial thresholding does not have a drastic effect on bubble detection. However, it filters out noisy spots which always exist on both high and low resolution frames. We infer that small structures especially close to chamber walls or CPFO aperture generally increase the false positive ratio. This is also correlated with image quality. In spatial thresholding, bubbles and bubble like structures are considered as ellipses [180]-[181] instead of star shape or lozenge structures [5]. Therefore, they are tagged and thresholded spatially with respect to elliptic axes.

The size of bubbles and cardiac chambers are found important to evaluate the functional activity of CPFO. For this purpose, bubble size was observed in details for both cTEE and cTTE. In Figure 5.18 and Figure 5.21, the mutual evaluation of bubble size was observed for the same subject. It is remarkable that in Figure 5.21 all bubbles in every chamber (LA,LV,RA and RV) could be observed. At the same time, this evaluation with cTTE requires a good angle of view in B-mode (4 chambers apical view), whereas cTEE offers accurate but limited views of LA.

The evaluation and coincidence of both chambers and bubbles support our hypothesis for a quantitative analysis of CPFO functionality. By interpreting synchronized plots, LA increases in size over three or four cycles that are consistent with the fact that after a 10 seconds straining, the right heart is almost empty and so the filling of the LA is also decreased. During atrial systole, bubble size is close to zero.

Temporal evaluation of cardiac chambers were performed through cTEE and cTTE in Figure 5.17 and Figure 5.20, respectively. In the same steps, bubble areas were also observed and the synchronized contraction phases helped us to determine a correct behaviour of the bubbles. At the beginning of CPFO shunt opening (31.5 sec)

some bubbles started to cross the septum in Figure 5.17. As it might be observed, when the shunt reached to its maximum size, the decay in total bubble area was observed whereas LA chamber conserved its size during the cycles.

In order to observe the time response of bubble behaviour, a systematic representation is necessary. Regarding the time response in Figure 5.17 and Figure 5.21, a decay of size could be observed in time. For this purpose, a first order exponential decay function $f(x) = A * exp^{-\tau * x}$ was used to observe time dynamics of bubble behaviour. Fitting a curve was achieved for five different subjects in both cTEE and cTTE. Bubble dynamics in these cases were presented in Figure 5.19 and Figure 5.22 Time constants; τ are estimated as between 1.36 and 1.41 for cTEE and between 0.3 and 0.58 for cTTE. It should be remarked that during atrial systole bubble size is close to zero in cTEE. Therefore, a limited view of LA might introduce a deviation in time dynamics of bubble activity during automatic analysis.

Larger bubble areas were recognized just after injection and maneuver-coughing (Figure 5.18). The contrast of bubbles are less bright than neighborhood structures such as endocardial wall, septum and the valves. As it was notified in Figure 5.18, the total bubble area and the total number of bubbles reach to their maximum at the half of cycle. Moreover, time response of bubbles was found as a meaningful criterion to guided the observer to analyze in depth the process starting from 10-15 sec after saline injection to the end of detection analysis.

We consider that this technique can be used in the evaluation of decompression and the effective analysis of induced bubbles in both diving and aerospace medicine. In grading, if the number of bubbles is high, specialists generally do not need to be able to count them precisely, they state only as grade 2. On the other hand, while decompression stress after dive is evaluated, precise bubble counting is much more important. We note that our approach would also provide an objective and automated bubble count in those applications where examination and duration of bubble decay are longer.

Consequently, it is remarkable that the results offer a good internal validity environment for CPFO evaluation and grading.

We conclude that there is a tradeoff between two modalities; cTEE and cTTE in our study. Even Di Tullio et al. [94] associated TTE as the least sensitive technique in CPFO detection; we found that the results are reasonable for grading. In image analysis we remark that the noise level and resolution are the bottleneck factors for real-time or offline analysis. Even though specialists may suffer due to these factors in real-time analysis, they may adjust image qualifications on echocardiogram side. However, in offline analysis, assessment and bubble detection are limited with the properties of recorded frames. Therefore, image standardization is a requirement for objectivity. We conclude that image acquisition protocols and standardization would bring new opportunities for CPFO assessment and grading.

7. CONCLUSION and FURTHER RECOMMENDATIONS

Visual interpretation of the examination of congenital defects requires high experience and patience within long lasting records. This problem meditates the necessity of a robust and reliable method. For an expert it is easier to measure the anatomical landmarks of right-to shunts than to detect and analyze bubbles by marking manually. However, this analysis which requires forward-backward steps in video frames ensures a better explanation of the functionality of bubble behavior. Therefore the correlation between defects and bubbles reflects also how long cardiac chambers will respond to bubble travel in cardiopulmonary system. This information is implicitly related with the capacity of pulmonary shunting.

In echocardiography, speckle noise level, frame resolution, video codecs and extensions are major factors that would reduce or optimize the objective assessment in both manual and computational surveys. Even though specialists may suffer due to these factors in real-time analysis, they may adjust image qualifications on echocardiogram side. However in offline analysis, assessment and bubble detection are limited with the properties of recorded frames. Therefore image standardization is a requirement for objectivity. We conclude that standardization in the visualization of right-to-left shunts and the grading protocols for bubble interpretation would benefit from the advantages of our proposed approach CPFO assessment and grading.

As future work, the analysis of CPFO-Microemboli association would also be extended as a clinical tool to analyze long lasting videos. This procedure would be also extended to the longitudinal analysis of echocardiographic records in DCS and especially in post decompression phase. It is well known that bubbles travelling in this period would be a potential threat to generate several diseases. Another potential application area would be the fusion of our proposed method within Transcranial Doppler modality. It is known that microemboli is a source to trigger migraine. Generally bubbles which cross CPFO promote this disease and TCD is preferred for monitoring. Furthermore,

bubble tracking is a wide area studied by mechanial engineers in order to modelize industrial process to prevent unwanted interactions between surfaces in liquid(s)-to-liquid(s) or liquid(s)-to-solid(s). This well known problem can be studied in medicine using new approaches developed in other areas to overcome the limitations arising from imaging restrictions, chaotic nature of circulation, non-Newtonian behavior of blood and especially unpredictable nature of microemboli.

APPENDIX A. MATHEMATICAL FOUNDATIONS of QUANTITATIVE DETECTION

The following thresholding methods were used in the quantitative microemboli detection. In this section, the mathematical background were summarized within their algorithmic steps.

A.1 Beghdadi's Method

Beghdadi et al.[9] proposed a new approach based on block source model where distribution-free local analysis of the image is used. To measure the entropy associated with a given experiment let x be defined as a random variable and $P(x)$ denotes its probability function. Let consider an input digital image of size N which has gray level pixels. In this case, the probability P_k that a pixel (i, j) randomly selected from that image will have some gray-level which is approximated by the relative frequency (N_k/N). If there is some prior measure m_k about that state k, the following measure would be used to calculate the entropy;

$$H = -\sum_k P_k log \frac{P_k}{m_k} \tag{A.1}$$

This represents the measure of the information content in the probability distribution P_k relative to the given prior m_k. If there is no prior knowledge, all m_k are equal to a constant which yields to Shannon entropy;

$$H = -\sum_k P_k log P_k \tag{A.2}$$

In order to define a probability distribution and an associated entropy, the image is analyzed with respect to a given source model. This model is composed of a window which is considered as a source of symbols corresponding to the gray level values of the pixels. Therefore, for each gray level threshold candidate, the two-tone image

composed of black and white pixels is analyzed through an elementary window. The optimal threshold level is determined such that the output image will be a compressed version of the input image containing the greatest amount of information associated with the given source symbol. Let A denote the grid of sample points of a picture of size

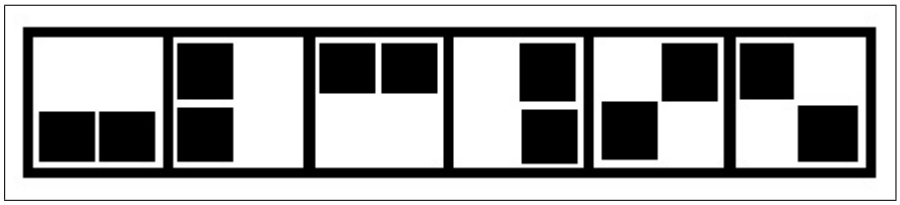

Figure A.1 Example of the possible symbols associated with a block source for $s = 2$ and $k = 2$ [9].

$L \times M$ and (i, j) the set of pixels in the image where $i = 1, 2, ..., L$ and $j = 1, 2, ..., M$ and g_{ij} the gray level of the (i, j)th pixel. For a gray level threshold t, A can be viewed as a set of juxtaposed binary blocks of size $m \times n$ pixels where each pixel of an original gray level g_{ij} is either black or white. The source is therefore, defined as the block.

A.2 Huang's Method

Huang et al. [185] developped a method using the measure of fuzziness in images to select an optimal threshold.

Let X denote an image set of size $M \times N$ with L levels and x_{mn} is the gray level of a (mn) pixel in X. Let $\mu_X(x_{mn})$ denote the membership value which represents the degree of possessing a certain property by the (m, n) pixel in X; that is a fuzzy subset of the image set X is a mapping μ from X into the interval [01]. In the notation of fuzzy set, the image set X is represented as;

$$X = \{(x_{mn}, \mu_X(x_{mn}))\} \tag{A.3}$$

where $0 \leq \mu_X(x_{mn}) \leq 1$, $m = 0, 1, \ldots, M-1$ and $n = 0, 1, \ldots, N-1$. The membership function $\mu_X(x_{mn})$ is viewed as a characteristic function that represents the fuzziness of a (m, n) pixel in X. Each pixel in the image has a fuzzy relationship with its belonging

region; the object or the background. Hence, the membership value of a pixel in X is defined regarding this relationship.

Let $h(g)$ denote the number of occurences at the gray level g in an image. Given a certain threshold value t, the average gray levels of the backround μ_0 and the object μ_1 can be obtained as follows;

$$\begin{aligned} \mu_0 &= \textstyle\sum_{g=0}^{t} g h(g) / \sum_{g=0}^{t} h(g) \\ \mu_1 &= \textstyle\sum_{g=t+1}^{L-1} g h(g) / \sum_{g=t+1}^{L-1} h(g) \end{aligned} \tag{A.4}$$

The average gray levels, μ_0 and μ_1 are considered as the target values of the background and the object for threshold t. The relationship berween a pixel in X and its belonging region should intuitively depend on the difference of its gray level and the target value of its belonging region. Thus, the membership function that evaluates the above relationship for a (m, n) pixel is defined as;

$$\begin{aligned} \mu_X(x_{mn}) &= \tfrac{1}{1+|x_{mn}-\mu_0|/C} \qquad \text{if} \qquad x_{mn} \leq t \\ &= \tfrac{1}{1+|x_{mn}-\mu_1|/C} \qquad \text{if} \qquad x_{mn} > t \end{aligned} \tag{A.5}$$

where C is a constant value $1/2 \leq \mu_X(x_{mn}) \leq 1$. For a given t any pixel in the input image should belong to either the object or the background. Hence, it is expected that the membership value of any pixel should be no less than 0.5.

The measure of fuzziness usually indicates the degree of fuzziness of a fuzzy set. The entropy which is used as a measure of fuzziness would be adapted in fuzzy set using the Shannon fuction. For a fuzzy set A, the entropy is given by;

$$E(A) = \frac{1}{nln2} \sum_i S(\mu_A(x_i)), \qquad \text{i=1,2,...,n} \tag{A.6}$$

$$S(\mu_A(x_i)) = -\mu_A(x_i) ln[\mu_A(x_i)] - [1-\mu_A(x_i)] ln[1-\mu_A(x_i)] \tag{A.7}$$

When the entropy is extended to two dimensional plane, the entropy of an image X;

$$E(X) = \frac{1}{MNln2} \sum_m \sum_n S(\mu_x(x_{mn}) \tag{A.8}$$

with $m = 0, 1, \ldots, M-1$ and $n = 0, 1, \ldots, N-1$ Using the histogram h;

$$E(X) = \frac{1}{MNln2} \sum_g S(\mu_X(g))h(g) \qquad g = 0, 1, \ldots, L-1 \tag{A.9}$$

Shannon's function is monotonically increasing in the interval [0,0.5] and decreasing in the interval [0.5, 1]. When $\mu_X(x_{mn})$=0.5 for all m and n, the entropy E will have the maximum measure of fuzziness. The entropy E should have the following properties;

1. $0 \leq E(X) \leq 1$
2. $E(X)$ has the minimum value 0, if $\mu_X(x_{mn}) = 0$ or 1 for all (m, n)
3. $E(X)$ has the maximum value 1, if $\mu_X(x_{mn}) = 0.5$ for all (m, n)
4. $E(X) \leq E(X')$, if X is crisper than X'.
5. $E(X) = E(\bar{X})$ where $\bar{X}$ is the complement of X.

The measure of fuzziness should be dependent on the relationship betwen the fuzzy set A and its complement $\bar{A}$. Therefore, it would be defined a measure of fuzziness as the measure of lack of distinction between A and its complement $\bar{A}$. The distance between a fuzzy image set X and its complement $\bar{X}$ is defined as follows;

$$D_p(X, \bar{X}) = [\textstyle\sum_m \sum_n |\mu_X(x_{mn}) - \mu_{\bar{X}}(x_{mn})|^p]^{1/p} \quad p = 1, 2, 3, \ldots \tag{A.10}$$

where$\mu_{\bar{X}}(x_{mn}) = 1 - \mu_X(x_{mn})$. Thus the measure of fuzziness of X can be denoted as;

$$\eta_p(X) = 1 - \frac{D_p(X, \bar{X})}{|X|^{1/p}} = 1 - \frac{D_p(X, \bar{X})}{(MN)^{1/p}} \tag{A.11}$$

To simplify the computation, the histogram would be used to compute $D_p(X, \bar{X})$;

$$D_p(X, \bar{X}) = \left[\sum_g |\mu_X(g) - \mu_{\bar{X}}(g)|^p\right]^{1/p} h(g), \quad g = 0, 1, \ldots, L-1. \tag{A.12}$$

For a given image set X, it is expected that the measure of fuzziness should be as small as possible. Hence, in this approach, the main goal is to select an optimal threshold value such that the measure of fuzziness of X is minimal.

Given an $M \times N$ image with L levels, let g_{max} and g_{min} represent the maximum and minimum gray levels, respectively and let $C = g_{max} - g_{min}$. Thus,

$$\begin{aligned} &S(t) = \textstyle\sum_{g=0}^{t} h(g) \\ &\bar{S}(t) = \textstyle\sum_{g=t+1}^{L-1} h(g) \qquad \bar{S}(L-1) = 0 \\ &W(t) = \textstyle\sum_{g=0}^{t} gh(g) \\ &\bar{W}(t) = \textstyle\sum_{g=t+1}^{L-1} gh(g) \quad \bar{S}(L-1) = 0 \end{aligned} \tag{A.13}$$

where $0 \leq t \leq L-1$. $S(L-1)$ and $W(L-1)$ are constant for an image. The algorithm is summarized as follows

- Step 0: Set the parameter p. Then, calculate $S(L-1)$ and $W(L-1)$ for the image. Given the threshold value $t = g_{min}$ let $S(t-1) = 0$ and $W(t-1) = 0$.
- Step 1: Compute

$$\begin{aligned} S(t) &= S(t-1) + h(t) \\ \bar{S}(t) &= S(L-1) - S(t) \\ W(t) &= W(t-1) + t \times h(t) \\ \bar{W}(t) &= W(L-1) - W(t) \end{aligned} \tag{A.14}$$

The average gray levels of the background and the object are obtained by

$$\begin{aligned} \mu_0 &= int[W(t)/S(t)] \\ \mu_1 &= int[\bar{W}(t)/\bar{S}(t)] \end{aligned} \tag{A.15}$$

where int[x] takes the integer value near the real x.

- Step 2: Compute the measure of fuzziness of the input image by using Eq. A.5,A.9,A.12.
- Step 3: Set $t = t + 1$ and go to Step 1 until $t = g_{max} - 1$.
- Step 4: Find the minimum measure to determine the optimal threshold value.

A.3 Li's Method

Li et al. [186] proposed an iterative method to get an optimal threshold which minimizes the cross entropy. For a histogram h on the gray level $[1, L]$ the zeroth and the first moments of the foreground and background portions of the thresholded histogram are given as it follows;

$$\begin{array}{ll} m_{0a}(t) = \sum_{i=1}^{t-1} h(i) & m_{0b}(t) = \sum_{i=t}^{L} h(i) \\ m_{1a}(t) = \sum_{i=1}^{t-1} ih(i) & m_{0b}(t) = \sum_{i=t}^{L} ih(i) \end{array} \tag{A.16}$$

Their means are respectively;

$$\mu_a(t) = \frac{m_{1a}(t)}{m_{0a}(t)} \quad \mu_b(t) = \frac{m_{1b}(t)}{m_{0b}(t)} \tag{A.17}$$

The minimum cross entropy method selects the threshold which minimizes the cross entropy of the image and its segmented version. The object function to minimize is;

$$\eta(t) = -m_{1a}(t)log(\mu_a(t)) - m_{1b}(t)log(\mu_b(t) \tag{A.18}$$

Thus the optimal threshold is; $t_{op} = argmin_t \eta t$

The calculation of the optimal threshold involves the evaluation of $\eta(t)$ for all possible threshold values. The computation can be significantly reduced by developing a numerical method for the minimization. For this purpose, a necessary condition to set is to have the derivative of $\eta(t)$ to zero.

$$\eta'(t) = h(t)(tlog(\frac{\mu_a(t)}{\mu_b(t)}) - (\mu_a(t) - \mu_b(t)) \tag{A.19}$$

For $\eta'(t)$ to be zero, either $h(t) = 0$ or the second term is zero. As $h(t) = 0$ is satisfied only by those threshold values where the image does not contain such gray values, these solutions can be considered as trivial solutions to the thresholding problem. Therefore, the solution depends on the seros of the second term.Then, we get;

$$t = \frac{\mu_b(t) - \mu_a(t)}{log(\mu_b(t)) - log(\mu_a(t))} \tag{A.20}$$

In order to find the solution of optimal threshold, an iterative procedure is applied;

$$t_{n+1} = round(\frac{\mu_b(t_n) - \mu_a(t_n)}{log(\mu_b(t_n)) - log(\mu_a(t_n))}), n \geq 0 \tag{A.21}$$

where round function rounds each iteration to the nearest integer.

A.4 O'Gorman's Method

O'Gorman [188] proposed an approach based on the connectivity information in the images. As a convention the range of intensities has often 256 levels in a grayscale image. Even if a histogram thresholding may offer feasible results it is a global solution. On the other hand, local features such as the connectivity between the image regions would render a new aspect in the image thresholding.

The methodology in this approach would be summarized in three steps;

1. Determine a histogram of the number of horizontal and vertical runs that result from thresholding the original image at each intensity

2. Determine the sliding profile from the runs histogram. This yields a measure of flatness, or lackof variation of runs, for ranges around each intensity level in the runs histogram.

3. Determine the number of thresholds as the number of peaks on the sliding profile. Each threshold is located at the intesnsity within a peak at which the sliding

profile has maximum profile. The image pixels are then set to $n+1$ intensity levels as separated by the n threshold values.

In step 1, all possible binary images from the original image are determined by thresholding at each intensity level; then, for each binary image, the number of runs is counted. A *run* is a sequence of consecutive (connected) ON-valued pixels along a row or column.

Furthermore, the sliding profile is calculated in step 2. The objective is to find the plateaus on the runs histogram. The determination of the sliding is characterized as the measure of deviation around each intensity and is calculated as follows;

$$d_i = \sum_{j=-w/2}^{w/2} |R(i) - R(j)| \tag{A.22}$$

where d_i is the sum of differences within a window of width w at intensity i and $R(i)$ is the number of runs at that intensity. The sliding profile $P(i)$ at each intensity is determined as;

$$P_i = exp(-\frac{1}{2}(\frac{d_i}{\sigma})^2) \tag{A.23}$$

where σ is the standard deviation of the Gaussian-shaped curve.

Finally, the sliding profile is analyzed to determine the thresholds in step 3. The number of peaks that reach or are close to reaching the maximum. All ranges of intensity for which the values of sliding profile are within the expected flatness of deviation, ΔF, of the maximum are considered to indicated threshold ranges. The flatness deviation is defined as a percentage of the maximum profile. Therefore,

$$\text{Threshold ranges} : i_j \quad | \quad (P(i) > P_{max}(1 - \Delta F/100)) \quad j = 1, \ldots, L \tag{A.24}$$

where i_j indicates ranges of intensities for L threshold ranges.

A threshold within each threshold range is choosen as the intensity of the maxi-

mum profile value. This yields the intensity centered on the flattest portion of the runs histogram within that range.

$$T_j = maxP(i), for i \in i_j, \quad j = 1, \ldots, L \tag{A.25}$$

where T_j are the threshold values for $j = 1, \ldots, L$ threshold ranges.

After the determination of n threshold values, the image is thresholded into $n + 1$ levels. For example, for $n = 1$ thresholds, there are two levels of thresholded pixel values, those above and below the threshold. For $n = 2$ thresholds, there are three levels of thresholded pixel values; below the lower threshold, between the lower and the higher thresholds, and above the higher thresholds.

In Figure A.2, three steps of the method is illustrated. The grayscale image has three regions. Two regions (of sizes 5x5 and 6x6) have intensity level 4. The other region (size 4x4) has intensity level 12. When the original image is thresholded below level 4, each binary image has 30 runs (5+5+6+6+4+4) because all regions are above the threshold. For the thresholds between 4-12, only 8 runs from the 4x4 region are above threshold. There are no runs for thresholds of 12 and above. Finally, there are two plateaus on the same plot corresponding to two threshold ranges.

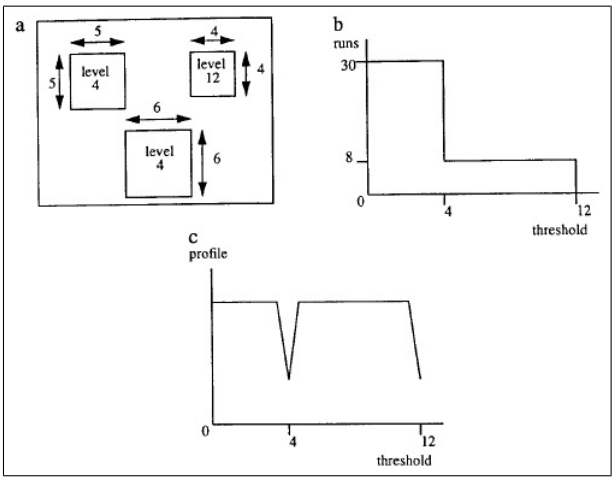

Figure A.2 Example showing three steps of the method; a-Original image with three regions. b-The runs histogram. c-Sliding profile from runs histogram.

A.5 Otsu's Method

Otsu [179] proposed a probablistic approach to solve the selection of optimal threshold. In a given picture of a gray level $[1, L]$ for a histogram h, the number of pixels at level i is denoted by n_i and the total number of pixels by $N = n_1+n_2+...+n_L$. The histogram h is normalized an considered as a probabilistic distribution;

$$p_i = \frac{n_i}{N} \quad p_i \geq 0, \quad \sum_{i=1}^{L} p_i = 1 \tag{A.26}$$

If the pixels would be separated into two groups C_0 and C_1 to gather background and foreground objects in a threshold level k; C_0 denotes pixels between $[1, k]$ and C_1 denotes pixels between $[k+1, L]$ respectively. The probabilities of class occurence and the class mean levels are given by;

$$\omega_0 = Pr(C_0) = \sum_{i=1}^{k} p_i = \omega(k) \tag{A.27}$$

$$\omega_1 = Pr(C_1) = \sum_{i=k+1}^{L} p_i = 1 - \omega(k) \tag{A.28}$$

and

$$\mu_0 = \sum_{i=1}^{k} iPr(i|C_0) = \sum_{i=1}^{k} ip_i/\omega_0 = \mu(k)\omega(k) \tag{A.29}$$

$$\mu_0 = \sum_{i=k+1}^{L} iPr(i|C_1) = \sum_{i=k+1}^{L} ip_i/\omega_1 = \frac{\mu_T - \mu(k)}{1 - \omega(k)} \tag{A.30}$$

where

$$\omega(k) = \sum_{i=1}^{k} p_i \quad \mu(k) = \sum_{i=1}^{k} ip_i \tag{A.31}$$

are the zeroth and the first order cumulative moments of the histogram up to the kth

level respectively, and

$$\mu_T = \mu(L) = \sum_{i=1}^{L} ip_i \tag{A.32}$$

is the total mean level of the original picture.

The variances of each class are given by

$$\sigma_0^2 = \sum_{i=1}^{k}(i-\mu_0)^2 Pr(i|C_0) = \sum_{i=1}^{k}(i-\mu_0)^2 p_i/\omega_0 \tag{A.33}$$

$$\sigma_1^2 = \sum_{i=k+1}^{L}(i-\mu_1)^2 Pr(i|C_1) = \sum_{i=k+1}^{L}(i-\mu_1)^2 p_i/\omega_1 \tag{A.34}$$

To evaluate the optimal threshold level, the following discriminant criterion measures are used;

$$\lambda = \sigma_B^2/\sigma_W^2 \quad \kappa = \sigma_T^2/\sigma_W^2 \quad \eta = \sigma_B^2/\sigma_T^2 \tag{A.35}$$

where

$$\begin{aligned} \sigma_W^2 &= \omega_0\sigma_0^2 + \omega_1\sigma_1^2 \\ \sigma_B^2 &= \omega_0\omega_1(\mu_1-\mu_0)^2 \\ \sigma_T^2 &= \textstyle\sum_{i=1}^{L}(i-\mu_T)^2 p_i \end{aligned} \tag{A.36}$$

are the within class variance, the between class variance and the total variance of levels respectively. The optimization problem is to search a threshold level k which will maximize one of the criterion measure. The discriminant criteria maximizing λ, κ and η respectively, for k are equivalent to one another; $\kappa = \lambda + 1$ and $\eta = \lambda/(\lambda+1)$ because $\sigma_W^2 + \sigma_B^2 = \sigma_T^2$

Therefore, the optimal threshold k^* that maximizes the criteria is;

$$\sigma_B^2(k^*) = \max_{1\le k<L} \sigma_B^2(k) \tag{A.37}$$

From the problem, the range of k over which the maximum is sought can be restricted to

$$S^* = \{k; \quad \omega_0\omega_1 = \omega(k)[1-\omega(k)] > 0, \quad or \quad 0 < \omega(k) < 1\} \tag{A.38}$$

This is called the effective range of the gray level histogram. Then, the criterion measure σ_B^2 or η takes a minimum value of zero for k such as $k \in S - S^* = \{k; \quad \omega(k) = 0 \text{ or } 1\}$ and takes a positive and bounded value for $k \in S^*$.

A.6 Palumbo's Method

Global thresholding techniques determine one threshold for converting the entire gray level image to binary image. If a pixel in the image is above the global threshold then it is converted to white (background) otherwise it is converted to black (foreground). Global thresholding is useful in simple situations. A common problem with this technique occurs when the gray level transition between the object and the background is gradual and inconsistent across objects in the image. Brightness, color gradient, noise are main pitfalls to set a global threshold.

On the other hand, local thresholding methods is an adaptive approach which considers a neighborhood of pixels around the pixel instead of taking the pixel alone. If the pixel is significantly darker than the neighboring pixels, it is converted to black; otherwise it is converted to white. Using this neighborhood information , the binary value for the pixel under consideration can be determined based upon local conditions and not just on a single threshold calculated from an image-wide standpoint. Using locally adaptive binarization techniques, a more top-down knowledqe-based approach is utilized to provide a better binarization. The intensity $I(x, y)$ of a pixel (x, y) in the input image is functionally compared to the intensities of pixels in a 9x9 neighborhood centered at the pixel and a binary value $Z(x, y)$ is output. The neighborhood is constructed as shown in Figure A.3. Area A_1 contains the pixels in the 3x3 neighborhood

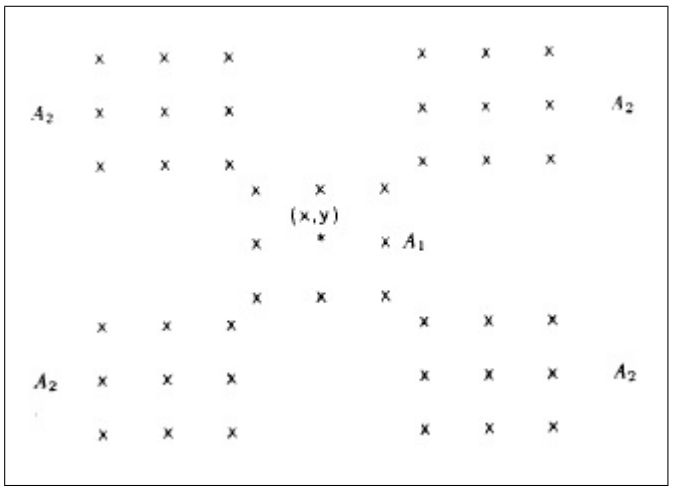

Figure A.3 Setup of neighborhood for Palumbo et al. [10].

about (x,y) and area A_2 contains the four 3x3 neighborhoods diagonally adjacent to A_1. This mask arrangement is presumably constructed so as to capture foreground pixels in area A_1 while the background is captured in area A_2 and vice versa. Pixels in A_1 are most significant in the comparison to determine an output value, those in A_2 are less significant and those in the remaining area of the input are not considered at all.

The thresholding is done using the following steps. Predetermined static thresholds t_1 and t_2 are set so that intensities less than t_1 are always black (similar to a global threshold). The subset A_{2t} of pixels in A_2 whose intensities exceed t_2 are determined. If the average intensity of pixels in A_{2t} exceeds the average intensity of pixels in A_1 (weighted by parameters t_3, t_4 and t_5) then the pixel is considered black; otherwise it is white. The algorithm is formally,

- Step 0: Check if $I(x,y) < t_1$ then $Z(x,y)$=black
- Step 1: If $I(x,y) \geq t_1$, calculate;

$$\begin{aligned} a_1 &= \text{Average of 9 pixels in area } A_1 \\ A_{2t} &= \{(x,y)|(x,y) \in A_2, I(x,y > t_2\} \\ a_2 &= \text{Average of pixels in area } A_{2t} \end{aligned} \tag{A.39}$$

- Step 2: If $(t_3 * a_2 + t_5) > (t_4 * a_1)$ set $Z(x, y)$=black otherwise set $Z(x, y)$=white

A.7 Ramesh's Method

In this technique, a functional approximation is used to calculate probability mass function consisting a two step function. The sum of square errors between the function and the histogram is minimized. Moreover, an optimal threshold is obtained iteratively.

Let the pixels in an image be represented by $L+1$ grey levels; $[0, 1, 2, ..., L]$. Let h_j denote the number of pixels with grey level j. Forming a histogram $H(x)$ of the image results in an ordered set of discrete values h_1, h_2,..., h_L. In this technique, an approximation of the set of discrete values is searched by a bi-level function $G(x)$ such that h_j, $j = 0, 1, 2, ..., L$ can be replaced by g_j, $j = 0, 1, 2, ..., L$ where $\forall_j \leq t$, $g_j = H_1$ and $\forall_j > t, g_j = H_2$. The partition point t where the approximation jumps from H_1 to H_2 provides a good threshold value. Thus all the pixels below t are mapped to one grey value whereas those above t are mapped to another value.

The error function $E(t)$ is defined as the sum of square errors;

$$E(t) = \sum_{i=0}^{t}(i - m_1(t))^2 + \sum_{i=t+1}^{L}(i - m_2(t))^2 \tag{A.40}$$

where

$$m_1(t) = \frac{\sum_{i=0}^{t} ih_i}{\sum_{i=0}^{t} h_i} \quad m_2(t) = \frac{\sum_{i=t+1}^{L} ih_i}{\sum_{i=t+1}^{L} h_i} \tag{A.41}$$

N_1 is the total number of pixels with grey values *below* or equal to t value and N_2 is the totalnumber of pixels with grey values greater than t. In order to minimise the sum of square errors between the grey values and the mean value, in the two regions, the following expression is calculated;

$$minE(t) = minE_1(t) + E_2(t) \tag{A.42}$$

$$E_1(t) = \int_0^t (x - m_1(t))^2 p(x) N dx \quad E_2(t) = \int_t^L (x - m_2(t))^2 p(x) N dx \tag{A.43}$$

and p(x), the probability density function is defined as

$$p(x) \cong \frac{h(x)}{N} N \cong \int_0^L h(x) dx \tag{A.44}$$

Thus,

$$\begin{aligned} p(x) &\cong \tfrac{h(x)}{N} N \cong \textstyle\int_0^L h(x) dx \\ m_1 &= \frac{\int_0^t x p(x) dx}{\int_0^t p(x) dx} = \frac{B}{A} \\ m_2 &= \frac{\int_t^L x p(x) dx}{\int_t^L p(x) dx} = \frac{D}{C} \end{aligned} \tag{A.45}$$

So;

$$\begin{aligned} E(t) = \quad & N \textstyle\int_0^t (x^2 - 2m_1(t)x + m_1^2(t)) p(x) dx + N \int_t^L (x^2 - 2m_2(t)x + m_2^2(t)) p(x) dx \\ \tfrac{E(t)}{N} = \quad & \textstyle\int_0^t x^2 p(x) dx - 2m_1(t) \int_0^t x p(x) dx + m_1^2(t) \int_0^t p(x) dx + \int_t^L x^2 p(x) dx \\ & -2m_2(t) \textstyle\int_t^L x p(x) dx + m_2^2(t) \int_t^L p(x) dx \end{aligned} \tag{A.46}$$

To find the threshold t that minimizes $E(t)$, the differentiation of $E(t)$ through t is calculated;

$$\begin{aligned} \tfrac{\partial E(t)}{\partial t} &= 0 \\ \tfrac{1}{N} \tfrac{\partial E(t)}{\partial t} = \quad & t^2 p(t) - 2(\tfrac{\partial m_1(t)}{\partial t} \textstyle\int_0^t x p(x) dx - 2m_1(t) t p(t) \\ & +2m_1(t) \tfrac{\partial m_1(t)}{\partial t} \textstyle\int_0^t p(x) dx + m_1^2(t) p(t) \\ & -t^2 p(t) - 2 \tfrac{\partial m_2(t)}{\partial t} \textstyle\int_0^t x p(x) dx + 2m_2(t) t p(t) \\ & 2m_2(t) \tfrac{\partial m_2(t)}{\partial t} \textstyle\int_t^L p(x) dx - m_2^2(t) p(t) \end{aligned} \tag{A.47}$$

The second, fourth, seventh and ninth terms reduce to zero

$$\begin{aligned} & -2 \tfrac{\partial m_1}{\partial t} \textstyle\int_0^t x p(x) dx + 2m_1 \tfrac{\partial m_1}{\partial t} \int_0^t p(x) dx \\ & = -2 \tfrac{tp(t)A - p(t)B}{A^2} B + 2m_1(t) \tfrac{tp(t)A - p(t)B}{A^2} A \\ & = -2(tp(t)m_1(t) - p(t)m_1^2(t)) + 2m_1(t) t p(t) - p(t) m_1(t) \\ & = 0 \end{aligned} \tag{A.48}$$

Thus the dependecy of $m_1(t)$ and $m_2(t)$ on t is effectively removed and;

$$\frac{\partial E_1(t)}{\partial t} = (t - m_1(t)^2)p(t)N \tag{A.49}$$

and

$$\begin{aligned} \tfrac{\partial E_2(t)}{\partial t} &= -(t - m_2(t)^2)p(t)N \\ \Rightarrow \tfrac{1}{N}\tfrac{\partial E(t)}{\partial t} &= p(t)[m_1^2(t) - m_2^2(t) + 2m_2(t)t - 2m_1(t)t] \\ &= 0 \\ \Rightarrow t &= \tfrac{m_1(t)+m_2(t)}{2} \end{aligned} \tag{A.50}$$

A.8 Rosenfeld's Method

In this method the optimal threshold value is selected through the shape of the histogram. Let a gray scale image be represented by gray levels $[K...L]$ and H is the histogram of the image. For all gray scale values $[K...L]$, $[h(K)...h(L)]$ corresponds to the respective values in H. The histogram is considered as a two dimensional bounded region.

Firstly, a convex hull is constructed through H to overcome the concavities of H. This is the smallest convex polygon $\overline{H}$ containing H and the concavities are found by taking the difference $\overline{H} - H$. Secondly, it is remarked that the three straight lines that bound H on the left, right and the bottom are sides of $\overline{H}$. Therefore, it is only required to construct the part of $\overline{H}$ which is defined as the tops of the values on H.

A basic algorithm to construct $\overline{H}$ is as follows;

1. Start at $(K, h(K))$, compute the slopes θ_i of the line segments $\overline{(K, h(K))(i, h(i))}$, $K + 1 \leq i \leq L$ where $-90 < \theta_i < 90$.

2. Let θK_1 be the largest of these slopes and let K_1 be the rightmost point having this slope.

3. Determine $\overline{(K, h(K))(K_1, h(K_1))}$ the side of the convex hull.

4. Repeat the process with K_1 by replacing K until L:

   Compute the slopes of the segments $(K_1, h(K_1))(i, h(i)) \quad K_1 + 1 \leq i \leq L$,

   Find the largest slope θ_{K_2} and the rightmost point K_2 having this slope, yielding $\overline{(K_1, h(K_1))(K_2, h(K_2))}$ as a side of the convex hull.

Whenever H lies strictly below $\overline{H}$, a concavity in H is obtained.

Even any concavity in the histogram would be a possible location for a threshold, it should be noted that not all points of the concavity are equally feasible candidates. In order to resolve this problem a deepest concavity problem must be taken into account.

Let $\overline{h(i)}$ be the height of $\overline{H}$ at gray level i. Thus $\overline{h(i)} - h(i)$ is the vertical distance between the top at the value $h(i)$ and the border of $\bar{(}H)$. The candidates will be determined as threshold levels i when $\overline{h(i)} - h(i)$ would be a local maximum. These points are denoted as deepest concavity points and are selected as optimal threshold points.

A.9 Yen's Method

Yen et al. [183] developed a thresholding method by considering the discrepancy between the thresholded and original images. The discrepancy is defined as a cost function based on the maximum correlation criterion. By the minimization of the cost function, an automatic threshold value is determined and gray levels are classified.

Let $f(x, y)$ is an image of size $N \times N$ pixels which are represented by m gray levels. Let $G_m = 0, 1, ..., (m-1)$ denote the set of gray-levels and $f_i, i \in G_m$ be the observed gray-level frequencies of the image f. The probability of the gray-level i in

the image f can be calculated as;

$$p_i = \frac{f_i}{n \times N}, i \in G_m \tag{A.51}$$

For a given gray-level s if $\sum_{t=0}^{s-1} p_i$ is larger than zero and smaller than one,the following distributions would be derived

$$\begin{aligned} A &\equiv \left\{ \frac{p_0}{P(s)}, \frac{p_1}{P(s)}, ..., \frac{p_{s-1}}{P(s)} \right\} \\ B &\equiv \left\{ \frac{p_s}{1-P(s)}, \frac{p_{s+1}}{1-P(s)}, ..., \frac{p_{m-1}}{1-P(s)} \right\} \end{aligned} \tag{A.52}$$

where $P(s) = \sum_{i=0}^{s-1} p_i$ is the total probability up to (s-1)th gray level. In the maximum entropy criterion, the threshold is chosen as the maximization of the total amount of information between input and thresholded image. Thus, the total information provided by A and B;

$$\begin{aligned} TE(S) &= E_A(S) + E_B(S) \\ &= -\sum_{i=0}^{s-1}(\frac{p_i}{P(s)})ln(\frac{p_i}{P(s)}) - \sum_{i=s}^{m-1}(\frac{p_i}{1-P(s)})ln(\frac{p_i}{1-P(s)}) \\ &= ln[P(s)(1-P(s))] - H(s)/P(s) - H'(s)/(1-P(s)) \end{aligned} \tag{A.53}$$

where $P(s) = \sum_{i=0}^{s-1} p_i$, $H(s) = -\sum_{i=0}^{s-1} p_i \times ln(p_i)$ and $H'(s) = -\sum_{i=s}^{m-1} p_i \times ln(p_i)$.

The maximum entropy criterion is to determine the threshold s^* such that

$$TE(s^*) = \max_{s \in G_m} TE(s) \tag{A.54}$$

In order to calculate this threshold, it is proposed to use the total amount of correlation provided by distributions;

$$\begin{aligned} TC(s) &= C_A(s) + C_B(s) \\ &= -ln\sum_{i=0}^{s-1}(\frac{p_i}{P(s)})^2 - ln\sum_{i=s}^{m-1}(\frac{p_i}{1-P(s)})^2 \\ &= -ln[G(s) \times G'(s)]/[P^2(s) \times (1-P(s))^2] \\ &= -ln[G(s) \times G'(s)] + 2ln[P(s) \times (1-P(s))] \end{aligned} \tag{A.55}$$

where $G(s) = \sum_{i=0}^{s-1} p_i^2$, $G'(s) = \sum_{i=s}^{m-1} p_i^2$ and the correlation of a random variable $C(X) = -ln\sum_{i \geq 0} p_i^2$. In order to obtain the maximal correlation contributed by the

object and the background, $TC(s)$ must be maximized. The maximum correlation criterion is to determine the threshold s^* such that;

$$TC(s^*) = \max_{s \in G_m} TC(s) \tag{A.56}$$

In order to quantify this maximization, the discrepancy between the thresholded and original images should be calculated and the following terms are introduced for a given distribution $P \equiv \{p_i | i \in G_m\}$;

- k: the classification number that the gray levels are classified,
- $s_{k,i}$: the i-th non-zero threshold when the gray levels are classified into k classes,
- $C_{k,i}$: the i-th class among these k classes with gray levels from $s_{k,i-1}$ to $s_{k,i} - 1$,
- $\omega_{k,i}$: the probability of the class $C_{k,i}$,

$$\omega_{k,i} = Prob(C_{k,i}) = \sum_{j=s_{k,i-1}}^{s_{k,i}-1} p_j \tag{A.57}$$

- $P_{k,i}$: the distribution derived from $C_{k,i}$ after the normalization by $\omega_{k,i}$,

$$P_{k,i} = \{p_j/\omega_{k,i} | j \in G_{s_{k,i}}\} \tag{A.58}$$

- $\mu_{k,i}$: the mean of $P_{k,i}$

$$\mu_{k,i} = \sum_{j=s_{k,i-1}}^{s_{k,i}-1} j \times Prob(j|C_{k,i}) \tag{A.59}$$

- $\sigma_{k,i}^2$: the variance of $P_{k,i}$

$$\begin{aligned} \sigma_{k,i}^2 &= \textstyle\sum_{j=s_{k,i-1}}^{s_{k,i}-1} (j - \mu_{k,i})^2 \times Prob(j|C_{k,i}) \\ &= \textstyle\sum_{j=s_{k,i-1}}^{s_{k,i}-1} (j - \mu_{k,i})^2 \times p_j/\omega_{k,i} \end{aligned} \tag{A.60}$$

where $G_{s_{k,i}} \equiv s_{k,i-1}, s_{k,i-1} + 1, ..., s_{k,i} - 1$. In each class, all gray levels are designated to the mean value of the gray levels in that class. The discrepancy $Dis(k)$ is defined

as follows;

$$\begin{aligned} Dis(k) &= \sum_{j=1}^{k} Prob(C_{k,j}) \times \sigma_{k,j}^2 \\ &= \sum_{i=0}^{s_{k,1}-1}(i-\mu_{k,1})^2 \times p_i + \sum_{i=s_{k,1}}^{s_{k,2}-1}(i-\mu_{k,2})^2 \times p_i \\ &\quad +\ldots+ \sum_{i=s_{k,k-1}}^{m-1}(i-\mu_{k,k})^2 \times p_i \end{aligned} \tag{A.61}$$

APPENDIX B. LIST OF THE PUBLICATIONS PRODUCED OUT OF THE PHD STUDY

1. Ismail Burak Parlak, Salih Murat Egi, Ahmet Ademoğlu, Peter Germonpré, Özlem Batukan Esen, Costantino Balestra, Alessandro Marroni, Bubble stream reveals functionality of the right-to-left shunt: Detection of a silent source for air embolism, *accepted for publication in* Journal of Ultrasound in Medicine and Biology, 2013.

2. Ismail Burak Parlak, Ahmet Ademoğlu, Salih Murat Egi, Peter Germonpré, Costantino Balestra, Alessandro Marroni, Detection of Post-Decompression Microemboli: Quantitative and Qualitative Approaches, *submitted to* Journal of Undersea and Hyperbaric Medicine, 2013.

3. Ismail Burak Parlak, Salih Murat Egi, Ahmet Ademoğlu, Peter Germonpré, Alessandro Marroni, Costantino Balestra, Salih Aydın, Computerized methods for the diagnosis of microemboli related to the decompression sickness (in Turkish), Sualtı Bilim ve Teknoloji Toplantısı-SBT, 2012.

4. Ismail Burak Parlak, Ahmet Ademoğlu, Salih Murat Egi, Costantino Balestra, Peter Germonpré, Alessandro Marroni, Automatic bubble detection in cardiac video imaging, POLIBITS, vol:44, pp:5-10, 2011 (ISSN: 1870-9044).

5. Ismail Burak Parlak, Salih Murat Egi, Ahmet Ademoğlu, Costantino Balestra, Peter Germonpré, Alessandro Marroni, Intelligent bubble recognition on cardiac videos using Gabor wavelet, International Journal of Digital Information and Wireless Communications (IJDIWC) Vol:1:1 pp: 195-203, 2011 (ISSN: 2225-658X).

6. Ismail Burak Parlak, Salih Murat Egi, Ahmet Ademoğlu, Costantino Balestra, Peter Germonpré, Alessandro Marroni, Salih Aydın, A neuro-fuzzy approach of bubble recognition in cardiac video processing: in Book of Springer in CIS, Vol:166, Part 2, pp:277-286, DOI: 10.1007/978-3-642-21984-924.

7. Ismail Burak Parlak, Salih Murat Egi, Ahmet Ademoğlu, Costantino Balestra, Peter Germonpré, Alessandro Marroni, Automatic bubble detection in cardiac video imaging, MICAI 2011.

8. Ismail Burak Parlak, Salih Murat Egi, Ahmet Ademoğlu, Costantino Balestra, Peter Germonpré, Alessandro Marroni, Salih Aydın, A neuro-fuzzy approach of bubble recognition in cardiac video processing, DICTAP 2011.

9. Ismail Burak Parlak, Salih Murat Egi, Ahmet Ademoğlu, Costantino Balestra, Peter Germonpré, Alessandro Marroni, Salih Aydın, Automatic analysis for bubble detection on decompression records, Annual Meeting of the European Underwater and Barometrical Society, EUBS 2010.

10. Ismail Burak Parlak, Salih Murat Egi, Ahmet Ademoğlu, Costantino Balestra, Peter Germonpré, Alessandro Marroni, Salih Aydın, Automatic bubble detection with neural networks on post decompression frames (in Turkish), Biyomedikal Mühendisliği Ulusal Toplantısı- BIYOMUT-2010.

11. Ismail Burak Parlak, Salih Murat Egi, Ahmet Ademoğlu, Peter Germonpré, Özlem Batukan Esen, Salih Aydın, Serap Tekin, Costantino Balestra, Alessandro Marroni, Bubble detection for automatic evaluation of patent foramen ovale (PFO), 3rd International Symposium on Underwater Research-EMU2009.

12. Ismail Burak Parlak, Salih Murat Egi, Ahmet Ademoğlu, Peter Germonpré, Özlem Batukan Esen, Salih Aydın, Serap Tekin, Costantino Balestra ,Alessandro Marroni, Automatic bubble counting and the identification of the left atrium area in ultrasound images for objective assessment of patency in cardiac foramen ovale, Undersea and Hyperbaric Medicine Annual Scientific Meeting UHMS-2009.

13. Ismail Burak Parlak, Salih Murat Egi, Ahmet Ademoğlu, Peter Germonpré, Özlem Batukan Esen, Salih Aydın, Serap Tekin, Costantino Balestra ,Alessandro Marroni, Bubble detection on left atrium related to patent foramen ovale (in Turkish), Biyomedikal Mühendisliği Ulusal Toplantısı-BIYOMUT-2009.

REFERENCES

1. Vinci, L. D., *Leonardo on the human body*, New York, USA: Dover Publications, 1953.

2. Hara, H., R. Virmani, E. Ladich, S. Mackey-Bojack, J. Titus, M. Reisman, W. Gray, M. Nakamura, M. Mooney, A. Poulose, and R. S. Schwartz, "Patent foramen ovale: current pathology,pathophysiology, and clinical status," *Journal of the American College of Cardiology*, Vol. 46, pp. 1768–1776, Nov 2005.

3. Soliman, O. I. I., M. L. Geleijnse, F. J. Meijboom, A. Nemes, O. Kamp, P. Nihoyannopoulos, N. Masani, S. B. Feinstein, and F. J. T. Cate, "The use of contrast echocardiography for the detection of cardiac shunts," *European Journal of Echocardiography*, Vol. 16, pp. 21–30, Nov 2002.

4. Buck, T., M. J. Monaghan, and A. Franke, *Three-dimensional Echocardiography*, Springer Verlag, 2011.

5. Eftedal, O., and A. O. Brubakk, "Detecting intravascular gas bubbles in ultrasonic images," *Medical & Biological Engineering & Computing*, Vol. 31, pp. 627–633, Nov 1993.

6. Hein, R., Y. Bayard, M. Taaffe, F. Buscheck, S. Ostermayer, K. Billinger, M. Reschke, T. Trepels, H. Lissmann-Jensen, K. Lang, A. Romer, N. Wilson, and H. Sievert, "Patent foramen ovale and left atrial appendage: New devices and methods for closure," *Pediatric Cardiology*, Vol. 26, pp. 234–240, May-Jun 2005.

7. Prisk, G. K., M. Paiva, and J. B. West, *Gravity and the lung lessons from microgravity*, Karachi, Pakistan: Informa Healthcare, 1st ed., 2001.

8. Honkanen, M., P. Saarenrinne, T. Stoor, and J. Niinimaki, "Recognition of highly overlapping ellipse-like bubble images," *Measurement Science & Technology*, Vol. 16, pp. 1760–1770, Jul 2005.

9. Beghdadi, A., A. L. Negrate, and P. V. D. Lesegno, "Entropic thresholding using a block source model," *Graphical Models in Image Processing*, Vol. 57, pp. 197–205, May 1995.

10. Palumbo, P. W., P. Swaminathan, and S. N. Srihari, "Document image binarization: Evaluation of algorithms," in *SPIE Conference on Applications of Digital Image Processing*, (San Diego, CA–USA), pp. 278–285, SPIE, Aug 1986.

11. Baars, H. F., I. C. Joziasse, and J. W. Roos-Hesselink, *Clinical cardiogenetics*, London,UK: Springer-Verlag, 1st ed., 2011.

12. Rashkind, W. J., "Pediatric cardiology: A brief historical perspective," *Pediatric Cardiology*, Vol. 1, no. 1, pp. 63–71, 1979.

13. Perloff, J. K., *Clinical Recognition of Congenital Heart Disease,*, Philadelphia, Pennsylvania: Saunders, 5e ed., 2003.

14. Fransson, S. G., "The botallo mystery," *Clinical Cardiology*, Vol. 22, pp. 434–436, Jun 1999.

15. Said, H. M., *Greco-Arab concepts on cardiovascular diseases*, Karachi, Pakistan: Hamdard Foundation Press, 2nd ed., 1983.

16. Ihsanoglu, E., R. Sesen, M. S. Bekar, G. Gunduz, and V. Bulut, *History of the literature of medical sciences during the ottoman period*, Istanbul, Turkey: IRCICA, 1st ed., 2008.

17. Slater, J., and M. Fisch, "Percutaneous treatment of congenital defects of the inter-atrial septum in adults - recent advances and persistent pitfalls," *Interventional Cardiology*, Vol. 4, no. 1, pp. 76–80, 2009.

18. Kilgour, F. G., "William harvey and his contributions," *Circulation*, Vol. 23, pp. 286–296, Feb 1961.

19. Rokitansky, K., *Die defecte der scheidewande des herzens*, Wien: Braumuller, 1875.

20. Salle, V., "Grosse der extremitaten mit einem an akromegalie erinnernden symptomenkomplex," *J Kinderheilk*, Vol. 75, pp. 540–541, 1912.

21. Assman, H., *Die klinische roentgendiagnostik der innern erkrankungen*, Leipzig: Vogel, 1921.

22. Bedford, D. E., C. Papp, and J. Parkinson, "Atrial septal defect," *British Heart Journal*, Vol. 3, pp. 37–68, Jan 1941.

23. Hudson, R., "The normal and abnormal inter-atrial septum," *British Heart Journal*, Vol. 17, pp. 489–495, Oct 1941.

24. Sweeney, L. J., and G. C. Rosenquist, "The normal anatomy of the atrial septum in the human heart," *American Heart Journal*, Vol. 98, pp. 194–199, Aug 1979.

25. Hanley, P. C., T. A. Jamil, J. K. Hynes, W. D. Edwards, G. S. Reeder, D. J. Hagler, and J. B. Seward, "Diagnosis and classification of atrial septal aneurysm by two-dimensional echocardiography: report of 80 consecutive cases," *Journal of the American College of Cardiology*, Vol. 6, pp. 1370–1382, Dec 1985.

26. Schwinger, M. E., A. J. Gindea, R. S. Freedberg, and I. Kronzon, "The anatomy of the interatrial septum : a transesephageal echocardiographic study," *The American Heart Journal*, Vol. 119, pp. 1401–1405, Jun 1990.

27. Filaire, M., O. Nohra, L. Sakka, J. B. Chadeyras, V. D. Costa, A. Naamee, P. Bailly, and G. Escande, "Anatomical bases of the surgical dissection of the interatrial septum : a morphological and histological study," *Surgical and Radiologic anatomy*, Vol. 30, pp. 369–373, Jun 2008.

28. Balestra, C., F. R. Cronjé, P. Germonpré, and A. Marroni, *PFO & The Diver*, Best Publishing Company, 2007.

29. Lang, F. J., and A. Posselt, "Aneurysmatische vorwolbung der fossa ovalis in den linken vorhof," *Wien Med Wochenschr*, Vol. 84, pp. 392–395, 1934.

30. Corno, A. F., and P. Festa, *Congenital heart defects decision making for cardiac surgery volume 3 CT-Scan and MRI*, Germany: Steinkopff Verlag Springer, 2nd ed., 2009.

31. Popelova, J., E. Oechslin, H. Kaemmerer, M. G. Sutton, and P. Zacek, *Congenital heart disease in adults*, United Kingdom: Informa Healthcare, 2nd ed., 2008.

32. Ferencz, C., C. Loffredo, A. C. Villasenor, and P. D. Wilson, *Genetic and environmental risk factors of major cardiovascular malformations: The Baltimore-Washington infant study: 1981-1989*, New York, USA: Futura Publishing, 1st ed., 1997.

33. Foster, P. P., A. M. Boriek, B. B. Butler, M. L. Gernhardt, and A. A. Bove, "Patent foramen ovale and paradoxical systemic embolism: a bibliographic review," *Aviation, Space and Environmental Medicine*, Vol. 74, pp. 1–64, Jun 2003.

34. Schneider, B., T. Zienkiewicz, V. Jansen, T. Hofmann, H. Noltenius, and T. Meinertz, "Diagnosis of patent foramen ovale by transesophageal echocardiography and correlation with autopsy findings," *American Journal of Cardiology*, Vol. 77, pp. 1202–1209, Jun 1996.

35. Woods, T. D., L. Harmann, T. Purath, S. Ramamurthy, S. Subramanian, S. Jackson, and S. Tarima, "Small- and moderate-size right-to-left shunts identified by saline contrast echocardiography are normal and unrelated to migraine headache," *Chest*, Vol. 138, pp. 264–269, Aug 2010.

36. Marriott, K., V. Manins, A. Forshaw, J. Wright, and R. Pascoe, "Detection of right-to-left atrial communication using agitated saline contrast imaging: experience with 1162 patients and recommendations for echocardiography," *Journal of the American Society of Echocardiography*, Vol. 26, pp. 96–102, Jan 2013.

37. Litwin, S. B., *Color Atlas of Congenital Heart Surgery*, USA: Springer, 2nd ed., 2007.

38. Meissner, I., B. K. Khandheria, J. A. Heit, G. W. Petty, S. G. Sheps, G. L. Schwartz, J. P. Whisnant, D. O. Wiebers, J. L. Covalt, T. M. Petterson, T. J. H. Christianson, and Y. Agmon, "Patent foramen ovale: Innocent or guilty? : Evidence from a prospective population-based study," *Journal of the American College of Cardiology*, Vol. 47, pp. 440–445, Jan 2006.

39. Meier, B., "Patent foramen ovale: beauty spot or health threat?," *Cardiology Rounds*, Vol. 5, pp. 1–8, Dec 2001.

40. Saary, M. J., and G. W. Gray, "The possible relationship between patent foramen ovale and decompression sickness: A review of the literature," print, Defence and Civil Institute of Environmental Medicine, DCIEM TR 1999-001, 1999.

41. Drighil, A., H. E. Mosalami, N. Elbadaoui, S. Chraibi, and A. Bennis, "Patent foramen ovale: A new disease?," *International Journal of Cardiology*, Vol. 122, pp. 1–9, Oct 2007.

42. Hagen, P. T., D. G. Scholz, and W. D. Edwards, "Incidence and size of patent foramen ovale during the first 10 decades of life: an autopsy study of 965 normal hearts," *Mayo Clinic Proceedings*, Vol. 59, pp. 17–20, Jan 1984.

43. Penther, P., "Patent foramen ovale: an anatomic study of 500 consecutive autopsies," *Archives des Maladies du Coeur et des Vaisseaux*, Vol. 87, pp. 15–21, Jan 1994.

44. Arquizan, C., J. Coste, P. J. Touboul, and J. L. Mas, "Is patent foramen ovale a family trait? a transcranial doppler sonographic study," *Stroke*, Vol. 32, pp. 1563–1566, Jul 2001.

45. Posch, M. G., M. Gramlich, M. Sunde, K. R. Schmitt, S. H. Y. Lee, S. Richter, A. Kersten, A. Perrot, I. H. A. K. A N Panek, G. Nemer, A. Megarbane, R. Dietz, B. Stiller, F. Berger, R. P. Harvey, and C. Ozcelik, "A gain-of-function tbx20 mutation causes congenital atrial septal defects, patent foramen ovale and cardiac valve defects," *Journal of Medical Genetics*, Vol. 47, pp. 230–235, Jul 2010.

46. Biben, C., R. Weber, S. Kesteven, E. Stanley, L. McDonald, D. A. Elliott, L. Barnett, F. Köentgen, L. Robb, M. Feneley, and R. P. Harvey, "Cardiac septal and valvular dysmorphogenesis in mice heterozygous for mutations in the homeobox gene nkx2-5," *Circulation Research*, Vol. 87, pp. 888–895, Nov 2000.

47. Kaltenbrun, E., P. Tandon, N. M. Amin, L. Waldron, C. Showell, and F. L. Conlon, "Xenopus: An emerging model for studying congenital heart disease," *Circulation Research*, Vol. 91, pp. 495–510, Jun 2011.

48. Wessels, M. W., and P. J. Willems, "Genetic factors in non-syndromic congenital heart malformations," *Circulation Research*, Vol. 78, pp. 103–123, Aug 2010.

49. Shen, T., I. Aneas, N. Sakabe, R. J. Dirschinger, G. Wang, S. Smemo, J. M. Westlund, H. Cheng, N. Dalton, Y. Gu, C. J. Boogerd, C. Ca, K. Peterson, J. Chen, M. A. Nobrega, and S. M. Evans, "Tbx20 regulates a genetic program essential to adult mouse cardiomyocyte function," *The Journal of Clinical Investigation*, Vol. 121, pp. 4640–4654, Dec 2011.

50. Cresci, M., I. Foffa, L. Ait-Ali, S. Pulignani, E. A. Gianicolo, N. Botto, E. Picano, and M. G. Andreassi, "Maternal and paternal environmental risk factors, metabolizing gstm1 and gstt1 polymorphisms, and congenital heart disease," *The American Journal of Cardiology*, Vol. 108, pp. 1625–1631, Dec 2011.

51. Germonpré, P., F. Hastir, P. Dendale, A. Marroni, A. F. Nguyen, and C. Balestra, "Evidence for increasing patency of the foramen ovale in divers," *American Journal of Cardiology*, Vol. 95, pp. 912–915, Apr 2005.

52. Conheim, J., *Thrombose und Embolie: Vorlesung uber allgemeine Pathologie*, Berlin, Germany: Hirschwald Verlag, 1877.

53. Cabanes, L., J. L. Mas, A. Cohen, P. Amarenco, P. A. Cabanes, P. Oubary, F. Chedru, F. Guerin, M. G. Bousser, and J. D. Recondo, "Atrial septal aneurysm and patent foramen ovale as risk factors for cryptogenic stroke in patients less than 55 years of age. a study using transesophageal echocardiography," *Stroke*, Vol. 24, pp. 1865–1873, Dec 1993.

54. Barratt, M. R., and S. L. Pool, *Principles of clinical medicine for space flight*, New York,USA: Springer-Verlag, 1st ed., 2008.

55. Germonpré, P., P. Dendale, P. Unger, and C. Balestra, "Patent foramen ovale and decompression sickness in sports divers," *Journal of Applied Physiology*, Vol. 84, pp. 1622–1626, May 1998.

56. Stone, D. A., J. Godard, and M. C. C. and, "Patent foramen ovale: association between the degree of shunt by contrast transesophageal echocardiography and the risk of future ischemic neurologic events," *American Heart Journal*, Vol. 131, pp. 158–161, Jan 1996.

57. Homma, S., M. R. D. Tullio, R. L. Sacco, D. Mihalatos, G. L. Mandri, and J. P. Mohr, "Characteristics of patent foramen ovale associated with cryptogenic stroke. a biplane transesophageal echocardiographic study," *Stroke*, Vol. 25, pp. 582–586, Mar 1994.

58. Germonpre, P., "Patent foramen ovale and diving," *Cardiology Clinics*, Vol. 23, pp. 97–104, Feb 2005.

59. Moon, R. E., E. M. Camporesi, and J. A. Kisslo, "Patent foramen ovale and decompression sickness in divers," *Lancet*, Vol. 333, pp. 513–514, Mar 1989.

60. Torti, S. R., M. Billinger, M. Schwerzmann, R. Vogel, R. Zbinden, and S. Windecker, "Risk of decompression illness among 230 divers in relation to the presence and size of patent foramen ovale," *European Heart Journal*, Vol. 25, pp. 1014–1020, Jun 2004.

61. Waligora, J. M., M. R. Powell, W. T. Norfleet, M. Wood, and D. Martin, "The incidence of patent foramen ovale and serious symptoms of decompression sickness in trials conducted to develop operational decompression prevention protocols for space flight," print, NASA, TM2003212052, 1999.

62. Bigal, M. E., and R. B. Lipton, "The epidemiology, burden, and comorbidities of migraine," *Neurologic Clinics*, Vol. 27, pp. 321–334, May 2009.

63. Sarisoy, S., *Migraine in children and prevalence of right-to-left shunt(in turkish)*. PhD thesis, Ondokuz Mayis University, Samsun, Turkey, 2009.

64. Anzola, G. P., M. Magoni, M. Guindani, L. Rozzini, and G. D. Volta, "Potential source of cerebral embolism in migraine with aura: A transcranial doppler study," *Neurology*, Vol. 52, pp. 1622–1625, May 1999.

65. Etminan, M., B. Takkouche, F. C. Isorna, and A. Samii, "Risk of ischaemic stroke in people with migraine: systematic review and metaanalysis of observational studies," *British Medical Journal*, Vol. 330, pp. 63–65, Jan 2005.

66. Stang, P. E., A. P. Carson, K. M. Rose, J. Mo, S. A. Ephross, E. Shahar, and M. Szklo, "Headache, cerebrovascular symptoms, and stroke: the atherosclerosis risk in communities study," *Neurology*, Vol. 64, pp. 1573–1577, May 2005.

67. Kurth, T., M. A. Slomke, C. S. Kase, N. R. Cook, I. M. Lee, J. M. Gaziano, H. C. Diener, and J. E. Buring, "Migraine, headache, and the risk of stroke in women: a prospective study," *Neurology*, Vol. 64, pp. 1020–1026, Mar 2005.

68. Giardini, A., A. Donti, R. Formigari, L. Salomone, D. Prandstraller, M. Bonvicini, G. Palareti, D. Guidetti, O. Gaddi, and F. M. Picchio, "Transcatheter patent foramen ovale closure mitigates aura migraine headache abolishing spontaneous right-to-left shunting," *The American Heart Journal*, Vol. 151, pp. 922.e1–922.e5, Apr 2006.

69. Gladstein, J., E. W. Holden, L. Peralta, and M. Raven, "Diagnosis and symptom patterns in children presenting to a pediatric headache clinic," *Headache*, Vol. 33, pp. 497–500, Oct 1993.

70. Godart, F., C. Rey, A. Prat, A. Vincentelli, A. Chmait, C. Francart, and H. Porte, "Atrial right-to-left shunting causing severe hypoxemia despite normal right-sided pressures:report of 11 consecutive cases corrected by percutaneous closure," *European Heart Journal*, Vol. 21, pp. 483–489, Mar 2000.

71. Kruit, M. C., M. A. V. Buchem, P. A. Hofman, T. N. B. Jacobus, M. T. Gisela, M. D. Ferrari, and J. L. Lenore, "Migraine as a risk factor for subclinical brain lesions," *The Journal of the American Medical Association*, Vol. 291, pp. 427–434, Jan 2004.

72. Woods, R. P., M. Iacoboni, and J. C. Mazziotta, "Brief report: Bilateral spreading cerebral hypoperfusion during spontaneous migraine headache," *The New England Journal of Medicine*, Vol. 331, pp. 1689–1692, Dec 1994.

73. Sztajzel, R., D. Genoud, S. Roth, B. Mermillod, and J. L. Floch-Rohr, "Patent foramen ovale, a possible cause of symptomatic migraine: A study of 74 patients with acute ischemic stroke," *Cerebrovascular Diseases*, Vol. 13, no. 2, pp. 102–106, 2002.

74. Carod-Artal, F. J., R. B. da Silveira, H. Braga, W. Kummer, H. M. Mesquita, and A. P. Vargas, "Prevalance of patent foramen ovale in migraine patients with and without aura compared with stroke patients. a transcranial doppler study," *Cephalalgia*, Vol. 26, pp. 934–939, Aug 2006.

75. Bateman, D. N., "Triptans and migraine," *Lancet*, Vol. 355, pp. 860–861, Mar 2000.

76. Wilmshurst, P., M. J. Pearson, S. Nightingale, K. P. Walsh, and W. L. Morrison, "Inheritance of persistent foramen ovale and atrial septal defects and the relation to familial migraine with aura," *Heart*, Vol. 90, pp. 1315–1320, Nov 2004.

77. Raymond-Martimbeau, P., "Transient adverse events positively associated with patent foramen ovale after ultrasound guided foam sclerotherapy," *Phlebology*, Vol. 24, pp. 114–119, Jun 2009.

78. Hacievliyagil, S. S., H. Gunen, F. M. Kosar, I. Sahin, and T. Kilic, "Prevalence and clinical significance of a patent foramen ovale in patients with chronic obstructive pulmonary disease," *Respiratory Medicine*, Vol. 100, pp. 903–910, Oct 2006.

79. Yalonetsky, S., A. B. Nun, Y. Shwartz, and A. Lorber, "Transcatheter closure of a patent foramen ovale prior to a pneumonectomy to prevent platypnea syndrome," *European Journal of CardioThoracic Surgery*, Vol. 29, pp. 622–624, Apr 2006.

80. Hashimoto, Y., T. Terasaki, Y. Hara, N. Furuyoshi, and M. Uchino, "Etiological studies on 17 cases of retinal artery occlusion and 16 cases of amaurosis fugax," *Rinsho Shinkeigaku*, Vol. 38, pp. 219–223, Mar 1998.

81. Nakagawa, T., A. Hirata, N. Inoue, Y. Hashimoto, and H. Tanihara, "A case of bilateral central retinal artery obstruction with patent foramen ovale," *Acta Ophthalmologica Scandinavica*, Vol. 82, pp. 111–112, Feb 2004.

82. Gabrielian, A., W. F. Mieler, and S. M. Hariprasad, "Retinal artery occlusion associated with a patent foramen ovale," *Eye*, Vol. 24, pp. 396–397, Feb 2010.

83. Wada, Y., R. Takahashi, C. Yanagihara, and Y. Nishimura, "Paradoxical cerebral embolism as the initial symptom in a patient with ovarian cancer," *Journal of Stroke and Cerebrovascular Diseases*, Vol. 16, pp. 88–90, Mar-Apr 2007.

84. Klingmann, C., P. J. Benton, P. A. Ringleb, and M. Knauth, "Embolic inner ear decompression illness: correlation with a right-to-left shunt," *Laryngoscope*, Vol. 113, pp. 1356–1361, Aug 2003.

85. Iguchi, Y., K. Kimura, K. Kobayashi, T. Tachi, T. Aihara, and T. Harada, "Sudden deafness and right-to-left shunts," *Cerebrovascular Diseases*, Vol. 26, pp. 409–412, Aug 2008.

86. Blatteau, J. E., J. B. Souraud, E. Gempp, and A. Boussugues, "Gas nuclei, their origin, and their role in bubble formation," *Aviation, Space and Environmental Medicine*, Vol. 77, pp. 1068–1076, Oct 2006.

87. Oakley, C., S. Taylor, D. Wilcken, A. Hollman, J. F. Goodwin, and J. Shillingford, "Dye dilution curves in congenital heart disease," *British Heart Journal*, Vol. 22, pp. 533–545, Sep 1960.

88. Karttunen, V., M. Ventila, M. Hillbom, O. Salonen, H. Haapaniemi, and M. Kaste, "Dye dilution and oximetry for detection of patent foramen ovale," *Acta Neurologica Scandinavica*, Vol. 97, pp. 231–236, Apr 1998.

89. Karttunen, V., M. Ventila, M. Ikaheimo, M. Niemela, and M. Hillbom, "Ear oximetry: a noninvasive method for detection of patent foramen ovale," *Stroke*, Vol. 32, pp. 448–453, Feb 2001.

90. Rubissow, G. J., and R. S. Mackay, "Ultrasonic imaging of in vivo bubbles in decompression sickness," *Ultrasonics*, Vol. 9, pp. 225–234, Oct 1971.

91. Tufan, K., A. Ademoglu, E. Kurtaran, G. Yildiz, S. Aydin, and S. M. Egi, "Automatic detection of bubbles in the subclavian vein using doppler ultrasound signals," *Aviation, Space and Environmental Medicine*, Vol. 77, pp. 957–962, Sep 2006.

92. Nakamura, H., Y. Inoue, T. Kudo, N. Kurihara, N. Sugano, and T. Iwai, "Detection of venous emboli using doppler ultrasound," *European Journal of Vascular & Endovascular Surgery*, Vol. 35, pp. 96–101, Jan 2008.

93. Neukam, K., J. Babin-Ebell, T. Hickethier, A. Weigl, and O. Elert, "Microbubble detektion wahrend der extrakorporalen zirkulation," *Zeitschrift fur Herz, Thorax und Gefasschirurgie*, Vol. 11, no. 3, pp. 127–130, 1997.

94. Tullio, M. R. D., R. L. Sacco, N. Venketasubramanian, D. Sherman, J. P. Mohr, and S. Homma, "Comparison of diagnostic techniques for the detection of a patent foramen ovale in stroke patients," *Stroke*, Vol. 24, pp. 1020–1024, Jul 1993.

95. Pinto, F. J., "When and how to diagnose patent foramen ovale," *Heart*, Vol. 91, pp. 438–440, Apr 2005.

96. Homma, S., and R. L. Sacco, "Patent foramen ovale and stroke," *Circulation*, Vol. 112, pp. 1063–1072, Aug 2005.

97. Mohrs, O. K., S. E. Petersen, D. Erkapic, A. Victor, T. Schlosser, B. N. amd G Kauffmann, T. Voigtlaender, and H. U. Kauczor, "Dynamic contrast-enhanced mri before and after transcatheter occlusion of patent foramen ovale," *American Journal of Roentgenology*, Vol. 188, pp. 844–849, Mar 2007.

98. Nusser, T., M. Hoher, N. Merkle, O. C. Grebe, J. Spiess, H. A. Kestler, V. Rasche, M. Kochs, V. Hombach, and J. Wohrle, "Cardiac magnetic mesonance imaging and transesophageal echocardiography in patients with transcatheter closure of patent foramen ovale," *European Journal of Echocardiography*, Vol. 48, pp. 322–329, Jul 2006.

99. Hamilton-Craig, C., A. Sestito, L. Natale, A. Meduri, P. Santangeli, F. Infusino, F. Pilato, V. D. Lazzaro, F. Crea, and G. Lanza, "Contrast transoesophageal echocardiography remains superior to contrast-enhanced cardiac magnetic resonance imaging for the diagnosis of patent foramen ovale," *European Journal of Echocardiography*, Vol. 12, pp. 222–227, Mar 2011.

100. Pruszczyk, P., A. Torbicki, R. Pacho, M. Chlebus, A. Kuch-Wocial, B. Pruszynski, and H. Gurba, "Noninvasive diagnosis of suspected severe pulmonary embolism: Transesophageal echocardiography vs spiral ct," *Chest*, Vol. 112, pp. 722–728, Sep 1997.

101. Purvis, J. A., D. R. Morgan, and S. M. Hughes, "Prevalence of patent foramen ovale in a consecutive cohort of 261 patients undergoing routine coronary 64-multi-detector cardiac computed tomography," *The Ulster Medical Journal*, Vol. 80, pp. 72–75, May 2011.

102. Bulwer, B. E., and J. M. Rivero, *The Transthoracic Examination*, Massachusetts: Jones and Bartlett Publishers, 2011.

103. Brucher, R., and D. Russell, "Automatic online embolus detection and artifact rejection with the first multifrequency transcranial doppler," *Stroke*, Vol. 33, pp. 1969–1974, Aug 2002.

104. Jauss, M., M. Kaps, M. Keberle, W. Haberbosch, and W. Dorndorf, "A comparison of transesophageal echocardiography and transcranial doppler sonography with contrast medium for detection of patent foramen ovale," *Stroke*, Vol. 34, pp. 1823–1830, Nov 1999.

105. Anzola, G. P., "Clinical impact of patent foramen ovale diagnosis with transcranial doppler," *European Journal of Ultrasound*, Vol. 16, pp. 11–20, Nov 2002.

106. Stendel, R., H. J. Gramm, K. Schroder, C. Lober, and M. Brock, "Transcranial doppler ultrasonography as a screening technique for detection of a patent foramen ovale before surgery in the sitting position," *Anesthesiology*, Vol. 93, pp. 971–975, Oct 2000.

107. Zuilen, E. V. V., W. H. Mess, C. Jansen, I. V. D. Tweel, J. V. Gijn, and R. G. A. Ackerstaff, "Automatic embolus detection compared with human experts," *Stroke*, Vol. 27, pp. 1840–1843, Oct 1996.

108. Fan, L., D. H. Evans, and A. R. Naylor, "Automated embolus identification using a rule-based expert system," *Ultrasound in Medicine and Biology*, Vol. 27, pp. 1065–1077, Aug 2001.

109. Dittrich, R., M. A. Ritter, and D. W. Droste, "Microembolus detection by transcranial doppler sonography," *European Journal of Ultrasound*, Vol. 16, pp. 21–30, Nov 2002.

110. Eftedal, O., and A. O. Brubakk, "Agreement between trained and untrained observers in grading intravascular bubble signals in ultrasonic images," *Undersea & Hyperbaric Medicine*, Vol. 24, no. 4, pp. 293–299, 1997.

111. Eftedal, O., R. Mohammadi, M. Rouhani, H. Torp, and A. O. Brubakk, "Computer real time detection of intravascular bubbles," in *Proceedings of the 20th Annual Meeting of EUBS*, (Istanbul–Turkey), pp. 490–494, European Underwater and Baromedical Society, 1994.

112. Norton, M. S., A. J. Sims, D. Morris, T. Zaglavara, M. A. Kenny, and A. Murray, "Quantification of echo contrast passage across a patent foramen ovale," in *Computers in Cardiology*, (Cleveland–USA), pp. 89–92, IEEE Press-Computers in Cardiology, 1998.

113. Seiler, C., "How should we assess patent foramen ovale?," *Heart*, Vol. 90, pp. 1245–1247, Nov 2004.

114. Manning, W. J., and D. J. Pennell, *Cardiovascular magnetic resonance*, Philadelphia: Saunders Elsevier, 2nd ed., 2011.

115. Mohrs, O. K., S. E. Petersen, D. Erkapic, C. Rubel, R. Schrader, B. Nowak, W. A. Fach, H. U. Kauczor, and T. Voigtlaender, "Diagnosis of patent foramen ovale using contrast-enhanced dynamic mri: a pilot study," *American Journal of Roentgenology*, Vol. 184, pp. 234–240, Jan 2005.

116. Schuchlenz, H. W., W. Weihs, A. Beitzke, J. I. Stein, A. Gamillscheg, and P. Rehak, "Transesophageal echocardiography for quantifying size of patent foramen ovale in patients with cryptogenic cerebrovascular events," *Stroke*, Vol. 33, pp. 293–296, Jan 2002.

117. Spencer, M. P., "Decompression limits for compressed air determined by ultrasonically detected blood bubbles," *Journal of Applied Physiology*, Vol. 40, pp. 229–235, Feb 1976.

118. Kisman, K. E., G. Masurel, and R. Guillerm, "Bubble evaluation code for doppler ultrasonic decompression data," in *Annual Meeting of EUBS*, European Underwater and Baromedical Society, 1978.

119. Williamson, E. E., J. Kirsch, P. A. Araoz, W. B. Edmister, D. D. Borgeson, J. F. Glockner, and J. F. Breen, "Ecg-gated cardiac ct angiography using 64-mdct for detection of patent foramen ovale," *American Journal of Roentgenology*, Vol. 190, pp. 929–933, Apr 2007.

120. Meier, B., and J. E. Lock, "Contemporary management of patent foramen ovale," *Circulation*, Vol. 107, pp. 5–9, Jan 2003.

121. Harvey, J. R., S. M. Teague, J. L. Anderson, W. F. Voyles, and U. Thadani, "nically silent atrial septal defects with evidence for cerebral embolization," *Annals of Internal Medicine*, Vol. 105, pp. 695–697, Nov 1986.

122. Brecker, S. J. D., *Percutaneous device closure of the atrial septum*, United Kingdom: Informa Healthcare, 1st ed., 2006.

123. Porstmann, W., L. Wierny, H. Warnke, G. Gerstberger, and P. A. Romaniuk, "Catheter closure of patent ductus arteriosus: 62 cases treated without thoracotomy," *Radiologic Clinics of North America*, Vol. 9, pp. 203–218, Aug 1971.

124. Rashkind, W. J., "Transcatheter treatment of congenital heart disease," *Circulation*, Vol. 67, pp. 711–716, Apr 1983.

125. Rashkind, W. J., C. E. Mullins, W. E. Hellenbrand, and M. A. Tait, "Nonsurgical closure of patent ductus arteriosus: clinical application of the rashkind pda occluder system," *Circulation*, Vol. 75, pp. 593–599, Mar 1987.

126. Lock, J. E., J. T. Cockerham, J. F. Keane, J. P. Finley, P. E. Wakely, and K. E. Fellows, "Transcatheter umbrella closure of congenital heart defects," *Circulation*, Vol. 75, pp. 593–599, Mar 1987.

127. Lock, J. E., P. C. Block, R. G. McKay, D. S. Baim, and J. F. Keane, "Transcatheter closure of ventricular septal defects," *Circulation*, Vol. 78, pp. 361–368, Aug 1988.

128. Lock, J. E., J. J. Rome, R. Davis, S. V. Praagh, S. B. Perry, R. V. Praagh, and J. F. Keane, "Transcatheter closure of atrial septal defects: experimental studies," *Circulation*, Vol. 79, pp. 1091–1099, May 1989.

129. Rome, J. J., J. F. Keane, S. B. Perry, P. J. Spevak, and J. E. Lock, "Double-umbrella closure of atrial defects: initial clinical applications," *Circulation*, Vol. 82, pp. 751–758, Sep 1990.

130. Bridges, N. D., S. B. Perry, J. F. Keane, S. A. Goldstein, V. Mandell, J. E. M. Jr, R. A. Jonas, A. R. Casteneda, and J. E. Lock, "Preoperative transcatheter closure of congenital muscular ventricular septal defects," *Circulation*, Vol. 324, pp. 1312–1317, May 1991.

131. Hourihan, M., S. B. Perry, V. S. Mandell, J. F. Keane, J. J. Rome, J. A. Bittl, and J. E. Lock, "Transcatheter umbrella closure of valvular and paravalvular leaks," *Journal of the American College of Cardiology*, Vol. 20, pp. 1371–1377, Nov 1987.

132. Perry, S. B., M. E. van der Velde, N. D. Bridges, J. F. Keane, and J. E. Lock, "Transcatheter closure of atrial and ventricular septal defects," *Herz*, Vol. 18, pp. 135–142, Apr 1993.

133. Martín, F., P. L. Sánchez, E. Doherty, P. J. Colon-Hernandez, G. Delgado, I. Inglessis, N. Scott, J. Hung, M. E. King, F. Buonanno, Z. Demirjian, M. de Moor, and I. F. Palacios, "Percutaneous transcatheter closure of patent foramen ovale in patients with paradoxical embolism," *Circulation*, Vol. 106, pp. 1034–1036, Aug 2002.

134. Braun, M. U., D. Fassbender, S. P. Schoen, M. Haass, R. Schraeder, W. Scholtz, and R. H. Strasser, "Transcatheter closure of patent foramen ovale in patients with cerebral ischemia," *Journal of the American College of Cardiology*, Vol. 39, pp. 2019–2025, Jun 2002.

135. Fathi, A. R., P. Eshtehardi, and B. Meier, "Patent foramen ovale and neurosurgery in sitting position: a systematic review," *British Journal of Anaesthesia*, Vol. 102, pp. 588–596, May 2009.

136. Aghasadeghi, K., and R. Mollazadeh, "A dumbbell thrombus entrapped in patent foramen ovale," *European Journal of Echocardiography*, Vol. 9, p. 155, Jan 2008.

137. Bugra, Z., D. Hunerel, Y. Tayyareci, O. Ruzgar, S. Umman, T. Tansel, and M. Meric, "Echocardiographic diagnosis of a giant thrombus passing through a patent foramen ovale from right atrium to the left atrium," *Journal of Thrombosis and Thrombolysis*, Vol. 25, pp. 297–299, Jun 2008.

138. Cakir, C., H. Duygu, N. K. Eren, Z. I. Akyildiz, C. Nazli, and O. Ergene, "Witnessing a rare event - thrombus seeking its route in the right atrium: 'thrombus-in-transit'," *Journal of Cardiovascular Medicine*, Vol. 9, pp. 1166–1168, Nov 2008.

139. Eweda, I. I., S. Samir, O. Abbas, G. M. El-Gohary, and W. Nammas, "Right heart thrombus-in-transit with pulmonary embolism in a patient with primary hypercoagulable state," *Cardiology Journal*, Vol. 17, pp. 408–411, Nov 2010.

140. Turfan, M., M. A. Vatankulu, S. N. Murat, F. Oksuz, M. Duran, and E. Ornek, "Thrombolytic treatment of simultaneous pulmonary embolism and impending paradoxical embolism through a patent foramen ovale: a different thrombolytic regimen," *Heart, Lung and Circulation*, Vol. 21, pp. 225–228, Apr 2012.

141. Vanhoutte, P. M., *Cardiovascular pharmacology: Endothelial control*, USA: Academic Press, Elsevier, 1st ed., 2010.

142. Horton, S. C., and T. J. Bunch, "Patent foramen ovale and stroke," *Mayo Clinic Proceedings*, Vol. 79, pp. 79–88, Jan 2004.

143. Mas, J. L., C. Arquizan, C. Lamy, M. Zuber, L. Cabanes, G. Derumeaux, and J. Coste, "Recurrent cerebrovascular events associated with patent foramen ovale, atrial septal aneurysm, or both," *The New England Journal of Medicine*, Vol. 345, pp. 1740–1746, Dec 2001.

144. Beal, M. F., R. S. Williams, E. P. Richardson, and C. M. Fisher, "Cholesterol embolism as a cause of transient ischemic attacks and cerebral infarction," *Neurology*, Vol. 31, pp. 860–865, Jul 1981.

145. Babikian, V. L., and L. R. Caplan, "Brain embolism is a dynamic process with variable characteristics," *Neurology*, Vol. 54, pp. 797–801, Feb 2000.

146. Kawakami, Y., K. Hirose, Y. Watanabe, N. Tomioka, K. Doyama, M. Morikawa, K. Kosuga, and T. Saiga, "Management of multiple cholesterol embolization syndrome-a case report," *Angiology*, Vol. 41, pp. 248–252, Mar 1990.

147. Pell, A. C. H., D. Hughes, J. Keating, J. Christie, A. Busuttil, and G. R. Sutherland, "Fulminating fat embolism syndrome caused by paradoxical embolism through a patent foramen ovale," *The New England Journal of Medicine*, Vol. 329, pp. 926–929, Sep 1993.

148. Pell, A. C. H., J. Christie, J. Keating, and G. R. Sutherland, "The detection of fat embolism by transoesophageal echocardiography during reamed intramedullary nailing: a study of 24 patients with femoral and tibial fractures," *Journal of bone and joint surgery. British volume*, Vol. 75, pp. 921–925, Nov 1993.

149. Etchells, E. E., D. T. Wong, G. Davidson, and P. L. Houston, "Fatal cerebral fat embolism associated with a patent foramen ovale," *Chest*, Vol. 104, pp. 962–963, Sep 1993.

150. Ward, R., D. Jones, and E. F. Haponik, "Paradoxical embolism: an underrecognized problem," *Chest*, Vol. 108, pp. 549–558, Aug 1995.

151. Brown, D. V., L. P. Faber, and K. J. Tuman, "Perioperative stroke caused by arterial tumor embolism," *Anesthesia and Analgesia*, Vol. 98, pp. 806–809, Mar 2004.

152. Ling, Z., H. Yiuzhi, and L. Jianjun, "The experience of treatment of advanced liver cancer with embolism of the hepatic artery combining the placing-pump in the portal vein (analysis of 160 cases)," *Henan Journal of Oncology*, Nov 1997.

153. Wang, J., T. Su, N. Jia, J. Wang, C. Wang, S. Wang, Y. Qian, and X. Han, "Computed tomographic and magnetic resonance imaging presentations of pancreatitis maldiagnosed as pancreatic carcinoma," *Pancreas*, Vol. 39, pp. 262–264, Mar 2010.

154. Sritippayawan, S., E. F. MacLaughlin, and M. S. Woo, "Acute neurological deficits in a young adult with cystic fibrosis," *Pediatric Pulmonology*, Vol. 35, pp. 147–151, Feb 2003.

155. Miroslav, M., D. Lazar, M. Aleksandar, D. Predrag, and P. Svetozar, "Rare forms of peripheral arterial embolism: review of 11 cases," *Vascular*, Vol. 13, pp. 222–229, Jul-Aug 2005.

156. Hagers, Y., K. Koole, D. Schoors, and G. V. Camp, "Tricuspid stenosis: a rare complication of pacemaker-related endocarditis," *Journal of the American Society of Echocardiography*, Vol. 13, pp. 66–68, Jan 2000.

157. Wilmshurst, P. T., and M. A. de Belder, "Patent foramen ovale in adult life," *British Heart Journal*, Vol. 71, pp. 209–212, Mar 1994.

158. Mathieu, D., ed., *Handbook on hyperbaric medicine*, The Netherlands: Springer Verlag, 1st ed., 2006.

159. Okang, G. I., and R. D. Vann, *Bubble formation in blood and urine*, Bethesda, USA: Undersea and Hyperbaric Medical Society, 1st ed., 1989.

160. Vukovic, V., A. L. Huzjan, and V. Demarin, "Microembolus detection by transcranial doppler sonography:technical and clinical aspects," *Acta Clinica Croatica*, Vol. 44, no. 1, pp. 33–45, 2005.

161. Markus, H. S., D. Droste, and M. M. Brown, "Ultrasonic detection of cerebral emboli in carotid stenosis," *Lancet*, Vol. 341, p. 1606, Jun 1993.

162. Ishida, C., E. Furui, Y. Sakashita, and M. Yamada, "Embolic stroke with a patent foramen ovale and behcet's disease," *Internal Medicine*, Vol. 44, pp. 326–327, Apr 2005.

163. Gurgun, C., E. Ercan, C. Ceyhan, O. Yavuzgil, M. Zoghi, K. Aksu, C. S. Cinar, and C. Turkoglu, "Cardiovascular involvement in behcet's disease," *Japanese Heart Journal*, Vol. 43, pp. 389–398, Jul 2002.

164. Specker, C., J. Rademacher, D. Sohngen, M. Sitzer, I. Janda, M. Siebler, H. Steinmetz, and M. Schneider, "Cerebral microemboli in patients with antiphospholipid syndrome," *Lupus*, Vol. 6, no. 8, pp. 638–644, 1997.

165. Long, B. R., and F. Leya, "The role of antiphospholipid syndrome in cardiovascular disease," *Hematology Oncology Clinics of North America*, Vol. 22, pp. 79–94, Feb 2008.

166. Selzer, A., W. H. Carnes, C. A. N. Jr., W. H. H. Jr., and R. O. Holmes, "The syndrome of pulmonary stenosis with patent foramen ovale," *The American Journal of Medicine*, Vol. 6, pp. 3–23, Jan 1949.

167. Droste, D. W., M. A. Ritter, G. Monnig, V. Kemeny, G. Breithardt, and E. B. Ringelstein, "Abundance of microembolic signals detected by transcranial doppler ultrasound in a patient with eisenmenger's syndrome," *Cerebrovascular Diseases*, Vol. 9, pp. 334–336, Nov-Dec 1999.

168. Grenander, U., *Pattern Analysis: Lecture in Pattern Theory Volume II*, New York, USA: Springer-Verlag, 1st ed., 1978.

169. Allen, T., ed., *Powder sampling and particle size determination*, The Netherlands: Elsevier BV, 1st ed., 2003.

170. Honkanen, M., and P. Saarenrinne, "Multiphase piv method with digital object separation methods," in *5th International Symposium on Particle Image Velocimetry*, 2003.

171. Daugman, J. G., "Complete discrete 2d gabor transforms by neural networks for image analysis and compression," *IEEE Transactions on Acoustics, Speech and Signal Processing*, Vol. 36, pp. 1169–1179, Jul 1988.

172. Kepenekci, B., "Face recognition using gabor wavelet transform," Master's thesis, Middle East Technical University, Ankara, Turkey, 2001.

173. Gonzalez, R. C., R. E. Woods, and S. L. Eddins, *Digital Image Processing using Matlab*, USA: Gatesmark Publishing, 2nd ed., 2009.

174. Caselles, V., F. Catte, T. Coll, and F. Dibos, "A geometric model for active contours in image processing," *Numerische Mathematik*, Vol. 66, no. 1, pp. 1–31, 1993.

175. Chan, T., and L. Vese, "Active contours without edges," *IEEE Transactions on Image Processing*, Vol. 10, pp. 266–277, Feb 2001.

176. Vemuri, B., and Y. Chen, *Joint image registration and segmentation*, Vol. 898 of *Geometric Level Set Methods in Imaging, Vision, and Graphics*, pp. 251–259. New York: Springer-Verlag, 2003.

177. Sezgin, M., and B. Sankur, "Survey over image thresholding techniques and quantitative performance evaluation," *Journal of Electronic Imaging*, Vol. 13, pp. 146–165, Jan 2004.

178. Sezgin, M., *Quantitative evaluation of image thresholding methods and application to nondestructive testing(in turkish)*. PhD thesis, Istanbul Technical University, Istanbul, Turkey, 2002.

179. Otsu, N., "A threshold selection method from gray-level histograms," *IEEE Transactions on Systems, Man and Cybernetics*, Vol. 9, pp. 62–66, Jan 1979.

180. Tokuhiroa, A., M. Maekawab, K. Iizukab, K. Hishidab, and M. Maedab, "Turbulent flow past a bubble and an ellipsoid using shadow-image and piv techniques," *International Journal of Multiphase Flow*, Vol. 24, pp. 1383–1406, Dec 1998.

181. Hua, Y. T., S. Qinb, T. Hub, K. W. Ferrarac, and Q. Jiang, "Asymmetric oscillation of cavitation bubbles in a microvessel and its implications upon mechanisms of clinical vessel injury in shock-wave lithotripsy," *International Journal of Non-Linear Mechanics*, Vol. 40, pp. 341–350, Mar-Apr 2005.

182. Griner, P. F., R. J. Mayewski, A. I. Mushlin, and P. Greenland, "Selection and interpretation of diagnostic tests and procedures," *Annals of Internal Medicine*, Vol. 94, pp. 557–592, Apr 1981.

183. Yen, J. C., F. J. Chang, and S. Chang, "A new criterion for automatic multilevel thresholding," *IEEE Transactions on Image Processing*, Vol. 4, pp. 370–378, Mar 1995.

184. Ramesh, N., J. H. Yoo, and I. K. Sethi, "Thresholding based on histogram approximation," *IEEE Proceedings Vision, Image and Signal Processing*, Vol. 142, pp. 271–279, Oct 1995.

185. Huang, L. K., and M. J. J. Wang, "Image thresholding by minimizing the measures of fuzziness," *Pattern Recognition*, Vol. 28, pp. 41–51, Jan 1995.

186. Li, C. H., and P. K. S. Tam, "An iterative algorithm for minimum cross entropy thresholding," *Pattern Recognition Letters*, Vol. 19, pp. 771–776, Jun 1998.

187. Rosenfeld, A., and P. D. L. Torre, "Histogram concavity analysis as an aid in threshold selection," *IEEE Transactions on Systems, Man and Cybernetics*, Vol. 13, pp. 231–235, Mar–Apr 1983.

188. O'Gorman, L., "Binarization and multithresholding of document images using connectivity," *Graphical Models in Image Processing*, Vol. 56, pp. 494–506, Nov 1994.

189. Woods, T. D., and A. Patel, "A critical review of patent foramen ovale detection using saline contrast echocardiography: when bubbles lie," *Journal of the American Society of Echocardiography*, Vol. 19, pp. 215–222, Feb 2006.

190. Suri, J. S., D. L. Wilson, and S. Laxminarayan, *Handbook of biomedical image analysis volume 1: segmentation models*, Kluwer Academic / Plenum Publishers, 2005.

191. West, J. B., "Ibn al-nafis, the pulmonary circulation, and the islamic golden age," *Journal of Applied Physiology*, Vol. 105, pp. 1877–1880, Dec 2008.

192. Zheng, Y. Q., J. X. Liu, J. N. Wang, and L. Xu, "Effects of crocin on reperfusion-induced oxidative/nitrative injury to cerebral microvessels after global cerebral ischemia," *Brain Research*, Vol. 1138, pp. 86–94, Mar 2007.

193. Rigatelli, G., P. Cardaioli, and M. Chinaglia, "Asymptomatic significant patent foramen ovale: Giving patent foramen ovale management back to the cardiologist," *Catheterization and Cardiovascular Interventions*, Vol. 71, pp. 573–576, Mar 2008.

194. King, T. D., S. L. Thompson, C. Steiner, and N. L. Mills, "Secundum atrial septal defects: nonoperative closure during cardiac catheterization," *The Journal of the American Medical Association*, Vol. 235, pp. 2506–2509, Jun 1976.

195. Chan, K. C., M. J. Godman, K. Walsh, N. Wilson, A. Redington, and J. L. Gibbs, "Transcatheter closure of atrial septal defect and interatrial communications with a new self expanding nitinol double disc device (amplatzer septal occluder): multicentre uk experience," *Heart*, Vol. 82, pp. 300–306, Sep 1999.

196. Foster, P. P., A. H. Feiveson, and A. M. Boriek, "Predicting time to decompression illness during exercise at altitude, based on formation and growth of bubbles," *American Journal of Physiology - Regulatory, Integrative and Comparative Physiology*, Vol. 279, pp. 2317–2328, Dec 2000.

197. Meier, B., "Closure of patent foramen ovale: technique, pitfalls, complications, and follow up," *Heart*, Vol. 91, pp. 444–448, Apr 2005.

198. Hoffman, J. I. E., S. Kaplan, and R. R. Liberthson, "Prevalence of congenital heart disease," *The American Heart Journal*, Vol. 147, pp. 425–439, Mar 2004.

199. Hoffman, J. I. E., and S. Kaplan, "The incidence of congenital heart disease," *Journal of the American College of Cardiology*, Vol. 39, pp. 1890–1900, Jun 2002.

200. Hoffman, J. I. E., "Incidence of congenital heart disease: Ii. prenatal incidence," *Pediatric Cardiology*, Vol. 16, pp. 155–165, Jul-Aug 1995.

201. Hoffman, J. I. E., "Incidence of congenital heart disease: I. postnatal incidence," *Pediatric Cardiology*, Vol. 16, pp. 103–113, May-Jun 1995.

202. Eftedal, O. S., *Ultrasonic detection of decompression induced vascular microbubbles*. PhD thesis, Norwegian University, Trondheim, Norway, 2007.

203. Brubakk, A. O., and O. Eftedal, "Comparison of three different ultrasonic methods for quantification of intravascular bubbles," *Undersea & Hyperbaric Medicine*, Vol. 28, pp. 131–136, Fall 2001.

204. Schiller, N. B., P. M. Shah, M. Crawford, A. DeMaria, R. Devereux, H. Feigenbaum, H. Gutgesell, N. Reichek, D. Sahn, I. Schnittger, N. H. Silverman, and A. J. Tajik, "Recommendations for quantitation of the left ventricle by two-dimensional echocardiography. american society of echocardiography committee on standards, subcommittee on quantitation of two-dimensional echocardiograms," *Journal of the American Society of Echocardiography*, Vol. 2, pp. 358–367, Sep-Oct 1989.

205. Wilmshurst, P., "The effect of persistent foramen ovale closure on migraine remains an enigma," *Cardiovascular Interventions*, Vol. 2, pp. 114–115, Feb 2009.

206. Wilmshurst, P., J. Panikkar, M. Pearson, and S. Nightingale, "Relation between inheritance of cyanotic congenital heart disease and persistent foramen ovale," *American Journal of Cardiology*, Vol. 104, pp. 148–149, Jul 2009.

207. Hirth, A., S. Nightingale, P. Wilmshurst, P. Disney, and S. Thorne, "Prevalence of migraine in adults with cyanotic congenital heart disease," *Congenital Heart Disease*, Vol. 3, pp. 124–127, Mar 2008.

208. Wilmshurst, P., S. Nightingale, M. Pearson, L. Morrison, and K. Walsh, "Relation of atrial shunts to migraine in patients with ischemic stroke and peripheral emboli," *American Journal of Cardiology*, Vol. 98, pp. 831–833, Sep 2006.

209. Wilmshurst, P., and S. Nightingale, "The role of cardiac and pulmonary pathology in migraine: a hypothesis," *Headache*, Vol. 46, pp. 429–434, Mar 2006.

210. Wilmshurst, P., and S. Nightingale, "Relationship between migraine and cardiac and pulmonary right-to-left shunts," *Clinical Science*, Vol. 100, pp. 215–220, Feb 2001.

211. Wilmshurst, P., "Cardiovascular problems in divers," *Heart*, Vol. 80, pp. 537–538, Dec 1998.

212. Reisman, M., R. D. Christofferson, J. Jesurum, J. V. Olsen, M. P. Spencer, K. A. Krabill, L. Diehl, S. Aurora, and W. A. Gray, "Migraine headache relief after transcatheter closure of patent foramen ovale," *Journal of the American College of Cardiology*, Vol. 45, pp. 493–495, Feb 2005.

213. Johansson, M. C., P. Eriksson, Y. Peker, J. Hedner, L. Rastam, and U. Lindblad, "The influence of patent foramen ovale on oxygen desaturation in obstructive sleep apnoea," *The European Respiratory Journal*, Vol. 29, pp. 149–155, Jan 2007.

214. Nootens, M. T., L. A. Berarducci, E. Kaufmann, S. Devries, and S. Rich, "The prevalence and significance of a patent foramen ovale in pulmonary hypertension," *Chest*, Vol. 104, pp. 1673–1675, Dec 1993.

215. Shanoudy, H., A. Soliman, P. Raggi, J. W. Liu, D. C. Russell, and N. F. Jarmukli, "Prevalence of patient foramen ovale and its contrubition to hypoxemia in patients with obstructive sleep apnea," *Chest*, Vol. 113, pp. 91–96, Jan 1998.

216. Kerut, E. K., W. T. Norfleet, G. D. Plotnick, and T. D. Giles, "Patent foramen ovale: a review of associated conditions and the impact of physiological size," *Journal of the American College of Cardiology*, Vol. 38, pp. 613–623, Sep 2001.

217. Dujic, Z., I. Palada, A. Obad, D. Duplancic, A. O. Brubakk, and Z. Valic, "Exercise-induced intrapulmonary shunting of venous gas emboli does not occur after open-sea diving," *Journal of Applied Physiology*, Vol. 99, pp. 944–949, Sep 2005.

218. Kuhl, H. P., R. Hoffmann, M. W. Merx, A. Franke, C. Klotzsch, W. Lepper, T. Reineke, J. Noth, and P. Hanrath, "Transthoracic echocardiography using second harmonic imaging: diagnostic alternative to transesophageal echocardiography for the detection of atrial right to left shunt in patients with cerebral embolic events," *Journal of the American College of Cardiology*, Vol. 34, pp. 1823–1830, Nov 1999.

219. Blum, A., S. Reisner, and Y. Farbstein, "Transesophageal echocardiography (tee) vs. transthoracic echocardiography (tte) in assessing cardio-vascular sources of emboli in patients with acute ischemic stroke," *Medical Science Monitor*, Vol. 10, pp. 521–523, Sep 2004.

220. Clarke, N. R., J. Timperley, A. D. Kelion, and A. P. Banning, "Transthoracic echocardiography using second harmonic imaging with valsalva manoeuvre for the detection of right to left shunts," *European Journal of Echocardiography*, Vol. 5, pp. 176–181, Jun 2004.

221. Kerr, A. J., T. Buck, K. Chia, C. M. Chow, E. Fox, R. A. Levine, and M. H. Picard, "Transmitral doppler: a new transthoracic contrast method for patent foramen ovale detection and quantification," *Journal of the American College of Cardiology*, Vol. 36, pp. 1959–1966, Nov 2000.

222. Engelhardt, M., W. Folkers, C. Brenke, M. Scholz, A. Harders, H. Fidorra, and K. Schmieder, "Neurosurgical operations with the patient in sitting position: analysis of risk factors using transcranial doppler sonography," *British Journal of Anaesthesia*, Vol. 96, pp. 467–472, Apr 2006.

223. Beacock, D. J., V. B. Watt, G. D. Oakley, and A. A. Mohammad, "Paradoxical embolism with a patent foramen ovale and atrial septal aneurysm," *European Journal of Echocardiography*, Vol. 7, pp. 171–174, Mar 2006.